

STATISTICS OF 207 Ly α EMITTERS AT A REDSHIFT NEAR 7: CONSTRAINTS ON REIONIZATION AND GALAXY FORMATION MODELS*

MASAMI OUCHI^{1,2,3,10}, KAZUHIRO SHIMASAKU^{4,5}, HISANORI FURUSAWA⁶, TOMOKI SAITO², MAKIKO YOSHIDA⁴,
 MASAYUKI AKIYAMA⁷, YOSHIKI ONO⁴, TORU YAMADA⁷, KAZUAKI OTA¹, NOBUNARI KASHIKAWA⁶, MASANORI IYE⁶,

TADAYUKI KODAMA⁶, SADANORI OKAMURA^{4,5}, CHRIS SIMPSON⁸, AND MICHITOSHI YOSHIDA⁹

¹ Institute for Cosmic Ray Research, University of Tokyo, Kashiwa 277-8582, Japan; ouchims@icrr.u-tokyo.ac.jp

² Institute for the Physics and Mathematics of the Universe (IPMU), University of Tokyo, Kashiwa 277-8568, Japan

³ Observatories of the Carnegie Institution of Washington, 813 Santa Barbara Street, Pasadena, CA 91101, USA

⁴ Department of Astronomy, School of Science, University of Tokyo, Tokyo 113-0033, Japan

⁵ Research Center for the Early Universe, School of Science, University of Tokyo, Tokyo 113-0033, Japan

⁶ National Astronomical Observatory, Mitaka, Tokyo 181-8588, Japan

⁷ Astronomical Institute, Graduate School of Science, Tohoku University, Aramaki, Aoba, Sendai 980-8578, Japan

⁸ Astrophysics Research Institute, Liverpool John Moores University, Twelve Quays House, Egerton Wharf, Birkenhead CH41 1LD, UK

⁹ Okayama Astrophysical Observatory, National Astronomical Observatory, Kamogata, Okayama 719-0232, Japan

Received 2010 July 16; accepted 2010 September 2; published 2010 October 15

ABSTRACT

We present the Ly α luminosity function (LF), clustering measurements, and Ly α line profiles based on the largest sample to date of 207 Ly α emitters (LAEs) at $z = 6.6$ on the 1 deg² sky of Subaru/XMM-Newton Deep Survey field. Our $z = 6.6$ Ly α LF including cosmic variance estimates yields the best-fit Schechter parameters of $\phi^* = 8.5^{+3.0}_{-2.2} \times 10^{-4} \text{ Mpc}^{-3}$ and $L^*_{\text{Ly}\alpha} = 4.4^{+0.6}_{-0.6} \times 10^{42} \text{ erg s}^{-1}$ with a fixed $\alpha = -1.5$, and indicates a decrease from $z = 5.7$ at the $\gtrsim 90\%$ confidence level. However, this decrease is not large, only $\simeq 30\%$ in Ly α luminosity, which is too small to have been identified in the previous studies. A clustering signal of $z = 6.6$ LAEs is detected for the first time. We obtain the correlation length of $r_0 = 2\text{--}5 \text{ } h_{100}^{-1} \text{ Mpc}$ and a bias of $b = 3\text{--}6$, and find no significant boost of clustering amplitude by reionization at $z = 6.6$. The average hosting dark halo mass inferred from clustering is $10^{10}\text{--}10^{11} M_\odot$, and a duty cycle of LAE population is roughly $\sim 1\%$, albeit with large uncertainties. The average of our high-quality Keck/DEIMOS spectra shows an FWHM velocity width of $251 \pm 16 \text{ km s}^{-1}$. We find no large evolution of the Ly α line profile from $z = 5.7$ to 6.6 , and no anti-correlation between Ly α luminosity and line width at $z = 6.6$. The combination of various reionization models and our observational results about the LF, clustering, and line profile indicates that there would exist a small decrease of the intergalactic medium's (IGM's) Ly α transmission owing to reionization, but that the hydrogen IGM is not highly neutral at $z = 6.6$. Our neutral-hydrogen fraction constraint implies that the major reionization process took place at $z \gtrsim 7$.

Key words: cosmology: observations – dark ages, reionization, first stars – galaxies: formation – galaxies: high-redshift – galaxies: luminosity function, mass function

1. INTRODUCTION

Understanding the physical process of cosmic reionization is one of the major goals in astronomy today. Although the increase of Gunn–Peterson (GP) optical depths may be contiguous from low z to $z > 6$ (Becker et al. 2007), the evolution of GP optical depths clearly show the steep rise at $z \sim 6$ toward high- z (Fan et al. 2006). On the other hand, Dunkley et al. (2009) find that the polarization data of WMAP place the constraints that instantaneous reionization at the late epoch below $z = 8.2$ (6.7) is rejected at the 2σ (3σ) level, and claim that the reionization process would be extended at $z \sim 6\text{--}11$ (see also Larson et al. 2010 for the latest WMAP7 results). However, physical models would not easily reproduce such a long extended reionization due to the rapid recombination of hydrogen (e.g., Fukugita & Kawasaki 1994; Cen 2003). Observational measurements on the neutral-hydrogen fraction of the intergalactic medium (IGM) at $z \sim 6\text{--}11$ are the missing pieces in this cosmological puzzle.

Studies of galaxies near the epoch of reionization (EoR) at $z \gtrsim 6$ are essential not only for understanding the cosmic reionization process but also galaxy formation history. The combination of Subaru and Very Large Telescope (VLT) wide-field cameras (WFCs) and the newly installed *Hubble Space Telescope* (HST)/WFC3 has identified a definitive decrease of the UV-continuum luminosity function (LF) from $z = 6$ to $7\text{--}8$ (Ouchi et al. 2009b; Oesch et al. 2010; Bouwens et al. 2010a; McLure et al. 2010; Castellano et al. 2010; Wilkins et al. 2010a, 2010b; Bunker et al. 2009; Yan et al. 2010; see also Hickey et al. 2010), which is also reproduced by recent hydrodynamic simulations (Finlator et al. 2010). Accordingly, the star formation rates drop by roughly an order of magnitude from its peak of $z = 2\text{--}3$ to $z = 7$, and this decrease implies that observations are touching the initial formation epoch of galaxies. Because galaxies are thought to be sources of reionization, the decrease of UV LF would indicate that galaxies produce less UV ionizing photons toward high redshifts. The production rate of UV ionizing photons is close to balance with the recombination rate of hydrogen IGM at $z \sim 7\text{--}8$, and the reionizing epoch may be near these redshifts. The other interpretation of the decrease of UV LF is that a moderately high ionizing photon escape fraction, $f_{\text{esc}} \gtrsim 0.2$, is required to keep the universe ionized at $z \sim 7$ (e.g., Ouchi et al. 2009b; Bunker et al. 2009). The faintest HST/WFC3 sources at

* Based on data obtained with the Subaru Telescope and the W. M. Keck Observatory. The Subaru Telescope is operated by the National Astronomical Observatory of Japan. The W. M. Keck Observatory is operated as a scientific partnership among the California Institute of Technology, the University of California, and the National Aeronautics and Space Administration.

¹⁰ Carnegie Fellow.

$z \simeq 7\text{--}8$ show a very blue UV-continuum slope possibly consistent with extremely young, metal-poor stellar populations, which is also suggestive of a large escape fraction of $f_{\text{esc}} \gtrsim 0.3$ (Bouwens et al. 2010b; see also Finkelstein et al. 2010), although there are claims that their UV-continuum slope measurements include potentially large statistical and systematic uncertainties (Schaerer & de Barros 2010).

On the other hand, neutral hydrogen of IGM absorbs the Ly α emission line from galaxies via the Ly α damping wing, and dim Ly α luminosity, which would be identified in the evolution of Ly α emitters (LAEs; e.g., Malhotra & Rhoads 2004; Kashikawa et al. 2006; Iye et al. 2006; Ota et al. 2008). Malhotra & Rhoads (2004) and Hu & Cowie (2006) find no significant change of Ly α LF from $z = 5.7$ to 6.6, while the study of Kashikawa et al. (2006) claims that Ly α LF evolves from $z = 5.7$ to 6.6. Similarly, Ly α LF evolution from $z = 5.7$ toward higher redshifts, $z \simeq 7\text{--}7.7$, is also under debate. Ly α LFs at these redshifts are poorly determined with only one spectroscopically confirmed LAE at $z = 7.0$ (Iye et al. 2006; Ota et al. 2008) and with relatively less reliable $z \simeq 7.7$ candidates with no spectroscopic confirmation (Hibon et al. 2010; Tilvi et al. 2010). Moreover, beyond this epoch, only weak upper limits are placed on Ly α LF at $z \simeq 8.8$ (Willis & Courbin 2005; Cuby et al. 2007; Willis et al. 2008; Sobral et al. 2009; cf. Stark et al. 2007). There are two conclusions from these $z = 6.6\text{--}7.7$ studies—no evolution and a decrease of Ly α LF—which do not agree with each other. These different conclusions of Ly α LF evolution may be raised by contamination, small statistics, and systematic errors such as cosmic variance. Moreover, a careful argument is needed for the interpretation of Ly α LF evolution because properties of star formation galaxies are changing, which are already found in the decrease of UV LF of dropout galaxies as discussed above. It is also important to constrain reionization and galaxy formation models with other observational quantities. The stacked spectra of $z = 6.6$ LAEs show no clear signal of Ly α damping wing absorption (Kashikawa et al. 2006; Hu & Cowie 2006). Recent theoretical studies predict that clustering measurements of LAEs can be an independent probe of reionization. Since Ly α lines of galaxies residing in ionized bubbles selectively escape from a partially neutral universe, clustering amplitude of observed LAEs would be boosted at the EoR (Furlanetto et al. 2006; McQuinn et al. 2007; Lidz et al. 2009; cf. Iliev et al. 2008). Although the importance of $z > 6$ LAE clustering is claimed from theoretical studies, no observational study has provided a reliable measurement. Kashikawa et al. (2006) measured the angular correlation function (ACF) of 58 LAEs at $z = 6.6$, which is so far the largest sample of $z = 6.6$ LAEs, but no significant signal is detected, probably due to the small statistics (McQuinn et al. 2007).

To address these issues in statistics of $z = 6.6$ LAEs, we are conducting an extensive survey that is the largest ever performed in terms of area and number of objects (cf. Malhotra & Rhoads 2004; Hu et al. 2005; Kashikawa et al. 2006). Our survey field is a large 1 deg^2 area of Subaru/XMM-Newton Deep Survey (SXDS) field well separated from the Subaru Deep Field (SDF) of Kashikawa et al. (2006). The combination of SXDS and SDF data will allow us to provide a large statistical sample with cosmic variance error estimates. The spectroscopic component of this survey is underway with Keck/DEIMOS and Magellan/IMACS (M. Ouchi et al. 2010, in preparation). The aim of this study is to supply the reliable statistical measurements of $z = 6.6$ LAEs based on our large sample that are useful

for constraining the existing and forthcoming cosmological models of cosmic reionization and galaxy formation. Our $z = 6.6$ LAE results from the large statistics will also be good baselines for ongoing and future studies of LAEs at $z > 7$ performed with the existing near-infrared imagers of VLT (Willis et al. 2008), Subaru (Tokoku et al. 2008), and VISTA (Nilsson et al. 2007) and the future facilities of the *James Webb Space Telescope*, E-ELT, GMT, and TMT. We present our survey and sample in Section 2, LFs in Section 3, clustering properties in Section 4, Ly α line profiles in Section 5, and discuss reionization and galaxy formation by comparisons with theoretical models in Section 6. Throughout this paper, magnitudes are in the AB system. We adopt a cosmology parameter set of $(h, \Omega_m, \Omega_\Lambda, n_s, \sigma_8) = (0.7, 0.3, 0.7, 1.0, 0.8)$ consistent with the WMAP results (Komatsu et al. 2009; Larson et al. 2010).

2. OBSERVATIONS AND DATA REDUCTION

2.1. Imaging Observations

We carried out extensive deep narrowband imaging with Subaru/Suprime-Cam (Miyazaki et al. 2002) for SXDS in 2005–2007. We summarize details of our observations as well as image qualities in Table 1. We used the narrowband filter, *NB921*, with a central wavelength of $\lambda_c = 9196\text{ \AA}$ and an FWHM of 132 \AA . The response curves of the *NB921* band and broadband filters are presented in Figure 1 of Ouchi et al. (2008). Five pointings of Suprime-Cam covered five subfields of SXDS, SXDS-C, -N, -S, -E, and -W (Furusawa et al. 2008), by 8.3, 10.5, 10.3, 8.2, and 7.8 hr on-source integration, respectively. In addition to these narrowband images, we use archival data of deep broadband (*B*, *V*, *R*, *i'*, and *z'*) images of the SXDS project (Furusawa et al. 2008) as summarized in the second half of Table 1. The narrowband data are reduced with the Suprime-Cam Deep field REDuction package (SDFRED; Yagi et al. 2002; Ouchi et al. 2004a). With the standard parameter sets of SDFRED, we perform bias subtraction, flat-fielding, distortion+atmospheric-dispersion corrections, sky subtraction, image alignments, and stacking. Before stacking, we mask out bad data areas such as dead pixels and satellite trails. Cosmic rays are removed in the process of stacking with the rejected-mean algorithm. The final *NB921* images have the seeing size of $0''.7\text{--}0''.8$ in FWHM, and reach the 3σ limiting magnitudes of $26.2\text{--}26.4\text{ mag}$ in a $2''.0$ diameter aperture.

We use neither contaminated areas with halos of bright stars and CCD blooming nor low signal-to-noise ratio (S/N) regions located around the edge of the field of view, which are caused by dithering. After we remove these low-quality regions from our catalog (Section 2.2), the effective total area is 3238 arcmin^2 . This effective area corresponds to the survey volume of $8.0 \times 10^5\text{ Mpc}^3$ at $z = 6.565 \pm 0.054$, if we assume a simple top-hat selection function of LAEs whose redshift distribution is defined by the FWHM of our narrowband filter.

During the observations, we took images of spectrophotometric standard star of GD71 with the *NB921*-band filter (Bohlin et al. 1995). The standard star was observed under photometric conditions on 2006 November 18 and 2007 October 11–12. We calculate photometric zero points from the standard star data. We check these photometric zero points based on colors of stellar objects in our field and 175 Galactic stars calculated from spectra given in Gunn & Stryker (1983). We find that colors of stellar objects in our data are consistent with those of Gunn & Stryker's (1983) stars within $\simeq 0.05\text{ mag}$.

Table 1
Imaging Observations and Data

Band	Field Name(s)	Exposure Time (s)	PSF Size ^a (arcsec)	Area (arcmin ²)	m_{lim}^b (3σ AB mag)	Date of Observations
<i>N B921</i>	SXDS-C	30000	0.73 (0.81)	590	26.2	2005 Oct 29, Nov 1, 2007 Oct 11–12
<i>N B921</i>	SXDS-N	37800	0.75 (0.85)	734	26.4	2005 Oct 30–31, Nov 1, 2006 Nov 18, 2007 Oct 11–12
<i>N B921</i>	SXDS-S	37138	0.79 (0.83)	783	26.2	2005 Aug 29, Oct 29–30, Nov 1, 2006 Nov 18, 2007 Oct 12
<i>N B921</i>	SXDS-E	29400	0.65 (0.83)	610	26.2	2005 Oct 31, Nov 1, 2006 Nov 18, 2007 Oct 11–12
<i>N B921</i>	SXDS-W	28101	0.75 (0.83)	521	26.2	2006 Nov 18, 2007 Oct 11–12
Archival broadband data ^c						
<i>B</i>	SXDS-C,N,S,E,W	19800–20700	0.78–0.84	915–979	28.1–28.4	...
<i>V</i>	SXDS-C,N,S,E,W	17460–19260	0.72–0.82	915–979	27.7–27.8	...
<i>R</i>	SXDS-C,N,S,E,W	13920–14880	0.74–0.82	915–979	27.5–27.7	...
<i>i'</i>	SXDS-C,N,S,E,W	18540–38820	0.68–0.82	915–979	27.5–27.7	...
<i>z'</i>	SXDS-C,N,S,E,W	11040–18660	0.70–0.76	915–979	26.4–26.6	...

Notes.

^a FWHM of PSFs in the reduced image. Values in parenthesis indicate the FWHMs of PSF that are matched with the broadband images in each field.

^b Limiting magnitude defined by a 3σ sky noise in a $2''$ diameter circular aperture.

^c The archival broadband data of SXDS presented in Furusawa et al. (2008). We show the properties of the five-subfield images on a single line. Note that the exposure time is not a total of the five subfields, but one subfield, i.e., integration per pixel. More details are presented in Table 2 of Furusawa et al. (2008).

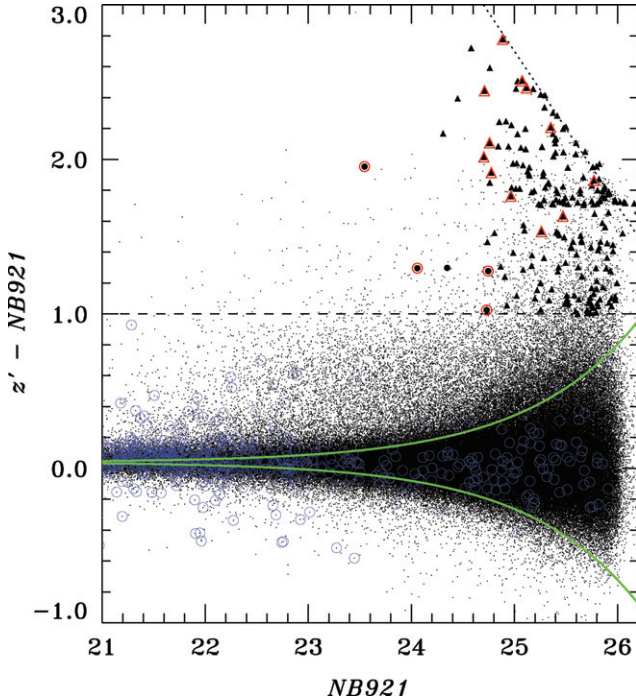


Figure 1. Color-magnitude diagram of narrowband excess color ($z' - \text{NB921}$) vs. narrowband magnitude (NB921). Black dots present colors of all the detected objects. Black filled circles and triangles denote our $z = 6.6$ LAEs. Specifically, the triangles indicate LAEs with z' -band magnitudes fainter than that of the 3σ level, and show their 1σ lower limits of their $z' - \text{NB921}$ colors. Red and blue open symbols mark spectroscopically identified objects in the redshift range of LAEs and interlopers, respectively. We define the redshift ranges of LAEs as 6.45–6.65 (see Figure 4 for the redshift range). The green lines indicate 2σ errors of the color of $z' - \text{NB921}$ for a source with a color of $z' - \text{NB921} = 0.04$, which corresponds to the median color of all objects. Dashed and dotted lines represent our color cut for narrowband excess and the 1σ limit of z' data, respectively. Note that NB921 magnitudes are total magnitudes, while the colors of $z' - \text{NB921}$ are defined with a $2''$ diameter aperture.

Our narrowband images are aligned with the deep optical *BVRiz* images from the SXDS survey (Table 1; Furusawa et al. 2008) based on hundreds of stellar objects commonly detected in both narrowband and broadband images. The astrometry

of our objects is the same as those of the SXDS version 1.0 catalog (Furusawa et al. 2008). The errors in the relative positions of objects are $\sim 0''.04$ in rms. The rms accuracy of the absolute positions is estimated in Furusawa et al. (2008) to be $\sim 0''.2$. After the image registration, we homogenize the point-spread function (PSF) sizes of broadband and narrowband images, referring to these stellar objects. The PSF sizes of our narrowband images match those of broadband images with an accuracy of $\Delta\text{FWHM} \simeq 0''.01$.

2.2. Photometric Sample of $z = 6.6$ LAEs

We identify 286,510 objects in the *NB921* images down to $\text{NB921} = 26.0$ with SExtractor (Bertin & Arnouts 1996). We measure both *MAG_AUTO* of SExtractor and $2''.0$ diameter aperture magnitudes. We adopt *MAG_AUTO* as total magnitudes, while we use a $2''.0$ diameter aperture magnitude to measure colors of objects in order to obtain colors of faint objects with a good S/N. We correct the magnitudes of objects for Galactic extinction of $E(B - V) = 0.020$ (Schlegel et al. 1998).

We plot a color-magnitude diagram in Figure 1 for our objects. Figure 1 shows narrowband excess color, $z' - \text{NB921}$, and narrowband magnitudes, NB921 . Figure 2 presents a two-color diagram based on the *NB921*-detection catalog, together with colors of model galaxies and Galactic stars. We plot colors of 3249 spectroscopically identified objects, which include our 16 $z = 6.6$ LAEs (see Section 2.3) and 3233 foreground/background interlopers (Ouchi et al. 2008). Spectroscopically identified LAEs are located in the upper right part of the two-color diagram, having a narrowband excess of $\text{Ly}\alpha$ emission ($z' - \text{NB921}$) and red continuum colors of a GP trough ($i' - z'$).

Based on the color diagram, we select candidate LAEs with the narrowband excess, no detection of blue continuum flux, and the existence of GP trough, by the color criteria,

$$z' - \text{NB921} > 1.0 \text{ and } B > B_{2\sigma} \text{ and } V > V_{2\sigma} \text{ and} \\ [(z' < z'_{3\sigma} \text{ and } i' - z' > 1.3) \text{ or } (z' \geq z'_{3\sigma})], \quad (1)$$

which are similar to those in the study of SDF (Taniguchi et al. 2005; Kashikawa et al. 2006). $B_{2\sigma}$ and $V_{2\sigma}$ are defined as 2σ limiting magnitudes of the *B* and *V* bands, respectively

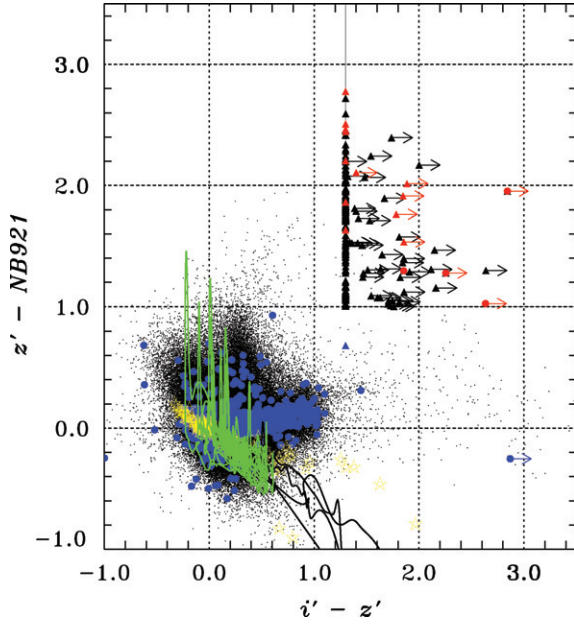


Figure 2. Two-color diagram of narrowband excess color ($z' - NB921$) vs. continuum color ($i' - z'$). Black dots present colors of all the detected objects. Our $z = 6.6$ LAEs are shown by black and red filled circles+triangles. The triangles have a z' -band magnitude fainter than 3σ level, and present the 1σ lower limit of $z' - NB921$. Red and blue circles+triangles indicate spectroscopically identified objects in and out of the LAE redshift range, respectively. We take the same LAE redshift range as that of Figure 1. For display purposes, objects with no color measurements (no z' -band detection at the 3σ level) are placed at a color of $i' - z' = 1.3$. The vertical and horizontal solid lines show our color criteria (Equation (1)) for sources with a detection in the z' band. Colors are defined with a $2''$ diameter aperture. Curves present tracks of model interloper galaxies at different redshifts. Green lines show six templates of starburst galaxies (Kinney et al. 1996) up to $z = 2$, which are six classes of starburst galaxies with different dust extinction ($E(B-V) = 0.0-0.7$). The narrowband excess peaks in the green lines correspond to the emission lines of $H\alpha$ ($z = 0.4$), $[O III]$ ($z = 0.8$), $H\beta$ ($z = 0.9$), or $[O II]$ ($z = 1.5$). Black lines represent colors of typical elliptical, spiral, and irregular galaxies (Coleman et al. 1980) which are redshifted from $z = 0$ to $z = 2$. Yellow star marks are 175 Galactic stars given by Gunn & Stryker (1983).

($B_{2\sigma} = 28.7$ and $V_{2\sigma} = 28.2$), which ensure no detection of continuum bluer than Lyman break ($\simeq 6900 \text{ \AA}$) for objects at $z = 6.6$. $z'_{3\sigma}$ is the 3σ detection limit ($z'_{3\sigma} = 26.5$).

We obtain a photometric sample of 207 LAEs at $z \simeq 6.56 \pm 0.05$ down to $NB921 = 26.0$ in a comoving survey volume of $8 \times 10^5 \text{ Mpc}^3$ (Ouchi et al. 2009a). Our selection criteria correspond to LAEs with the rest-frame equivalent width, EW_0 , of $\gtrsim 36 \text{ \AA}$, if a flat continuum spectrum ($f_\nu = \text{const}$) is assumed. If the realistic spectrum of LAEs with a GP trough is assumed, the limit of rest-frame equivalent width is $EW_0 \gtrsim 14 \text{ \AA}$ and a limiting line flux of $f \gtrsim 5 \times 10^{-18} \text{ erg s}^{-1} \text{ cm}^{-2}$ corresponding to $L \gtrsim 2.5 \times 10^{42} \text{ erg s}^{-1}$ at $z \simeq 6.56$.

2.3. Spectroscopic Observations

We conducted deep spectroscopic follow-up for our $z = 6.6$ LAEs with Keck/DEIMOS (Faber et al. 2003) on 2007 November 6, 2008 August 1, and 2008 October 3. We took spectra of 3.0 hr on-source integration for three masks and 2.3 hr integration for one mask with a $1''$ slit and the 830G grating, which covered $\simeq 6000-10000 \text{ \AA}$ and gave a medium-high spectral resolution of $R \simeq 3600$ at 9200 \AA . We observed 30 out of the 207 LAEs including faint LAEs whose expected flux is below our observational limit, and obtained 19 spectra with significant signals. All of the 19 spectra show a single line at around 9200 \AA with no detectable continuum. Because we allowed redundant

observations for six LAEs that can be included in two different masks. Three out of 19 detected objects were taken for the same targets. Thus, totals of the observed and identified LAEs are 24 ($= 30 - 6$) and 16 ($= 19 - 3$), respectively. We hereafter refer to the 24 galaxies as the spectroscopic sample. The three duplicate spectra with the signals present an emission line at the same wavelength as the original spectra, and confirm that the emission lines are real signals. We use these three duplicate spectra for the stacking analysis in Section 5.

We present our spectra in Figure 3. We have confirmed that no spectra show signatures of an $[O III] \lambda 5007$ emission line (at $\sim 7000 \text{ \AA}$) and an $[O II] \lambda 3727$ emission line (at $\sim 5200 \text{ \AA}$) from a $z = 0.40$ $H\alpha$ emitter or an $[O II]$ emission line (at $\sim 6800 \text{ \AA}$) from a $z = 0.84$ $[O III]$ emitter, and found that these objects are neither a foreground $H\alpha$ nor $[O III]$ emitters. If there is a $z \simeq 1.47$ $[O II]$ emitter, it should show a $\lambda\lambda 3726, 3729$ doublet whose separation is 7 \AA . Our DEIMOS spectra with an FWHM spectral resolution of 2.6 \AA can distinguish the doublet from an $Ly\alpha$ line with a characteristic asymmetric profile. Our DEIMOS spectra confirm no such signature of $[O II]$ doublet, but mostly clear asymmetric line profiles with an extended red wing that is typical for a high- z $Ly\alpha$ line. One exception is the spectrum of $NB921-W-35578$, which has three spikes in the range of $\simeq 9156-9162 \text{ \AA}$. The two-dimensional spectrum of $NB921-W-35578$ presents a significant residual of sky subtraction around $\simeq 9159-9164 \text{ \AA}$, although a signal of emission line is clearly seen in the wavelength range free of residuals. The complicated spectral shape of $NB921-W-35578$ is probably made by errors of sky subtraction. Table 2 summarizes properties of the 16 LAEs in our spectroscopic sample. The $Ly\alpha$ emission lines of these LAEs are strong, $EW_0 \gtrsim 20 \text{ \AA}$, which are consistent with the expected EW_0 from our color criteria ($EW_0 \gtrsim 14 \text{ \AA}$; Section 2.2). Figure 4 plots the redshift distribution of our spectroscopic sample, together with a selection function simply estimated from the filter response curve of the $NB921$ band. The estimated selection function is similar to the redshift distribution of our spectroscopically identified LAEs.

3. LUMINOSITY FUNCTION

3.1. Completeness and Contamination of our Sample

We estimate the completeness and contamination of our sample in the same manner as Ouchi et al. (2008). First, we estimate the detection completeness of narrowband images, f_{det} , as a function of narrowband magnitude. We distribute 7400 artificial objects with a PSF profile that mimic LAEs on our original 3238 arcmin^2 images after adding photon noise, and detect them in the same manner as for the detection of our LAE catalogs with SExtractor. We repeat this process 10 times and compute the detection completeness. We plot the detection completeness as a function of magnitude in the top panel of Figure 5. The top panel of Figure 5 presents that the detection completeness is typically $\simeq 80\%-90\%$ for relatively luminous sources with $NB921 < 25.5$. The detection completeness is $\simeq 50\%$ in the faintest magnitude bin of our sample, $NB921 = 25.5-26.0$.

Second, we estimate the contamination of our LAE samples. There are no interlopers in our spectroscopic sample. We also use a spectroscopic catalog of 3233 SXDS objects at low redshifts of $z = 0-6$ (Ouchi et al. 2008) and find that none of these 3233 low- z objects are included in our $z = 6.6$ LAE sample. We define the contamination fraction, f_{cont} , as

$$f_{\text{cont}} = N_{\text{low}z} / N_{\text{all}}, \quad (2)$$

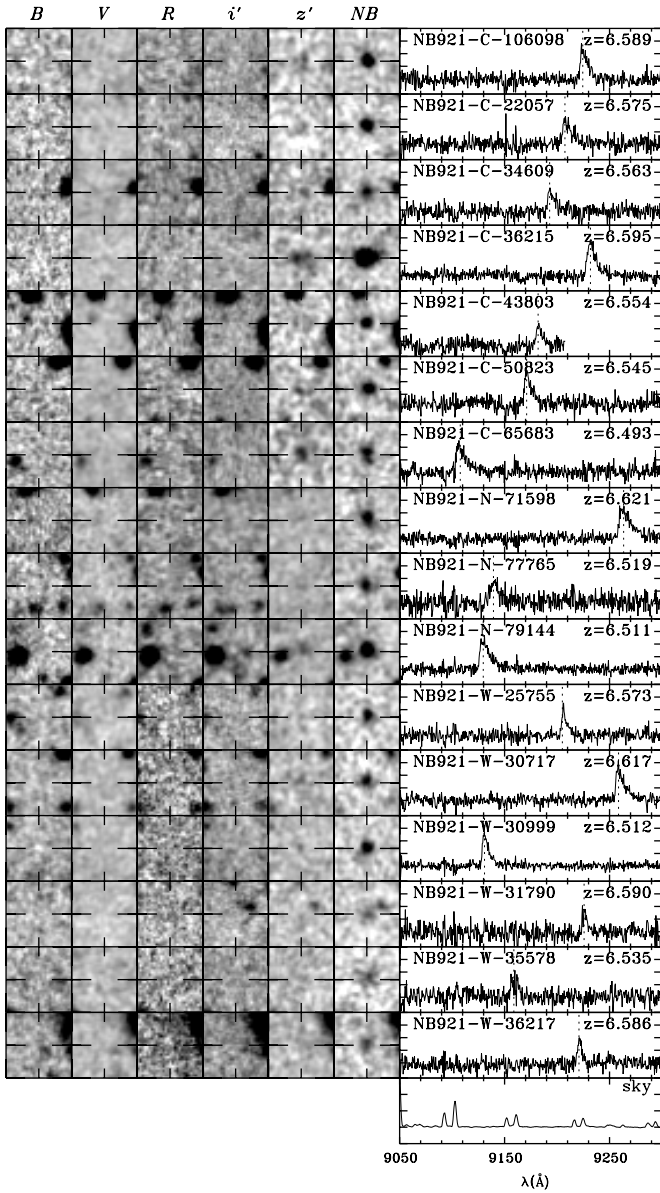


Figure 3. Spectra and snapshots of our $z = 6.6$ LAEs confirmed with Keck/DEIMOS. Each object has a spectrum in the right panel and snapshots of B , V , R , i' , z' , and $NB921$ images in the left panels. Each snapshot is presented in a $6'' \times 6''$ box. The object name and redshift are presented in the left and right corners of each spectrum panel, respectively. The right bottom panel shows a typical DEIMOS spectrum of the sky background that is obtained in the process of sky subtraction.

where $N_{\text{low}z}$ and N_{all} are the numbers of low- z interlopers and all objects, respectively, in our spectroscopy sample.

The totals of the spectroscopically observed and identified LAEs are 24 and 16, respectively (Section 2.3). Since there are eight objects with no identification in our spectroscopic sample (see Section 2.3), we calculate f_{cont} for the following two extreme cases. If all of these unidentified objects are real LAEs whose $\text{Ly}\alpha$ lines are simply too faint or extended to be detected in our spectroscopy, we find $N_{\text{low}z}/N_{\text{all}} = 0/24$ because of the lack of interlopers in our spectroscopic sample. If all the unidentified objects are interlopers, $N_{\text{low}z}/N_{\text{all}} = (24 - 16)/24$. Thus, the contamination rate is taken within the range of $f_{\text{cont}} \simeq 0\% - 30\%$ for our LAE samples. Note that there are no obvious contaminants in our follow-up spectroscopy and the SXDS catalogs. Moreover, the ongoing DEIMOS and IMACS

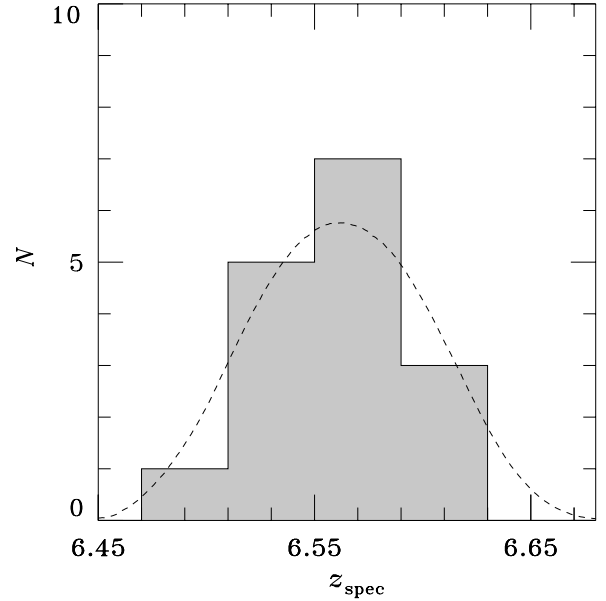


Figure 4. Redshift distribution of our LAEs with a spectroscopic identification. Histogram presents LAEs confirmed by our Keck/DEIMOS observations. The dashed line represents the selection function of LAEs that is simply calculated from the response curves of the $NB921$ filter. The selection function is normalized by the number of identified LAEs.

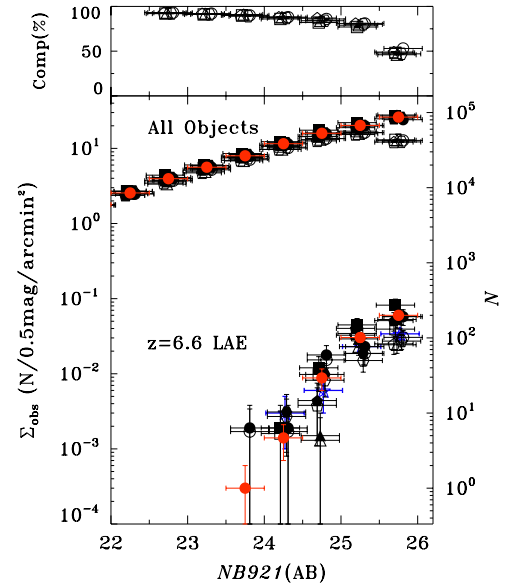


Figure 5. Top panel: detection completeness of our $NB921$ images in percent. Circles, hexagons, triangles, squares, and pentagons represent the completeness of a magnitude bin ($\Delta m = 0.5$ mag) in the five subfields, SXDS-C, SXDS-N, SXDS-S, SXDS-E, and SXDS-W, respectively. For presentation purposes, we slightly shift all the points along the abscissa. Bottom panel: surface densities of objects detected in the $NB921$ data. The lower and upper points indicate surface densities of our $z = 6.6$ LAEs and all the objects detected in the narrow band, respectively. Black circles, hexagons, triangles, squares, and pentagons plot the surface densities in the five subfields of SXDS-C, SXDS-N, SXDS-S, SXDS-E, and SXDS-W, respectively. We distinguish between the raw and completeness-corrected surface densities with the open and filled symbols, respectively. The red filled circles represent the surface density averaged over our entire survey field. The errors are given by Poisson statistics for black symbols, while the errors of red symbols are the geometric mean of Poisson errors and cosmic variances calculated from Equation (3). To avoid overlaps of points, we slightly shift all the black points along the abscissa with respect to the corresponding red filled circles. The right vertical axis indicates the number of objects, i.e., $N/(0.5\text{mag})$, identified in our entire survey area. Blue stars denote the surface density of $z \simeq 6.6$ LAEs obtained by Taniguchi et al. (2005).

Table 2
LAEs with Spectroscopic Redshifts

Object Name	α (J2000)	δ (J2000)	z	m_{NB} (mag)	$m_{z'}$ (mag)	$L(\text{Ly}\alpha)$ ($10^{43} \text{ erg s}^{-1}$)	ΔV_{FWHM} (km s^{-1})	EW_0 (\AA)	M_{UV} (mag)	SFR ($M_{\odot} \text{ yr}^{-1}$)
(1)	(2)	(3)	(4)	(5)	(6)	(7)	(8)	(9)	(10)	(11)
<i>N B921-C-106098</i>	2:17:03.4908	−4:56:19.158	6.589	24.7	26.8	1.2 ± 0.1	269 ± 37	$105.9^{+0}_{-65.4}$	$\simeq -20.2$	$\simeq 6.6$
<i>N B921-C-22057</i>	2:18:20.6670	−5:11:09.664	6.575	24.9	>27.7	1.0 ± 0.1	304 ± 58	$\gtrsim 100$	$\lesssim -19.9$	$\lesssim 5$
<i>N B921-C-34609</i>	2:18:19.3797	−5:09:00.550	6.563	24.8	27.3	0.9 ± 0.2	247 ± 98	$76.6^{+0}_{-57.1}$	$\lesssim -19.9$	$\lesssim 5$
<i>N B921-C-36215^a</i>	2:17:57.5630	−5:08:44.446	6.595	23.5	25.9	3.9 ± 0.2	267 ± 32	$116.5^{+179.5}_{-47.3}$	-21.1 ± 0.7	15.0 ± 9.7
<i>N B921-C-43803</i>	2:18:26.9734	−5:07:26.828	6.554	25.0	26.9	0.7 ± 0.2	199 ± 190	$32.2^{+828.2}_{-21.3}$	$\simeq -20.7$	$\simeq 10.3$
<i>N B921-C-50823^b</i>	2:17:02.5772	−5:06:04.480	6.545	24.8	26.9	0.9 ± 0.3	257 ± 69	$52.9^{+0}_{-35.8}$	$\simeq -20.5$	$\simeq 9.0$
<i>N B921-C-65683</i>	2:17:01.4777	−5:03:09.291	6.493	24.7	26.1	3.5 ± 12.7	329 ± 70	$\gtrsim 100$	$\lesssim -19.9$	$\lesssim 5$
<i>N B921-N-71598</i>	2:18:44.6534	−4:36:36.501	6.621	24.7	27.4	2.6 ± 0.3	367 ± 46	$\gtrsim 100$	$\lesssim -19.9$	$\lesssim 5$
<i>N B921-N-77765</i>	2:18:23.5317	−4:35:24.193	6.519	24.7	26.4	0.4 ± 0.8	266 ± 80	$45.2^{+0}_{-39.4}$	-21.6 ± 0.7	22.9 ± 14.8
<i>N B921-N-79144</i>	2:18:27.0289	−4:35:08.216	6.511	24.1	25.7	0.9 ± 1.2	317 ± 49	$24.8^{+0}_{-19.5}$	-22.2 ± 0.4	42.7 ± 15.7
<i>N B921-W-25755</i>	2:16:58.2805	−4:55:56.703	6.573	25.1	>27.7	0.7 ± 0.2	134 ± 42	$145.1^{+0}_{-115.8}$	$\lesssim -19.9$	$\lesssim 5$
<i>N B921-W-30717</i>	2:16:54.5645	−4:55:56.788	6.617	25.3	26.8	1.3 ± 0.2	246 ± 44	$153.0^{+0}_{-101.4}$	$\simeq -20.1$	$\simeq 5.9$
<i>N B921-W-30999^b</i>	2:16:54.3945	−5:00:04.162	6.512	25.1	>27.7	1.3 ± 0.8	185 ± 25	$\gtrsim 100$	$\lesssim -19.9$	$\lesssim 5$
<i>N B921-W-31790^b</i>	2:16:53.9169	−5:06:01.379	6.590	25.8	>27.7	0.4 ± 0.1	142 ± 154	$45.9^{+0}_{-32.9}$	$\lesssim -19.9$	$\lesssim 5$
<i>N B921-W-35578</i>	2:16:50.9037	−5:10:16.221	6.535	25.4	>27.7	0.6 ± 0.3	279 ± 210	$104.4^{+0}_{-89.0}$	$\lesssim -19.9$	$\lesssim 5$
<i>N B921-W-36217</i>	2:16:50.4202	−5:05:45.130	6.586	25.5	27.3	0.5 ± 0.2	128 ± 145	$34.7^{+1045.6}_{-23.3}$	$\lesssim -19.9$	$\lesssim 5$

Notes. (1) Object ID; (2, 3) R.A. and decl.; (4) redshift measured with an $\text{Ly}\alpha$ line; (5, 6) magnitudes in *N B921* (m_{NB}) and z' ($m_{z'}$). *N B921* is a total magnitude, while z' is a $2''$ aperture magnitude. The lower limit of $m_{z'}$ corresponds to a 1σ limit; (7) $\text{Ly}\alpha$ luminosity in $10^{43} \text{ erg s}^{-1}$; (8) FWHM velocity width in km s^{-1} ; (9) rest-frame apparent equivalent width of $\text{Ly}\alpha$ emission line; (10) UV total magnitude; (11) star formation rate estimated from the UV magnitude based on Madau et al. (1998). The quantities of columns (7)–(10) are estimated from *N B921* and z' photometry.

^a This object is the giant LAE, *Himiko* (Ouchi et al. 2009a). The EW_0 , M_{UV} , and SFR values listed here are slightly different from those shown in Ouchi et al. (2009a). In this table, we present values based on measurements of $2''$ aperture magnitudes to maximize the S/N for the other sources which are mostly fainter than *Himiko*. For consistency, the values of *Himiko* are based on $2''$ aperture magnitudes in this table. On the other hand, Ouchi et al. (2009a) estimate these values from total magnitudes for the bright object of *Himiko* to minimize systematic errors.

^b $\text{Ly}\alpha$ emission lines are doubly confirmed with our two independent spectra taken by our redundant observations (see Section 2.3).

spectroscopy have already confirmed 70% of our LAEs at $\log L_{\text{Ly}\alpha} > 43.0 \text{ erg s}^{-1}$, and found no contaminants in our sample (M. Ouchi et al. 2010, in preparation). Although the effect of contaminants may be negligible, we use this upper limit of contamination ($f_{\text{cont}} \simeq 30\%$) to derive the upper limits of our measurements in Section 4.

3.2. Surface Number Density and Cosmic Variance

The bottom panel of Figure 5 shows surface densities of LAEs and all narrowband-detected objects (designated as “All Objects”). Red circles are the average surface densities. Black points with five different symbols indicate the surface densities in the five subfields ($\simeq 0.2 \text{ deg}^2$) of Suprime-Cam, i.e., SXDS-C, -N, -S, -E, and -W. The detection completeness correction is applied based on the simulation results described in Section 3.1. After the completeness correction, surface densities of $z = 6.6$ LAEs among the five subfields differ up to by a factor of ~ 2 in faint magnitude bins ($N B921 = 25\text{--}26$) and a factor of ~ 10 in bright magnitude bins ($N B921 < 25$), while the difference for “All Objects” is negligibly small. Accordingly, the large variance of $z = 6.6$ LAEs is not due to artifacts, but is real. These large differences of LAE surface densities probably come from the combination of cosmic variance and Poisson errors. Following the procedures used in Ouchi et al. (2008), we evaluate the cosmic variance in our survey area, σ_g , with

$$\sigma_g = \sigma_{g:\text{lsf}}(\sigma_{\text{DM}}/\sigma_{\text{DM:lsf}}), \quad (3)$$

$$\sigma_{g:\text{lsf}}^2 = [(\langle \Sigma_{g:\text{lsf}} - \bar{\Sigma}_g \rangle^2) - \bar{\Sigma}_g] / \bar{\Sigma}_g^2, \quad (4)$$

where σ_{DM} and $\sigma_{\text{DM:lsf}}$ are the rms fluctuation of dark matter in all of the survey volume and the volume of the five subfields ($\simeq 0.2 \text{ deg}^2$), respectively. We calculate the fluctuations of dark matter with the power spectrum, adopting the transfer function given by Bardeen et al. (1986). $\sigma_{g:\text{lsf}}$ is the fluctuation of number density of LAEs for one subfield. $\Sigma_{g:\text{lsf}}$ and $\bar{\Sigma}_g$ are LAE’s surface densities in a subfield and the entire survey areas, respectively.

Since these estimates of cosmic variance are based on a large but single contiguous field, it is important to check whether our field is located at the sky of an overdense or underdense region. Moreover, a large-scale overdensity or underdensity of $\text{Ly}\alpha$ sources could also be produced by an inhomogeneous distribution of $\text{Ly}\alpha$ absorbers (i.e., neutral hydrogen) along the line of sight. In Figure 5, we compare the surface densities of our LAEs with those selected with the same *N B921* filter in a completely independent sky of $\simeq 0.2 \text{ deg}^2$ SDF (Taniguchi et al. 2005; see also Kashikawa et al. 2006). We find that the surface densities of our $z = 6.6$ LAEs are consistent with those of Taniguchi et al. (2005) within the scatters and Poisson errors of our five subfields. Moreover, Figure 5 shows that Taniguchi et al.’s measurements scatter around our average surface-density curve. Thus, we conclude that our field has neither the signature of overdensity nor underdensity, and that our five subfields appear to represent the average cosmic variance.

3.3. $\text{Ly}\alpha$ Luminosity Function

We derive the $\text{Ly}\alpha$ LF of LAEs at $z = 6.6$ in the same manner as Ouchi et al. (2008). We obtain the number densities of LAEs in each magnitude bin by dividing the observed number counts

of LAEs by the effective survey volume defined as the FWHM of the $NB921$ bandpass times the area of the survey. Here, we calculate the $\text{Ly}\alpha$ luminosity of each object with the response curves of narrow and broad bands by subtracting the continuum emission measured from the continuum magnitude from the total luminosity in the narrow band. In this calculation, we use the total magnitude of narrowband images. The continuum emission is estimated by the narrowband excess color defined with a $2''$ aperture, so as to keep high S/Ns and to avoid the effects of source confusion on broadband images with high source density. $\text{Ly}\alpha$ luminosity estimates of this photometry technique are tested for $z = 3\text{--}6$ LAEs in Figure 15 of Ouchi et al. (2008), which verifies that the ratios of these luminosity estimates to independent spectroscopy measurements are about unity on average.

Although this procedure of $\text{Ly}\alpha$ LF derivation is a simple classical method that was taken by most of the previous studies (e.g., Ouchi et al. 2003; Ajiki et al. 2003; Hu et al. 2004; Malhotra & Rhoads 2004), there are two possible sources of uncertainties in $\text{Ly}\alpha$ LFs derived with this classical method. (1) The narrowband magnitude of LAEs of a fixed $\text{Ly}\alpha$ luminosity varies largely as a function of redshift. Thus, $\text{Ly}\alpha$ luminosity may be overestimated or underestimated for some LAEs. (2) The selection function of LAEs in terms of EW also changes with redshift; the minimum EW value corresponding to a given (fixed) narrowband excess, $z' - NB921$, becomes larger when the redshift of the object is far from the redshift corresponding to the center of the $NB921$ bandpass. To derive $\text{Ly}\alpha$ LF with no bias originating from (1) and (2), Ouchi et al. (2008) have carried out Monte Carlo simulations with a mock catalog of their $z = 3\text{--}6$ LAEs uniformly distributed in comoving space that are produced by a set of the Schechter parameters (α, ϕ^*, L^*) and a Gaussian sigma for a probability distribution of EW_0 . Figures 16–18 of Ouchi et al. (2008) compare LFs from the unbiased simulations with those from the classical method, and indicate that the LFs from the classical method are consistent with those from the simulations. This is because the uncertainties (1) and (2) in the classical method are negligible and/or cancel out (Ouchi et al. 2008). Thus, our simple classical method gives good estimates of $\text{Ly}\alpha$ LF.

Figure 6 presents the $\text{Ly}\alpha$ LF of our LAEs at $z = 6.6$. Note that we have corrected the detection completeness by weighting with f_{det} measured in Section 3.1. To check the cosmic variance and the accuracy of our results, we plot the estimates of LFs from the entire 3238 arcmin^2 (red filled circles), together with those from the five subfields (black open symbols). In Figure 6, we calculate cosmic variances with Equation (3), and include these uncertainties in the error bars of LFs of the entire field. We find that the scatters of the measurements are large among the five subfields with differences by up to a factor of $\simeq 10$, although the typical scatters of the subfield results are not far beyond the errors of Poisson statistics.

We plot the previous measurements of $\text{Ly}\alpha$ LFs at $z \simeq 6.6$ in Figure 6. The previous measurements of $\text{Ly}\alpha$ LFs show large scatters. If one compares the LFs of Malhotra & Rhoads (2004; dotted line), Hu et al. (2005; crosses), and Kashikawa et al. (2006; stars), which are derived from a moderate number of LAEs and a moderately wide field, their measurements do not appear to agree. This large difference causes a long-standing argument of $\text{Ly}\alpha$ LF evolution between $z = 5.7$ and 6.6 . However, all of these previous measurements fall about within the scatters and errors of LFs derived from our five subfields each with a $\sim 0.2 \text{ deg}^2$ area. Thus, the discrepancies of LF

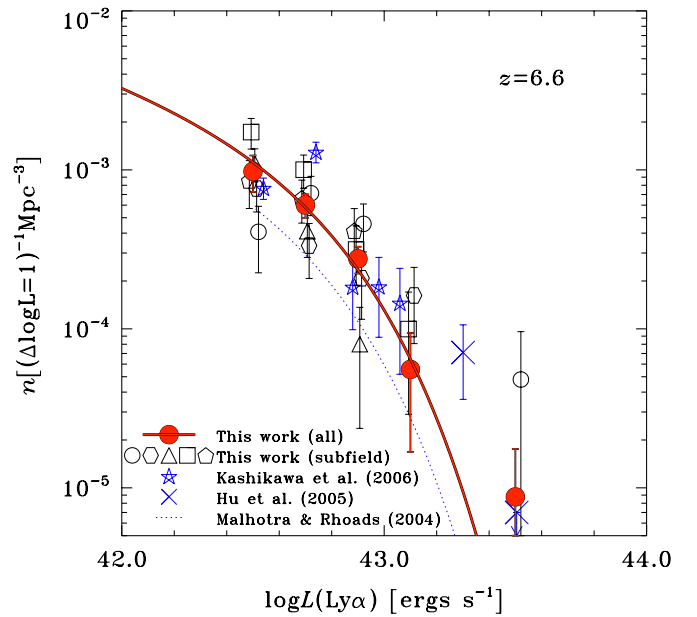


Figure 6. LFs of LAEs at $z = 6.6$, together with those of previous measurements for $z = 6.5\text{--}6.6$ LAEs. Filled red circles denote the best-estimate LF at $z = 6.6$ from our SXDS data. The error bars include uncertainties from statistics and cosmic variance (Equation (3)). Black open circles, hexagons, triangles, squares, and pentagons represent the LFs of five $\sim 0.2 \text{ deg}^2$ subfields, SXDS-C, SXDS-N, SXDS-S, SXDS-E, and SXDS-W, respectively. In order to avoid the overlaps of points, we slightly shift all the open symbols along the abscissa with respect to the corresponding red filled circles. The blue star marks present $z \simeq 6.6$ LF derived in the $\sim 0.2 \text{ deg}^2$ SDF by Kashikawa et al. (2006, photometric sample), while blue crosses are the measurement and upper limit of $z = 6.5$ LF given by Hu et al. (2005). The blue dotted line shows the LF estimated by Malhotra & Rhoads (2004). The red solid line is the best-fit Schechter function to the combination of SXDS and SDF LFs at $z = 6.6$.

measurements between these previous studies are probably due to the combination of cosmic variances and small statistics. Because our $z = 6.6$ LFs from the five subfields cover the range of measurements of Malhotra & Rhoads (2004), Hu et al. (2005), and Kashikawa et al. (2006), we conclude that our LF measurements agree well with those derived in previous studies.

A Schechter function (Schechter 1976) is fit to the $\text{Ly}\alpha$ LFs composed of our large area data with cosmic variance errors and the previous LF estimate in the independent 876 arcmin^2 area of SDF (Kashikawa et al. 2006).¹³ The Schechter function is defined by

$$\phi(L)dL = \phi^*(L/L^*)^\alpha \exp(-L/L^*)d(L/L^*). \quad (5)$$

With a total of 265 ($= 207 + 58$) LAEs at $z \simeq 6.6$ in a total area of 4114 arcmin^2 data in the SXDS and SDF, we obtain the best-fit Schechter parameters of $\phi^* = 8.5^{+3.0}_{-2.2} \times 10^{-4} \text{ Mpc}^{-3}$ and $L^*_{\text{Ly}\alpha} = 4.4^{+0.6}_{-0.6} \times 10^{42} \text{ erg s}^{-1}$ with a fixed $\alpha = -1.5$, which are summarized in Table 3. Because the difference in χ^2 for α values is insignificant, we fix α to -1.5 , which is a fiducial value used for low- z $\text{Ly}\alpha$ LFs (e.g., Malhotra & Rhoads 2004; Kashikawa et al. 2006; Ouchi et al. 2008). The best-fit Schechter function is shown in Figure 6 with the red solid line. We also estimate the best-fit Schechter parameters with a fixed $\alpha = -1.7$, because the value of $\alpha \simeq -1.7$ is

¹³ Twenty-six out of 29 LAEs used in Malhotra & Rhoads (2004) are provided from a subsample of the SDF data (Taniguchi et al. 2005; Kashikawa et al. 2006). To avoid using the same LAE data, we do not include Malhotra & Rhoads (2004) data points for our Schechter fitting. We also do not use data points in papers that are not published yet in a refereed journal.

Table 3
Ly α Luminosity Function

z	ϕ^* (10^{-4} Mpc^{-3})	$L_{\text{Ly}\alpha}^*$ ^a ($10^{42} \text{ erg s}^{-1}$)	α	χ_r^2	n^{obs} (10^{-4} Mpc^{-3})	$\rho_{\text{Ly}\alpha}^{\text{obs}}$ ($10^{39} \text{ erg s}^{-1} \text{ Mpc}^{-3}$)	$\rho_{\text{Ly}\alpha}^{\text{tot}}$ ($10^{39} \text{ erg s}^{-1} \text{ Mpc}^{-3}$)
(1)	(2)	(3)	(4)	(5)	(6)	(7)	(8)
6.6	$8.5^{+3.0}_{-2.2}$	$4.4^{+0.6}_{-0.6}$	$-1.5(\text{fix})$	1.60	$4.1^{+0.9}_{-0.8}$	$1.9^{+0.5}_{-0.4}$	$6.6^{+1.0}_{-0.8}$

Notes. (1) Redshift; (2)–(4) best-fit Schechter parameters for ϕ^* and $L_{\text{Ly}\alpha}^*$, respectively, α is fixed to -1.5 ; (5) reduced χ^2 of the fitting; (6)–(7) number densities and Ly α luminosity densities calculated with the best-fit Schechter parameters down to the observed limit of Ly α luminosity, i.e., $\log L_{\text{Ly}\alpha} = 42.4 \text{ erg s}^{-1}$; (8) inferred total Ly α luminosity densities integrated down to $L_{\text{Ly}\alpha} = 0$ with the best-fit Schechter parameters.

^a $L_{\text{Ly}\alpha}^*$ is the apparent value, i.e., observed Ly α luminosity with no correction for IGM absorption.

recently reported for $z = 2$ – 6 LAEs (Cassata et al. 2010; see also Rauch et al. 2008) as well as $z \sim 7$ dropouts (e.g., Ouchi et al. 2009b; Oesch et al. 2010; McLure et al. 2010). The best-fit parameters for $\alpha = -1.7$ are $\phi^* = 6.9^{+2.6}_{-1.9} \times 10^{-4} \text{ Mpc}^{-3}$ and $L_{\text{Ly}\alpha}^* = 4.9^{+0.9}_{-0.7} \times 10^{42} \text{ erg s}^{-1}$. Note that our data point at the bright end ($\log L(\text{Ly}\alpha) = 43.5 \text{ erg s}^{-1}$) appears to exceed the best-fit Schechter function in Figure 6, although the data point is consistent with the best-fit Schechter function within the error bar that extends down to 0. This excess data point is solely made by one exceptional LAE that is an extended giant LAE, *Himiko*, reported in Ouchi et al. (2009a).

3.4. Evolution of Ly α Luminosity Function

Figure 7 compares our Ly α LF of LAEs at $z = 6.6$ with those at $z = 3.1$ and 5.7 . Note that these low- z LFs are derived from large LAE samples of wide-field SXDS (Ouchi et al. 2008) with the same procedures (including cosmic variance errors) and similar data sets taken with the same instrument. In this sense, there are little systematics among different redshift results caused by the sample selection and measurement technique. While the LFs do not change within error bars from $z = 3.1$ to 5.7 (Ouchi et al. 2008), the LF decreases from $z = 5.7$ to 6.6 beyond sizes of errors, i.e., uncertainties of statistics and cosmic variance. To quantify this decrease, we present in Figure 8 error ellipses of Schechter parameters of LFs at $z = 6.6$, together with those at $z = 5.7$ from Ouchi et al. (2008). Figure 8 shows that error contours of $z = 6.6$ and 5.7 differ at the $>90\%$ significance level. Even if we consider the maximum effect of contamination (Section 3.1), there exists a significant evolution of the Ly α LF. Because a contamination correction pushes down our $z = 6.6$ LAE LF toward low number density in Figure 7, an inclusion of contamination correction even strengthens the evolutionary tendency. The EW_0 limit of our $z = 6.6$ LAE sample is $\gtrsim 14 \text{ \AA}$, which is different from and smaller than that of the $z = 5.7$ LAE sample ($\text{EW}_0 \gtrsim 27 \text{ \AA}$; Ouchi et al. 2008) by $\Delta \text{EW}_0 \simeq 10 \text{ \AA}$. Ouchi et al. (2008) have investigated a possible false evolution given by a choice of EW_0 limit for LAE samples at different redshifts. They use LAE samples at $z = 3$ – 6 whose EW_0 limits differ by 30 \AA ($\text{EW}_0 \gtrsim 30$ – 60 \AA), and fit a number- EW_0 distribution of the samples with a Gaussian function to obtain inferred Schechter parameters for all $z = 3$ – 6 LAE samples with the same EW_0 limit of $\text{EW}_0 = 0$. Ouchi et al. (2008) find that the inferred ϕ^* is different from the original ϕ^* by only $\lesssim 10\%$, and claim that the choice of EW_0 limits provides negligible impact on the results of Ly α LF evolution. This is true if the difference of the EW_0 limit is much smaller than the best-fit Gaussian sigma of the number- EW_0 distribution ($\gtrsim 130 \text{ \AA}$ for $z = 3$ – 6 ; Ouchi et al. 2008). Although we cannot carry out the similar investigation for our $z = 6.6$ sample due to poorly

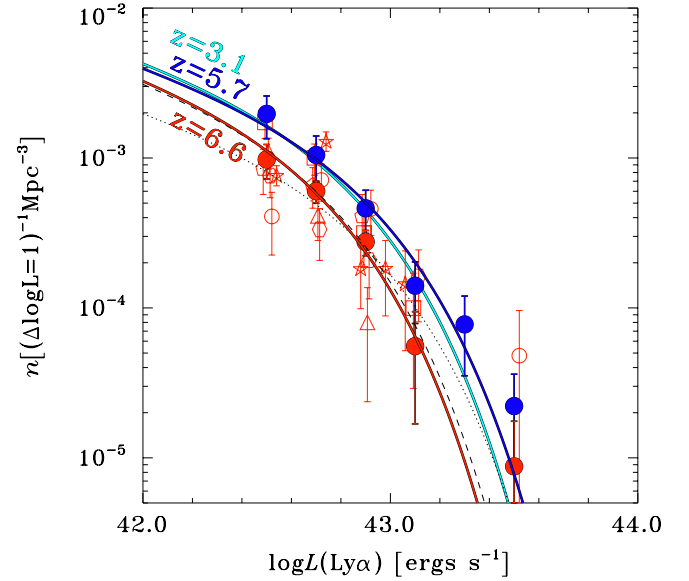


Figure 7. Evolution of Ly α LFs up to $z = 6.6$. Red filled circles are the best estimates of $z = 6.6$ LAEs from the entire SXDS sample and red solid line is the best-fit Schechter function of $z = 6.6$ LAEs. Blue filled circles and the solid line are data points and the best-fit Schechter function, respectively, of $z = 5.7$ LAEs given by Ouchi et al. (2008). Note that the error bars of $z = 6.6$ and 5.7 data points (red and blue filled circles) represent uncertainties from statistics and cosmic variance. The cyan solid line is the best-fit Schechter function of $z = 3.1$ LAEs (Ouchi et al. 2008). The LF decreases from $z = 5.7$ to 6.6 significantly, while no significant evolution can be found between $z = 3.1$ and 5.7 . For comparison, we plot LF estimates from each of the five $\sim 0.2 \text{ deg}^2$ subfields with the same open symbols as found in Figure 6. These open symbols illustrate that with the data of a single $\sim 0.2 \text{ deg}^2$ field alone (e.g., open circles down to $\log L_{\text{Ly}\alpha} \simeq 42.6$), which is a typical survey size of previous studies, it is difficult to distinguish whether or not $z = 6.6$ LFs show evolution (decrease) with respect to $z = 5.7$. Dashed and dotted lines represent the best-fit Schechter functions to our $z = 6.6$ LF with a ϕ^* and L^* fixed to that of $z = 5.7$, respectively.

constrained EW_0 values of our LAEs (see Section 6.1.1 for more details), it is very likely that the bias introduced by the different EW_0 limits ($\Delta \text{EW}_0 \simeq 10 \text{ \AA}$) is smaller than that found in Ouchi et al. (2008), $\lesssim 10\%$ corresponding to $\lesssim 0.04 \text{ dex}$ in ϕ^* . This small bias of $\lesssim 0.04 \text{ dex}$ does not affect to the conclusion of LF decrease in Figure 8. Moreover, the conclusion of LF decrease is probably, again, even strengthened, because corrections for the incompleteness of the EW_0 limits raise ϕ^* of the $z = 5.7$ sample ($\text{EW}_0 \gtrsim 27 \text{ \AA}$) more than that of our $z = 6.6$ sample ($\text{EW}_0 \gtrsim 14 \text{ \AA}$) in the case of the same number- EW_0 distribution at $z = 5.7$ and 6.6 . We plot error contours obtained by Kashikawa et al. (2006) in Figure 8 for comparison. Because the measurements of Kashikawa et al. (2006) do not include cosmic variance errors, their contours are relatively small.

Although the errors of our measurements are not small, Figure 8 implies that a decrease in L^* would be the

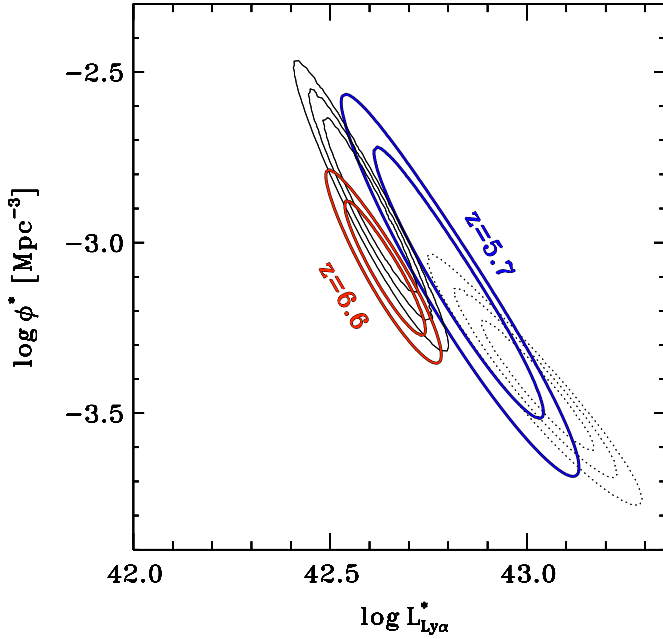


Figure 8. Error ellipses of our Schechter parameters, $L_{\text{Ly}\alpha}^*$ and ϕ^* . Red contours represent the fit of the $z = 6.6$ LF with the fixed slope of $\alpha = -1.5$ based on SXDS and SDF data. The inner and outer contours indicate 68% and 90% confidence levels, respectively, which include cosmic variance errors. Blue contours denote $z = 5.7$ LFs given by Ouchi et al. (2008), which are similarly derived with cosmic variance errors. For a fair comparison with our $z = 6.6$ LF, we show error ellipses of the $z = 5.7$ LF derived by the classical method (see more details in Ouchi et al. 2008). The error ellipses of the $z = 5.7$ LF are larger than those of our $z = 6.6$ LF. This is because the data of $z = 5.7$ LF have more uncertainties of cosmic variance. Black solid and dotted lines indicate 1σ , 2σ , and 3σ confidence levels of $z = 6.6$ and $z = 5.7$ LFs with no cosmic variance errors previously derived solely with the smaller data of SDF (Kashikawa et al. 2006).

dominant factor of the LF evolution from $z = 5.7$ to 6.6. We investigate whether pure number or pure luminosity evolutions are dominant. We fix either L^* or ϕ^* of the $z = 5.7$ LF, and carry out Schechter function fitting to our $z = 6.6$ LF. Figure 7 plots the best-fit Schechter functions for the two scenarios of the pure number (dotted line) and pure luminosity (dashed line) evolutions from $z = 5.7$ to 6.6. We obtain $\phi^*(z = 6.6) = 0.5\phi^*(z = 5.7)$ for the pure number evolution and $L^*(z = 6.6) = 0.7L^*(z = 5.7)$ for the pure luminosity evolution. The fitting to the pure luminosity evolution is better than that to the pure number evolution, and the χ^2 value of the pure luminosity evolution is smaller than that of the pure number evolution by 7.40. We confirm that, irrespective of α , the pure luminosity evolution is more favorable than the pure number evolution based on our Schechter function fitting with the fixed best-fit L^* or ϕ^* of the $z = 5.7$ LF in the cases of $\alpha = -1.0$ and -2.0 (Table 5 of Ouchi et al. 2008) that bracket a reasonable range of α . In the case of pure luminosity evolution, the decrease of luminosity is 30% from $z = 5.7$ to 6.6. This decrease is smaller than that obtained by Kashikawa et al. (2006) who claim a luminosity decrease by 0.75 mag. Moreover, this 30% decrease is too small to be distinguished by any previous studies that include large statistical and cosmic variance errors. We plot LF estimates from each of the five $\sim 0.2 \text{ deg}^2$ subfields in Figure 7 with the same open symbols as in Figure 6. These open symbols illustrate that with the data of a single $\sim 0.2 \text{ deg}^2$ field alone, which is a typical survey size of previous studies, it is difficult to distinguish whether or not $z = 6.6$ LFs show evolution (decrease) with respect to $z = 5.7$. We find the decrease of $\text{Ly}\alpha$

LF between $z = 5.7$ and 6.6 at the $>90\%$ significance level. On the other hand, Malhotra & Rhoads (2004) claim no evolution between $z = 5.7$ and 6.6, which appears to contradict our findings. However, Malhotra & Rhoads (2004) carefully state that an $\text{Ly}\alpha$ flux of $z = 6.5$ LAEs is not attenuated by a factor of 3, i.e., 300%, compared with $z = 5.7$ LAEs. In other words, Malhotra & Rhoads (2004) conclude no evolution of $\text{Ly}\alpha$ LF within large uncertainties of their estimate (300%), and claim nothing about the small 30% level evolution such as we find. In this sense, the conclusion of Malhotra & Rhoads (2004) quantitatively agrees with ours. Another issue is the baseline LF at $z = 5.7$ used in these comparisons. The baseline $z = 5.7$ LFs are different between our study, Malhotra & Rhoads (2004), and Hu et al. (2005). We use the up-to-date $z = 5.7$ LF of Ouchi et al. (2008) shown in Figure 7, while Malhotra & Rhoads (2004) and Hu et al. (2005) use their own LFs. Figure 19 of Ouchi et al. (2008) compares all of these three $z = 5.7$ LFs, and indicates that our baseline $z = 5.7$ LF of Ouchi et al. (2008) comes around the middle of previous results and falls between those of Malhotra & Rhoads (2004) and Hu et al. (2004); the one used by Malhotra & Rhoads (2004) is placed below ours, while the one used by Hu et al. (2005) is above ours. Because we see exactly the same tendency in $z = 6.6$ LF measurements in Figure 6 (i.e., Malhotra & Rhoads's LF below ours, and Hu et al.'s LF above ours), the “no evolution” is more clearly found in Figure 2 of Malhotra & Rhoads (2004) and Figure 3 of Hu et al. (2005), even without considering their large uncertainties of statistics and cosmic variance.

In summary, we conclude that $\text{Ly}\alpha$ LF decreases from $z = 5.7$ to 6.6, and that no evolution of $\text{Ly}\alpha$ LF is ruled out at the $>90\%$ significance level with errors including uncertainties of statistics and cosmic variance. The pure luminosity evolution is more preferable to the pure number density evolution. If the pure luminosity evolution is assumed, $L_{\text{Ly}\alpha}^*$ dims by 30% from $z = 5.7$ to 6.6.

4. SPATIAL DISTRIBUTION

In this section, we discuss clustering of our $z = 6.6$ LAEs. Since we need to know an evolutionary trend of clustering at $z = 3$ –6 to distinguish cosmic reionization and galaxy evolution effects at $z = 6.6$ (Section 6.1.2), we derive correlation functions of not only our 207 LAEs at $z = 6.6$, but also those at lower redshifts. We use 356, 101, and 401 LAEs at $z = 3.1$, 3.7, and 5.7, respectively, given by Ouchi et al. (2008). Since we have a moderately large number ($\gtrsim 200$) of LAEs at $z = 3.1$, 5.7, and 6.6 down to narrowband magnitude limits of 25.3, 26.0, and 26.0, respectively, we make bright subsamples with narrowband limiting magnitudes brighter by 0.5 mag: 24.8 ($z = 3.1$), 25.5 ($z = 5.7$), and 25.5 ($z = 6.6$). Readers should refer to Ouchi et al. (2008) for the details of the SXDS $z = 3.1$ –5.7 LAE samples.

4.1. Angular Correlation Function

Figures 9 and 10 present sky distributions of the $z = 3.1$ –5.7 LAEs and our $z = 6.6$ LAEs, respectively. In order to quantitatively measure the inhomogeneity of spatial distribution, we derive the two-point ACF in the same manner as Ouchi et al. (2003, 2004b, 2005b). According to Landy & Szalay (1993), the ACF is calculated by

$$\omega_{\text{obs}}(\theta) = [\text{DD}(\theta) - 2\text{DR}(\theta) + \text{RR}(\theta)]/\text{RR}(\theta), \quad (6)$$

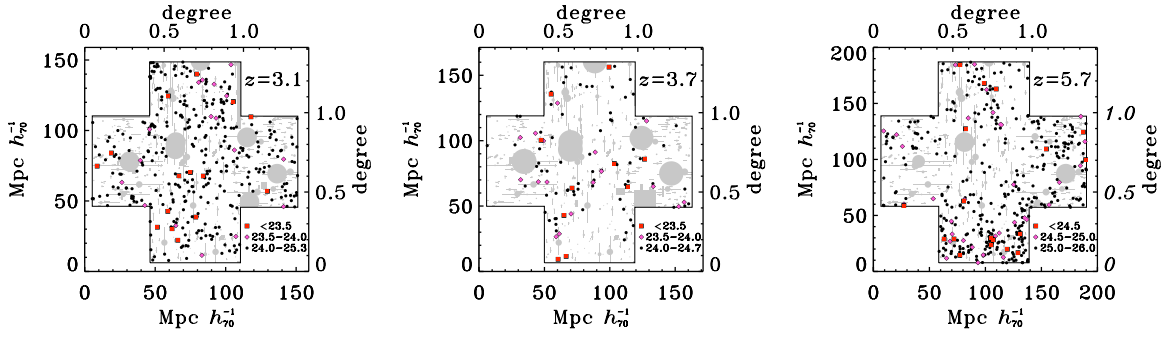


Figure 9. Sky distribution of the SXDS LAEs at $z = 3.1$ (left), 3.7 (center), and 5.7 (right) obtained by Ouchi et al. (2008). Red squares, magenta diamonds, and black circles present positions of narrowband (bright, medium bright, and faint) LAEs, respectively, in narrowband magnitudes of ($NB503 < 23.5$, $23.5 \leq NB503 < 24.0$, $24.0 \leq NB503 < 25.3$; left panel), ($NB570 < 23.5$, $23.5 \leq NB570 < 24.0$, $24.0 \leq NB570 < 24.7$; center panel), and ($NB816 < 24.5$, $24.5 \leq NB816 < 25.0$, $25.0 \leq NB503 < 26.0$; right panel). The gray shades represent masked areas that are not used for sample selection. The scale on the map is marked in both degrees and the projected distance in comoving megaparsecs at each redshift.

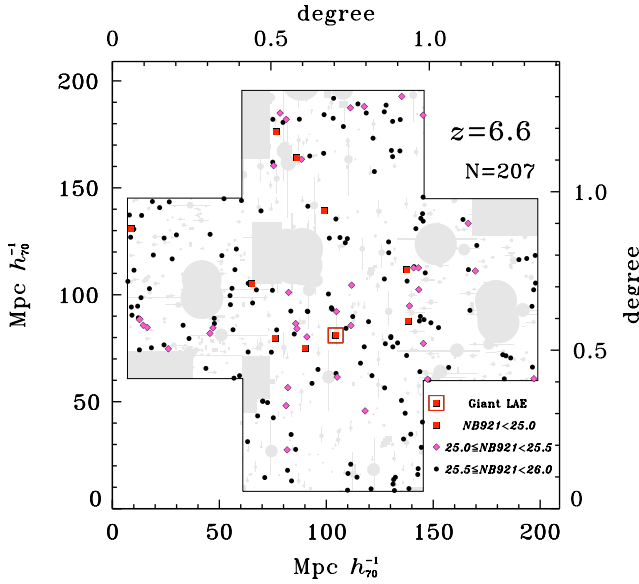


Figure 10. Same as Figure 9, but for our 207 LAEs at $z = 6.565 \pm 0.054$. Red squares, magenta diamonds, and black circles show positions of bright ($NB921 < 25.0$), medium bright ($25.0 \leq NB921 \leq 25.5$), and faint ($25.5 \leq NB921 \leq 26.0$) LAEs, respectively. The red square highlighted with a red open square indicates the giant LAE, *Himiko*, with a bright and extended Ly α nebular at $z = 6.595$ reported by Ouchi et al. (2009a).

where $DD(\theta)$, $DR(\theta)$, and $RR(\theta)$ are numbers of galaxy–galaxy, galaxy–random, and random–random pairs normalized by the total number of pairs in each of the three samples. We first create a pure random sample composed of 100,000 sources with the same geometrical constraints as the data sample and estimate errors with the bootstrap technique (Ling et al. 1986). Figures 11 and 12 show the ACFs, $\omega_{\text{obs}}(\theta)$, of LAEs from the observations at $z = 3.1$ – 5.7 and 6.6 . We find significant clustering signals for our $z = 6.6$ LAEs as well as the $z = 3.1$ – 5.7 LAEs.

We then confirm that these clustering signals are not artifacts produced by the slight inhomogeneous quality over the images or occultation by foreground objects on the basis of our Monte Carlo simulations. We use mock catalogs of LAEs obtained by simulations of Ouchi et al. (2008), which have number counts and color distribution that agree with observational measurements. We generate 50,000 artificial LAEs based on the mock catalog, and distribute them randomly on the original 1 deg^2 narrowband and broadband images after adding Poisson noise according to their brightness. Since most of the LAEs

are nearly point sources, we assume profiles of PSFs that are the same as the original images. Then, we detect these simulated LAEs and measure their brightness in the same manner as the real LAEs. We iterate this process 10 times and select LAEs with the same color criteria as the real LAEs. We thus obtain $\sim 200,000$ simulation-based random sources at each redshift whose positions are affected by the inhomogeneity of LAE detectability and the occultation of foreground objects, and therefore slightly different from the pure random sample. We use these simulation-based random sources for our ACF calculation. Crosses in Figure 11 present estimates of ACFs with these random sources. The ACFs estimated with these simulation-based random sources (crosses) and the pure random-distribution sources (squares) are consistent. Accordingly, we conclude that the clustering signals are not artifacts given by the slight inhomogeneity of image qualities or the occultation of foreground objects.

To evaluate observational offsets included in $\omega_{\text{obs}}(\theta)$ due to the limited area and object number, we assume that the real ACF, $\omega(\theta)$, is approximated by the power law:

$$\omega(\theta) = A_{\omega} \theta^{-\beta}. \quad (7)$$

Then, the offset from the observed ACF, $\omega_{\text{obs}}(\theta)$, is given by the integral constraint, C (Groth & Peebles 1977), and the number of objects in the sample, N ,

$$\omega(\theta) = \omega_{\text{obs}}(\theta) + C + \frac{1}{N}, \quad (8)$$

$$C = \frac{\Sigma \text{RR}(\theta) A_{\omega} \theta^{-\beta}}{\Sigma \text{RR}(\theta)}. \quad (9)$$

The term $1/N$ in Equation (8) corrects for the difference between the number of object pairs, $N(N-1)/2$, and its approximation, $N^2/2$ (Peebles 1980). Note that most of the previous clustering studies for high- z galaxies neglect this $1/N$ term (e.g., Roche & Eales 1999; Daddi et al. 2000) probably because of their large samples. However, it should be applied for samples with a small number of objects such as LAE samples to obtain more accurate ACF at a large scale. The ACFs corrected with Equation (8) are also presented in Figures 11 and 12.

We fit the power law (Equation (7)) over $10'' < \theta < 1000''$ with the corrections. The lower limit of the fitting range, $\theta = 10''$, is placed because the one-halo term of high- z galaxies is dominant at this small scale (Ouchi et al. 2005b;

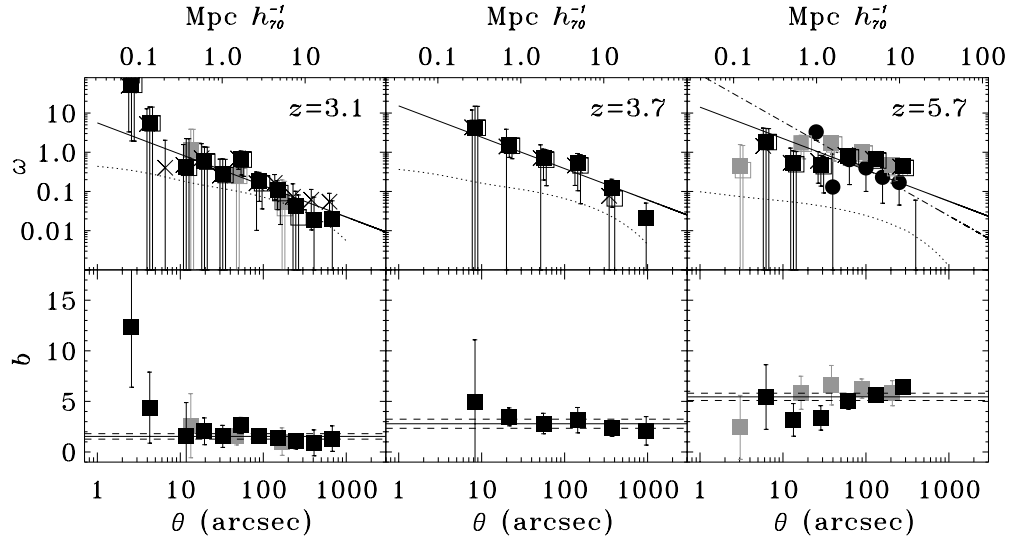


Figure 11. ACF and bias of the SXDS LAEs at $z = 3.1$ (left), 3.7 (center), and 5.7 (right). Top panels present ACFs and bottom panels show bias as a function of angular distance. Black filled and open squares indicate the best estimates for all LAEs with and without the corrections of limited area (i.e., integral constraints) and number (Equation (8)). Gray filled and open squares are the same, but for the bright subsamples, $NB503 < 24.7$ in the left panels and $NB816 < 25.5$ in the right panels. Crosses in the top panels represent ACFs calculated with the Monte Carlo simulation-based random sources that are artificial LAEs distributed and detected in the real images (see the text). In the top panels, solid lines are the best-fit power-law functions for all LAEs, while the dotted lines denote ACFs of underlying dark matter predicted by the CDM model (Peacock & Dodds 1996). In the bottom panels, solid and dashed lines present the best estimates of bias and the associated 1σ errors. In the top right panel, filled circles and dot-dashed line are ACF and the best-fit power law obtained by Murayama et al. (2007). The scale on the top axis denotes the projected distance in comoving megaparsecs at each redshift.

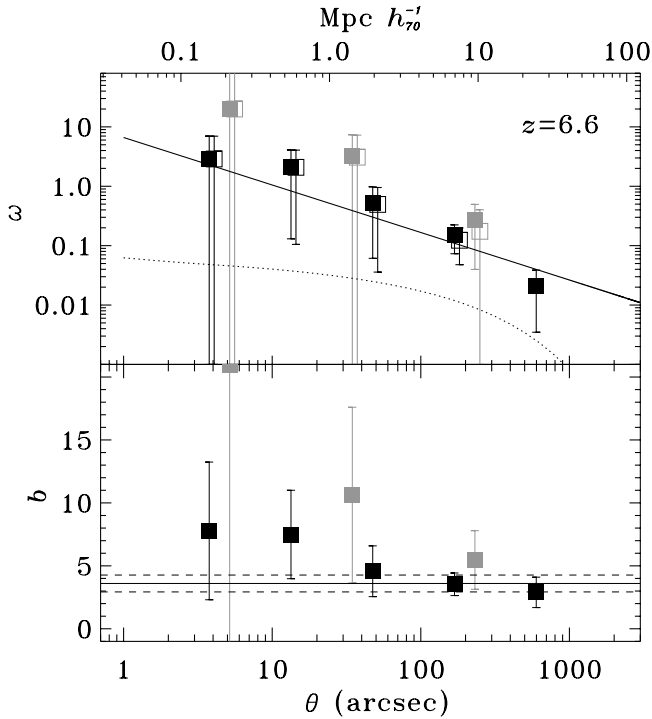


Figure 12. Same as Figure 11, but for our LAEs at $z = 6.6$. Gray filled and open squares are the estimates for the bright ($NB921 < 25.5$) subsample.

Lee et al. 2006; Hildebrandt et al. 2007, 2009). The upper limit of the range is nearly the limit of our ACF measurements with significant signals. We apply the upper limit of $400''$ for the $z = 5.7$ LAEs, since a large-scale clustering ($\gtrsim 20$ Mpc) with protoclusters is reported in this survey volume (Ouchi et al. 2005a). Because we obtain no meaningful constraints on β , we fix β with the fiducial value of 0.8 following the previous

clustering analyses (e.g., Ouchi et al. 2003; Gawiser et al. 2007; Kovač et al. 2007). We summarize the best-fit values in Table 4.

Foreground contamination to a galaxy sample dilutes the apparent clustering amplitude of galaxies. If the fraction of contaminants is f_c , the apparent A_ω value can be reduced by up to a factor of $(1 - f_c)^2$. The correlation amplitude with the contamination correction, A_ω^{\max} , is given by

$$A_\omega^{\max} = \frac{A_\omega}{(1 - f_c)^2}. \quad (10)$$

This is the maximum reduction of the correlation amplitude that occurs when the contaminants are not at all clustered. In reality, contaminants, if any, are the sum of foreground galaxies mostly at some specific redshifts, and thus would be clustered to some extent on the sky. We use the maximum values of f_c , and obtain maximal A_ω^{\max} values inferred from the LAE data. The maximum values of f_c are (0.13, 0.14, 0.25) for redshifts of (3.1, 3.7, 5.7) (Ouchi et al. 2008) and 0.33 for $z = 6.6$ (Section 3.1). In the following section, we will place conservative upper limits on correlation lengths and bias measurements with the maximal values of A_ω^{\max} .

4.2. Correlation Length and Bias

The spatial correlation function of galaxies is well approximated by a power law as

$$\xi = (r/r_0)^{-\gamma} \quad (11)$$

only with a subtle departure from the real spatial correlation function (Zehavi et al. 2004), where r is the spatial separation between two objects, r_0 is the correlation length, and γ is the slope of the power law. The correlation length, r_0 , is related to the correlation amplitude, A_ω , with the integral equation called

Table 4
Clustering Measurements

z	Sample	$C + 1/N$	A_ω (arcsec $^\beta$)	β	r_0 (h_{100}^{-1} Mpc)	r_0^{\max} (h_{100}^{-1} Mpc)
(1)	(2)	(3)	(4)	(5)	(6)	(7)
3.1	All ($NB503 < 25.3$)	1.99×10^{-2}	5.61 ± 2.46	0.80 (fix)	$1.70^{+0.39}_{-0.46}$	$1.99^{+0.45}_{-0.55}$
3.1	$NB503 < 24.8$	1.66×10^{-2}	3.13 ± 3.12	0.80 (fix)	$1.23^{+0.58}_{-1.18}$	$1.44^{+0.67}_{-1.37}$
3.7	All ($NB570 < 24.7$)	5.59×10^{-2}	15.24 ± 6.38	0.80 (fix)	$2.74^{+0.58}_{-0.72}$	$3.24^{+0.69}_{-0.85}$
5.7	All ($NB816 < 26.0$)	4.52×10^{-2}	14.13 ± 2.80	0.80 (fix)	$3.12^{+0.33}_{-0.36}$	$4.30^{+0.45}_{-0.50}$
5.7	$NB816 < 25.5$	8.76×10^{-2}	26.37 ± 6.59	0.80 (fix)	$4.41^{+0.59}_{-0.65}$	$6.08^{+0.80}_{-0.90}$
6.6	All ($NB921 < 26.0$)	2.53×10^{-2}	6.63 ± 3.73	0.80 (fix)	$2.31^{+0.65}_{-0.85}$	$3.60^{+1.02}_{-1.32}$
6.6	$NB921 < 25.5$	9.35×10^{-2}	23.25 ± 22.31	0.80 (fix)	$4.64^{+2.10}_{-3.86}$	$7.23^{+3.28}_{-6.01}$

Notes. (1) Redshift; (2) LAE sample; (3) offset value for A_ω that corrects for limited survey area and number (Equation (8)); (4) best-fit amplitude of power-law function for the ACF in arcsec $^\beta$; (5) the fixed β for the power-law fitting; (6)–(7) correlation lengths in h_{100}^{-1} Mpc, the best estimate and the maximally contamination-corrected r_0 in (6) and (7), respectively. To facilitate comparison with previous results, we express r_0 using h_{100} , the Hubble constant in units of $100 \text{ km s}^{-1} \text{ Mpc}^{-1}$, instead of $70 \text{ km s}^{-1} \text{ Mpc}^{-1}$.

the Limber equation (Peebles 1980; Efsthathiou et al. 1991),

$$A_\omega = k r_0^\gamma \int_0^\infty F(z) D_\theta^{1-\gamma}(z) N(z)^2 g(z) dz \left[\int_0^\infty N(z) dz \right]^{-2}, \quad (12)$$

where $F(z)$ ¹⁴ describes the redshift dependence of $\xi(r)$, $D_\theta(z)$ is the angular diameter distance, $N(z)$ is the redshift distribution of objects, $g(z) = H_0/c[(1+z)^2(1+\Omega_m z + \Omega_\Lambda((1+z)^{-2} - 1))^{1/2}]$, and k is a numerical constant, $k = \sqrt{\pi} \Gamma[(\gamma - 1)/2] / \Gamma(\gamma/2)$. The slope, β , of the ACF is related to γ by

$$\gamma = \beta + 1. \quad (13)$$

We adopt the redshift distribution of the LAEs calculated with the simulation output sources (i.e., referred to as simulation-based random sources in our Monte Carlo simulations; Section 4.1). The correlation lengths thus obtained are summarized in Table 4. These correlation lengths are expressed with h_{100} , the Hubble constant in units of 100 km s^{-1} , instead of 70 km s^{-1} , to facilitate comparison with previous results. In Table 4, we present r_0 and its upper limit, r_0^{\max} , that are the correlation lengths obtained from A_ω and its maximal value, A_ω^{\max} , respectively. The correlation lengths are typically $1\text{--}2 h_{100}^{-1} \text{ Mpc}$ at $z \sim 3$ and $2\text{--}6 h_{100}^{-1} \text{ Mpc}$ at $z = 4\text{--}6$. Our estimates of r_0 are consistent with the previous measurements. Ouchi et al. (2003) and Kovač et al. (2007) obtain (r_0, r_0^{\max}) of ($3.5 \pm 0.3, 6.2 \pm 0.5$) $h_{100}^{-1} \text{ Mpc}$ at $z = 4.9$ and ($3.20 \pm 0.42, 4.61 \pm 0.60$) $h_{100}^{-1} \text{ Mpc}$ at $z = 4.5$, respectively. Gawiser et al. (2007) and Guaita et al. (2010) estimate r_0 to be $2.5^{+0.6}_{-0.7} h_{100}^{-1} \text{ Mpc}$ at $z = 3.1$ and $3.4 \pm 0.6 h_{100}^{-1} \text{ Mpc}$ at $z = 2.1$, respectively, where r_0 is converted to values in units of $h_{100}^{-1} \text{ Mpc}$. At $z = 3.1$, the value of Gawiser et al. (2007) is slightly higher than that of our $z = 3.1$ LAEs, but these are still consistent within 1σ errors. The correlation length of our $z = 6.6$ LAEs is $r_0 = 2\text{--}5 h_{100}^{-1} \text{ Mpc}$, while that for r_0^{\max} is $3\text{--}7 h_{100}^{-1} \text{ Mpc}$, as presented in Table 4.

Note that these correlation lengths are estimated by the Limber equation (Equation (12)). Simon (2007) claims that the Limber equation is accurate for small galaxy separation but

breaks down beyond a certain separation that mainly depends on the width of galaxy distribution and distance. In this sense, Equation (12) is regarded as a Limber approximation that is valid only in a small angular separation. Simon (2007) presents the exact equation connecting the spatial and angular correlation functions, which is hereafter referred as Simon's equation. On the other hand, Sobral et al. (2010) have demonstrated that there is only a small, $\simeq 4\%$ level, difference between the correlation lengths calculated with Limber's and Simon's equations based on their NB-selected sample of H α emitters at $z = 0.8$. Although their survey area is similar to that of our study, it is not clear whether the Limber approximation gives only a negligible impact on our results at the different redshift of $z = 6.6$. We have compared ACFs calculated with Limber's and Simon's equations in the same manner as shown in Figure 4 of Sobral et al. (2010). We have found that there are no apparent differences between two results up to $\theta \sim 200''$. We have used our data of $10''\text{--}1000''$ for our power-law fitting that is mostly not affected by the bias of Limber approximation. Moreover, the ACFs of Limber's and Simon's equations differ only by a factor of ~ 2 even at θ near $1000''$, the largest angular separation of our fitting where the error of our data point is comparably large. Thus, the change in r_0 values is negligibly small for our galaxies at higher redshifts, compared with their relatively large statistical errors.

We define galaxy–dark matter bias in the framework of a Λ CDM model by

$$b_g(\theta)^2 \equiv \omega(\theta)/\omega_{\text{dm}}(\theta), \quad (14)$$

where $\omega_{\text{dm}}(\theta)$ is the ACF predicted by the nonlinear model (Peacock & Dodds 1996) at the cosmic volume defined with $N(z)$ for each sample. Note that $\omega_{\text{dm}}(\theta)$ is defined in the same survey volume as our LAE sample, and that this bias value is equivalent to the bias given by the original definition, $b_g^2 = \xi(r)/\xi_{\text{dm}}(r)$, where $\xi_{\text{dm}}(r)$ is the spatial correlation function of dark matter. The top panels of Figures 11 and 12 plot $\omega_{\text{dm}}(\theta)$, and the bottom panels of Figures 11 and 12 show $b_g(\theta)$. We obtain an average bias, b_g , that is the value of $b_g(\theta)$ averaged over the same angular range as the one for the A_ω fitting (Section 4.1) with error weights. The upper limits of bias values, b_g^{\max} , are also calculated with A_ω^{\max} for the maximal contamination correction case of Equation (10). The estimates of b_g and b_g^{\max} are presented in Table 5. For our $z = 6.6$ LAEs, we obtain $b_g = 3\text{--}6$ and $b_g^{\max} = 5\text{--}9$.

¹⁴ Assuming that the clustering pattern is fixed in comoving coordinates in the redshift range of our sample, we take the functional form, $F(z) = (1+z)/(1+z_c)^{-(3+\epsilon)}$, where z_c is the central redshift of the sample and $\epsilon = -1.2$. The effect of the change in ϵ over $0 < \epsilon < -3$ on r_0 is, however, very small.

Table 5
Bias and Hosting Dark Halos

z	$\log(L_{\text{Lim}})$ (erg s $^{-1}$)	n_g (Mpc $^{-3}$)	b_g	b_g^{max}	M_h (M_\odot)	M_h^{min} (M_\odot)	M_h^{max} (M_\odot)
(1)	(2)	(3)	(4)	(5)	(6)	(7)	(8)
3.1	42.3	$8.9^{+1.9}_{-1.2} \times 10^{-4}$	1.5 ± 0.7	1.7 ± 0.8	$2.9^{+24.0}_{-2.9} \times 10^{10}$	$5.2^{+73.0}_{-5.2} \times 10^9$	$6.7^{+42.0}_{-6.7} \times 10^{10}$
3.1	42.1	$1.5^{+0.3}_{-0.2} \times 10^{-3}$	1.5 ± 0.3	1.8 ± 0.3	$3.6^{+3.6}_{-2.7} \times 10^{10}$	$6.8^{+15.0}_{-5.5} \times 10^9$	$8.2^{+11.0}_{-5.7} \times 10^{10}$
3.7	42.6	$2.8^{+0.6}_{-0.6} \times 10^{-4}$	2.8 ± 0.5	3.2 ± 0.5	$3.0^{+2.7}_{-1.7} \times 10^{11}$	$1.1^{+1.2}_{-0.7} \times 10^{11}$	$5.7^{+4.6}_{-3.0} \times 10^{11}$
5.7	42.6	$3.5^{+2.5}_{-1.7} \times 10^{-4}$	6.1 ± 0.7	8.2 ± 0.9	$6.1^{+2.8}_{-2.2} \times 10^{11}$	$3.5^{+1.9}_{-1.4} \times 10^{11}$	$1.7^{+0.7}_{-0.5} \times 10^{12}$
5.7	42.4	$6.8^{+3.8}_{-2.7} \times 10^{-4}$	5.5 ± 0.4	7.3 ± 0.5	$3.8^{+1.2}_{-0.9} \times 10^{11}$	$2.1^{+0.7}_{-0.5} \times 10^{11}$	$1.2^{+0.3}_{-0.3} \times 10^{12}$
6.6	42.6	$1.8^{+0.5}_{-0.4} \times 10^{-4}$	6.0 ± 2.2	8.9 ± 3.3	$2.4^{+0.9}_{-2.1} \times 10^{11}$	$1.3^{+3.9}_{-1.2} \times 10^{11}$	$1.1^{+2.1}_{-0.9} \times 10^{12}$
6.6	42.4	$4.1^{+0.9}_{-0.8} \times 10^{-4}$	3.6 ± 0.7	5.4 ± 1.0	$2.4^{+3.1}_{-1.6} \times 10^{10}$	$9.0^{+15.0}_{-6.5} \times 10^9$	$1.5^{+1.5}_{-0.9} \times 10^{11}$

Notes. (1) Redshift; (2) approximated limiting Ly α luminosity estimated from narrowband magnitudes; (3) number density of the observed LAEs that is derived with the best-fit Schechter function (Table 3); (4) best estimate of bias; (5) upper limit of bias with the maximal contamination correction; (6) average hosting dark halo mass inferred from the best estimate of bias; (7) minimum hosting dark halo mass; (8) upper limit of the average hosting dark halo mass corresponding to the upper limit of bias.

4.3. Hosting Dark Halo

We estimate dark halo masses of LAEs with bias values obtained in Section 4.2 in the framework of the Λ CDM model. Because, as discussed in Section 6.1.2, we find that clustering of $z = 6.6$ LAEs is negligibly affected by cosmic reionization, compared with the size of errors, the bias of $z = 6.6$ LAEs mostly depends on properties of hosting dark halos.

Generally, the average dark halo mass, M_h , and the mean galaxy bias, b_g , are given by

$$M_h = \frac{\int_{M_h^{\text{min}}}^{\infty} M f_{\text{duty}}^{\text{LAE}}(M) N_g(M) n(M) dM}{\int_{M_h^{\text{min}}}^{\infty} f_{\text{duty}}^{\text{LAE}}(M) N_g(M) n(M) dM} \quad \text{and} \quad (15)$$

$$b_g = \frac{\int_{M_h^{\text{min}}}^{\infty} b(M) f_{\text{duty}}^{\text{LAE}}(M) N_g(M) n(M) dM}{\int_{M_h^{\text{min}}}^{\infty} f_{\text{duty}}^{\text{LAE}}(M) N_g(M) n(M) dM}, \quad (16)$$

where $n(M)$ and $b(M)$ are the number density and bias of dark halos, respectively, with a mass of M , and $N_g(M)$ is a galaxy occupation function at the halo mass, M . $f_{\text{duty}}^{\text{LAE}}(M)$ is a fraction of dark halos hosting LAEs to those hosting any galaxies, which we refer to as the duty cycle of LAEs. M_h^{min} is the minimum dark halo mass that can host a galaxy. To obtain $n(M)$ and $b(M)$, we apply the model of Sheth & Tormen (1999; see also Mo & White 2002),

$$n(M) dM = A \left(1 + \frac{1}{v^{2q}} \right) \sqrt{\frac{2}{\pi}} \frac{\bar{\rho}_0}{M} \frac{dv'}{dM} \exp \left(-\frac{v'^2}{2} \right) dM, \quad (17)$$

where $v' = \sqrt{a}v$, $a = 0.707$, $A \simeq 0.322$, and $q = 0.3$. $\bar{\rho}_0$ is the current mean density of the universe. Here, v is a function of the growth factor, $D(z)$, and the rms of the density fluctuations on mass scale M , $\sigma(M)$, as defined by

$$v \equiv \frac{\delta_c}{D(z)\sigma(M)}, \quad (18)$$

where $\delta_c = 1.69$ represents the critical amplitude of the perturbation for collapse. We calculate the growth factor, $D(z)$, at redshift, z , following Carroll et al. (1992). Again, the power spectrum of the density fluctuations is calculated with the transfer function of Bardeen et al. (1986). The bias of dark halos is estimated by

$$b = 1 + \frac{1}{\delta_c} \left[v^2 + b v^{2(1-c)} - \frac{v^{2c}/\sqrt{a}}{v^{2c} + b(1-c)(1-c/2)} \right], \quad (19)$$

where $b = 0.5$, $c = 0.6$, and the other parameters (v' , δ_c , and a) are the same as those in Equations (17) and (18).

Note that our clustering measurements do not have accuracies high enough to determine the galaxy occupation function, which is often described with three free parameters (see, e.g., Hamana et al. 2004; Ouchi et al. 2005b; Lee et al. 2006; Kovač et al. 2007). Different choices of galaxy occupation functions change average halo masses only by a factor of a few, but not over an order of magnitude for LAEs (Hamana et al. 2004), unless extremely unphysical parameter sets are taken. Because we aim to accomplish an accuracy of an order of magnitude for halo properties inferred from clustering, we assume $N_g(M) = 1$, a one-to-one correspondence between galaxies and dark halos. We also assume that the duty cycle of LAEs is mass independent for simplicity (see more discussions about duty cycle in Section 4.4). In this case, M_h and b_g are independent of $f_{\text{duty}}^{\text{LAE}}$. We determine M_h^{min} with our observational estimates of LAE bias, b_g , via Equation (16), and calculate the average dark halo mass, M_h , from the M_h^{min} values with Equation (15). Table 5 presents M_h and M_h^{min} of our LAEs, together with the maximum of average halo mass, M_h^{max} , estimated with the maximally contamination-corrected bias of b^{max} .

Figure 13 plots our b_g values as a function of redshift. This figure also compares b_g of LAEs obtained in the previous studies. Note that in our study we assume $\sigma_8 = 0.8$ that is consistent with the latest WMAP results (Komatsu et al. 2009; Larson et al. 2010). Because all of the previous studies, except Guaita et al. (2010), assume $\sigma_8 = 0.9$, we multiply the bias values of these previous results by 1.1 to correct for the difference of σ_8 . This correction factor of 1.1, irrespective of redshift and selection function, is estimated from $\sqrt{\omega_{\text{dm}}(\sigma_8 = 0.9)/\omega_{\text{dm}}(\sigma_8 = 0.8)}$ with the model of Peacock & Dodds (1996), where $\omega_{\text{dm}}(\sigma_8 = 0.9)$ and $\omega_{\text{dm}}(\sigma_8 = 0.8)$ are ACFs predicted by the nonlinear model under $\sigma_8 = 0.9$ and 0.8, respectively. Figure 13 shows that our “all” and “bright” subsample measurements ($z = 3.1$ and 6.6) agree within 1σ errors at each redshift. This indicates that a clear luminosity segregation cannot be found beyond the size of our relatively large error bars for samples whose luminosity differs only by a factor of $\simeq 1.6$ (see Tables 4 and 5). The LAE samples of the previous studies and ours have similar Ly α luminosity limits ($L_{\text{Ly}\alpha} \simeq 2 \times 10^{42}$ erg s $^{-1}$) only with small differences by a factor of two, and the effect of luminosity dependence is probably smaller than the given relatively large error bars. Thus, we consider that the luminosity dependence between the LAE

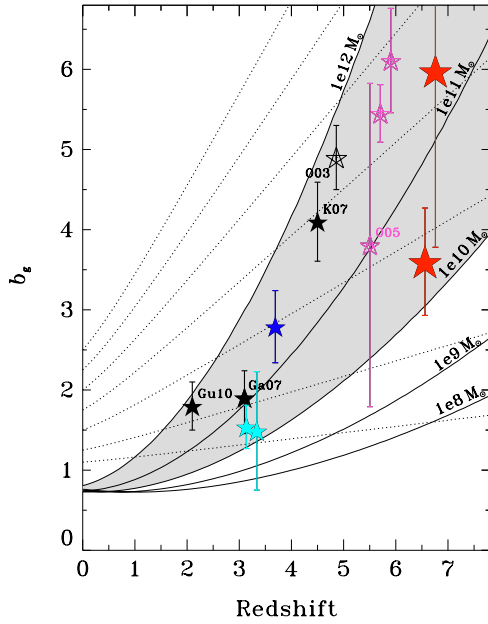


Figure 13. Bias of LAEs at $z = 2-7$. Red stars present our LAEs at $z = 6.6$ with the bright (top) and all (bottom) samples. Cyan, blue, and magenta stars plot the bias of SXDS LAEs at $z = 3.1, 3.7$, and 5.7 , respectively, estimated with the samples of Ouchi et al. (2008). Small offsets are given to these points in the direction of redshift to avoid overlapping symbols. Right and left cyan stars denote the bright and all samples at $z = 3.1$, respectively. For $z = 5.7$ LAEs, we show the bias of the bright LAE sample at right, all LAE sample in the middle, and the similar sample but estimated by Ouchi et al. (2005a, O05) with the count-in-cell technique in a large scale of 20 Mpc radius at left. Black stars represent estimates given by Guaita et al. (2010, Gu10; $z = 2.1$), Gawiser et al. (2007, Ga07; $z = 3.1$), Kovač et al. (2007, K07; $z = 4.5$), and Ouchi et al. (2003, O03; $z = 4.9$). Because the fields of the SXDS LAEs at $z = 5.7$ and Ouchi et al. (2003) have a strong large-scale clustering with protocluster candidates made of LAE overdensity, we use open star symbols to indicate the existence of these structures that may boost the bias measurements. Solid lines denote bias as a function of redshift for dark halos with a mass of $10^8, 10^9, 10^{10}, 10^{11}$, and $10^{12} M_{\odot}$ predicted by the Sheth & Tormen (1999) model in the case of one-to-one correspondence between galaxies and dark halos. The gray area denotes the dark halo mass range of $10^{10}-10^{12} M_{\odot}$ where LAEs at $z = 2-7$ falls. Dotted lines represent evolutionary tracks of bias under the galaxy-conserving model (Equation (24)). This plot assumes $\sigma_8 = 0.8$. We apply a correction to all of the previous estimates that assume $\sigma_8 = 0.9$, except for the one of Guaita et al. (2010).

samples is negligibly small in Figure 13 (see also the arguments for the relation between bias and number density described below). Figure 13 shows that our measurements at $z = 3.1$ are consistent with the measurement at the same redshift given by Gawiser et al. (2007). The bias of LAEs appears to increase from $z = 2-3$ to 6.6 . Because there are strong large-scale clusterings with protoclusters or protocluster candidates reported in the data of $z = 4.9$ in the SDF (Shimasaku et al. 2003) and $z = 5.7$ in the SXDS (Ouchi et al. 2005a), Figure 13 plots open star marks for the bias estimates at $z = 4.9$ in the SDF (Ouchi et al. 2003) and $z = 5.7$ in the SXDS (Ouchi et al. 2005a) to indicate that these bias estimates might be boosted by these obvious cosmic structures. Even if we omit the points of these open star marks in Figure 13, we confirm the trend of increasing bias toward high- z . To understand this increase, we plot Sheth & Tormen's (1999) model of a constant dark halo mass under the assumption of one-to-one correspondence between galaxies and dark halos. The dark halo masses of our $z = 6.6$ LAEs are about $10^{10}-10^{11} M_{\odot}$ in Figure 13, which are the same as those listed in Table 5. At $z = 2-7$, the bias values fall in the range of $\sim 10^{10}-10^{12} M_{\odot}$ for dark halo masses. Thus,

the average dark halo mass of LAEs is roughly $\sim 10^{11 \pm 1} M_{\odot}$ at $z = 2-7$. The dark halo masses of LAEs show no significant evolution at $z = 2-7$ beyond the mass-estimate scattering by an order of magnitude. It would indicate that all or some type of galaxies have an LAE stage in their evolution when their hosting dark halos reach a mass of $\sim 10^{11 \pm 1} M_{\odot}$ by mass assembly. Figure 14 plots bias and number density of LAEs, and compares those with Lyman break galaxies (LBGs) including *i*-dropouts. The solid lines present the relation of bias and number density for all dark halos, which correspond to the case of one-to-one correspondence between galaxies and dark halos. The dashed lines are the same as the solid lines but with their number densities multiplied by 10 and 1/10. The bias values of LAEs are generally smaller than those of LBGs at redshifts over 3–7. One exception is LAEs at $z = 5.7$ that have a bias value as large as those of $z \sim 6$ LBGs. However, bias measurements of these LAEs could be boosted by strong large-scale clustering with protoclusters as discussed above. On the other hand, LBGs have a roughly one-to-one correspondence between dark halos and galaxies within a scatter of an order of magnitude in number density. Comparing with LBGs, we find that LAEs have significantly less number density and/or bias. This weak bias at the small number density for LAEs indicates that LAEs reside in less massive dark halos on average, and that not all but some of the less massive dark halos can host LAEs. Because it is unlikely that some dark halos always have LAEs and the other dark halos with the same mass never host LAEs, dark halos become the ones hosting LAEs by duty cycle, stochastic processes made by star formation history and changes of interstellar medium (ISM) geometry and dynamics (Nagamine et al. 2008).

4.4. Duty Cycle

In Figure 14, the simplest estimate of duty cycle can be obtained from the ratio of the number density (ordinate of Figure 14) of all halos (solid line) to that of LAEs (star marks). However, due to a mild gradient of the solid curves, especially in the small bias range, even very small uncertainties of bias estimates of LAEs give very different duty cycle values. For this reason, the determination of duty cycle requires a precision measurement of the bias of LAEs. Nevertheless, in the following subsection, we try to constrain the duty cycle of LAEs with the given bias measurements and errors of the present study.

The duty cycle of LAEs can be constrained with a galaxy number density, n_g ,

$$n_g = \int_{M_h^{\min}}^{\infty} f_{\text{duty}}^{\text{LAE}}(M) N_g(M) n(M) dM. \quad (20)$$

Following the assumptions, $N_g(M) = 1$ and constant $f_{\text{duty}}^{\text{LAE}}$, made in Section 4.3, Equation (20) can be expressed as $f_{\text{duty}}^{\text{LAE}} = n_g / \int_{M_h^{\min}}^{\infty} n(M) dM$. We estimate $f_{\text{duty}}^{\text{LAE}}$ with M_h^{\min} values and the observed number densities of LAEs (Table 5) to be $f_{\text{duty}}^{\text{LAE}} = (0.008 \pm 0.03, 0.04 \pm 0.1, 1 \pm 1, 0.009 \pm 0.04)$ for our “all” LAEs at $z = (3.1, 3.7, 5.7, 6.6)$. Note that the errors of $f_{\text{duty}}^{\text{LAE}}$ are raised by the combination of M_h^{\min} and n_g estimates. The uncertainties of our $f_{\text{duty}}^{\text{LAE}}$ estimates are quite large as discussed above. Specifically, the $f_{\text{duty}}^{\text{LAE}}$ value of $z = 5.7$ provides no meaningful constraints, because its error of n_g is larger than the others due to a relatively large cosmic variance observed in our survey volume (see the caption of Figure 8). Because of these large uncertainties, we cannot constrain the

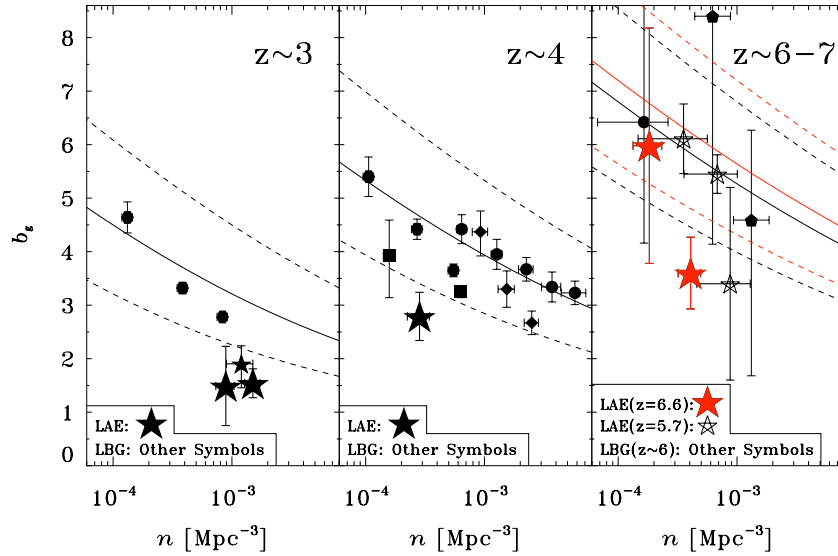


Figure 14. Bias as a function of number density at $z \sim 3$ (left), $z \sim 4$ (center), and $z \sim 6-7$ (right). Star marks represent LAEs, while the other symbols denote LBGs (including dropout galaxies). Specifically, the red stars indicate our LAEs at $z = 6.6$. The open star marks in the right panel are $z = 5.7$ SXDS LAEs whose bias values might be boosted by the large-scale clustering with protoclusters (Ouchi et al. 2005a). All of the star marks are our estimates from samples of this study and Ouchi et al.'s (2008) studies, except the small star mark in the left panel that is given by Gawiser et al. (2007). Because our estimates of LAEs overlap with that of Gawiser et al. (2007), we slightly shift their point in the number density direction for clarification. We plot the bias and number densities of LBGs with squares ($z \simeq 4$; Ouchi et al. 2004b), diamonds ($z \simeq 4$; Lee et al. 2006), pentagons ($z \simeq 6$; Overzier et al. 2006), hexagons ($z \simeq 3.3$ and 3.8 ; Hildebrandt et al. 2009), and circles ($z \simeq 4$, Ouchi et al. 2005b; $z \simeq 6$, Ouchi & SXDS Team 2005). Black solid lines indicate the relation of bias and number density for the case of one-to-one correspondence between galaxies and dark halos (Sheth & Tormen 1999) at $z = 3, 4$, and 6 , in the left, center, and right panels, respectively. Black dashed lines present the same relation but their number densities are multiplied by $1/10$ and 10 from bottom to top. Red solid and dashed lines in the right panel are the same, but for $z = 6.6$, the redshift of our LAE samples. This plot assumes $\sigma_8 = 0.8$. Because all of the previous bias estimates here are obtained with a cosmological parameter of $\sigma_8 = 0.9$, we apply the correction to the previous estimates for the different σ_8 values.

evolution of duty cycle. However, these $f_{\text{duty}}^{\text{LAE}}$ estimates indicate that $f_{\text{duty}}^{\text{LAE}}$ is a few 0.1 to a few percent, roughly $\sim 1\%$.

By definition, the duty cycle of LAEs, $f_{\text{duty}}^{\text{LAE}}$, is a fraction of galaxies that are LAEs. It can be expressed by the product $f_{\text{duty}}^{\text{LAE}} = f_{\text{duty}}^{\text{SF}} \times f_{\text{duty}}^{\text{Ly}\alpha}$, where $f_{\text{duty}}^{\text{SF}}$ is a duty cycle of star-forming activities in all dark halos, and $f_{\text{duty}}^{\text{Ly}\alpha}$ is the one for $\text{Ly}\alpha$ emitting galaxies among star-forming galaxies. Ouchi et al. (2004b) estimate $f_{\text{duty}}^{\text{SF}}$ of LBGs, UV-bright star-forming galaxies, to be $0.1-1^{15}$ from their clustering analyses, and a fainter galaxy has a smaller $f_{\text{duty}}^{\text{SF}}$ of 0.2 at $i \simeq 25.5$. Similarly, Lee et al. (2009) estimate $f_{\text{duty}}^{\text{SF}}$ to be $0.15-0.6$ for their LBGs with $z' < 27$ (Lee et al. 2006). Because our LAEs have a UV-continuum magnitude of ~ 27 mag on average (Ono et al. 2010a, 2010b), results of Ouchi et al. (2004b) and Lee et al. (2009) suggest that $f_{\text{duty}}^{\text{SF}}$ is $\lesssim 0.2$ for LBGs whose UV luminosity is comparable to our LAEs. On the other hand, Stark et al. (2010) obtain $f_{\text{duty}}^{\text{Ly}\alpha} \sim 0.5$ at ~ 27 mag, which is a fraction of $\text{Ly}\alpha$ emitting dropouts with $\text{EW}_0 > 50 \text{ \AA}$ to all LBGs at $z \simeq 3-6$. Combining these previous results, we find $f_{\text{duty}}^{\text{LAE}} = f_{\text{duty}}^{\text{SF}} \times f_{\text{duty}}^{\text{Ly}\alpha} \lesssim 0.1$, which is consistent with our estimates. Hayes et al. (2010) claim $f_{\text{duty}}^{\text{Ly}\alpha} = 0.05$ from the comparison of $\text{Ly}\alpha$ and $\text{H}\alpha$ emitting galaxies based on $\text{Ly}\alpha$ and $\text{H}\alpha$ LFs. If we naively assume that $f_{\text{duty}}^{\text{SF}}$ of $\text{H}\alpha$ emitting galaxies is the same as that of LBGs, i.e., $f_{\text{duty}}^{\text{SF}} \lesssim 0.2$, we obtain $f_{\text{duty}}^{\text{LAE}} \lesssim 0.01 (= 0.2 \times 0.05)$, which is roughly consistent with our result.

5. $\text{Ly}\alpha$ LINE PROFILE

We investigate $\text{Ly}\alpha$ line profiles of our $z = 6.6$ LAEs, exploiting our high-quality medium-high resolution spectra of Keck/DEIMOS. In this analysis, we add the 3 duplicate spectra to the 16 spectra (Section 2.3), and use a total of 19 DEIMOS spectra for $z = 6.6$ LAEs. In order to study the evolution of $\text{Ly}\alpha$ line profiles between $z = 5.7$ and 6.6 , we also perform analysis of 11 DEIMOS spectra of $z = 5.7$ LAEs. Ten out of the eleven DEIMOS spectra are taken in the SDF by Shimasaku et al. (2006) with exactly the same instrumental configuration as that of our $z = 6.6$ spectra, and the remaining one DEIMOS spectrum is obtained for the SXDS $z = 5.7$ LAE sample (Ouchi et al. 2008) as mask fillers of our DEIMOS observations on 2008 October 3 (Section 2.3). The top panels of Figure 15 present all of the DEIMOS spectra at $z = 6.6$ and 5.7 .

5.1. Composite Spectra and $\text{Ly}\alpha$ Velocity Widths

We make a composite spectra of our 19 spectra of $z = 6.6$ LAEs, and the 11 spectra of $z = 5.7$ LAEs to investigate the average $\text{Ly}\alpha$ line profiles. The line centers of the spectra are aligned to the wavelengths of 9190 \AA and 8157 \AA that are the average ones of the $z = 6.6$ and 5.7 samples, respectively. The line fluxes are normalized to average $\text{Ly}\alpha$ fluxes, since we calculate rejected-mean and median spectra for our stacking. In this process, we remove the lowest-quality five and two spectra from the $z = 6.6$ and 5.7 LAE spectra, respectively, so as to avoid the possible systematic bias given by uncertainties of line-center determination and/or flux normalization. We compute the rejected-mean spectra weighted with S/Ns of $\text{Ly}\alpha$ lines in the same manner as Ouchi et al. (2008). At each wavelength bin, the rejection is made for data points that fall beyond 68th

¹⁵ These numbers are given in the sixth column in Table 6 of Ouchi et al. (2004b).

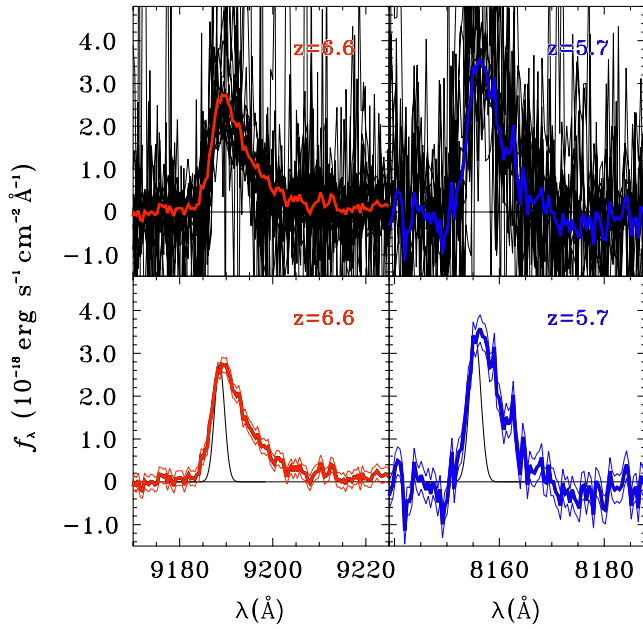


Figure 15. $\text{Ly}\alpha$ lines of LAEs. Top left: red line represents the composite spectrum of our $z = 6.6$ LAEs. Black lines denote our 19 DEIMOS spectra whose $\text{Ly}\alpha$ lines are aligned to the average redshift and scaled to the flux of the composite spectrum. Bottom left: the composite spectrum of our $z = 6.6$ LAEs is shown with a thick red line. 1σ error of the composite spectra is shown with thin red lines. The black curve presents the instrumental resolution of our DEIMOS spectra whose shape is approximated with a Gaussian profile. Top right: same as the top left panel, but for the $z = 5.7$ LAEs. The blue line is the composite spectrum of the $z = 5.7$ LAEs. Bottom right: same as the bottom left panel, but for the $z = 5.7$ LAEs. Blue lines are used for $z = 5.7$ LAEs.

percentile among all data points, which corresponds to the rejection of two (one) data points (point) above and below the 68 percentile for the LAEs at $z = 6.6$ (5.7). With this rejection algorithm, our composite spectra are secure against systematic residuals of sky subtraction. We compare these composite spectra with the ones computed by simple median statistics, and check whether these rejection procedures introduce a systematic bias. We find that the two composite spectra agree very well and that the rejected-mean composite spectra do not show any sign of bias in the overall shapes and velocity width of $\text{Ly}\alpha$ lines. Because improvements of S/N are generally better in the rejected-mean stacking than in the simple median stacking, we use the rejected-mean spectra for our composite spectra in the following discussion. Figure 15 plots our composite spectra of $z = 6.6$ and 5.7 LAEs. The quality of the spectrum of the $z = 5.7$ LAE is not as good as that of the $z = 6.6$ LAE. This is because (1) the total number of available $z = 5.7$ spectra (11) is small and (2) the average S/N of individual $z = 5.7$ spectra is relatively low due to their short (~ 2 hr) integration time (Shimasaku et al. 2006). The instrumental spectral resolution of the DEIMOS data is presented in the bottom panels of Figure 15, which illustrate that our composite spectra are well resolved beyond the instrumental resolution. Our composite spectra show a very clear asymmetric profile because of the high S/N.

To quantify the $\text{Ly}\alpha$ line profiles, we evaluate an FWHM velocity width, ΔV_{FWHM} . We fit a Gaussian profile to the individual spectra as well as the composite spectra, and obtain ΔV_{FWHM} . We correct for the instrumental broadening of line profile, and estimate intrinsic ΔV_{FWHM} by $\Delta V_{\text{FWHM}} = \sqrt{v_{\text{obs}}^2 - v_{\text{inst}}^2}$, where v_{obs} and v_{inst} are FWHM velocity widths for the measured $\text{Ly}\alpha$ lines and the instrumental resolution, respectively. We estimate the

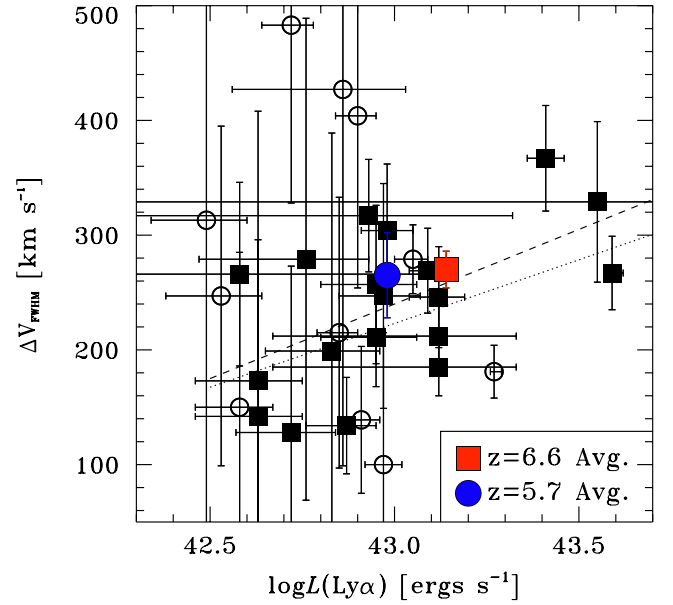


Figure 16. FWHM velocity width of our $z = 6.6$ LAEs, together with the $z = 5.7$ LAEs. The red square and blue circle denote velocity widths of the composite spectra. Black squares and open circles are velocity widths measured for individual LAEs at $z = 6.6$ and 5.7 , respectively. Dotted and dashed lines represent the best-fit linear functions to the individual LAEs at $z = 6.6$ with and without measurement errors in the fitting, respectively. These FWHM velocity widths are the ones given by the Gaussian profile fitting, which provides robust measurements for relatively poor-quality data of individual spectra.

errors of ΔV_{FWHM} including uncertainties raised by a choice of profile fitting range and Poisson statistics based on Monte Carlo simulations. Figure 16 and Table 2 present the ΔV_{FWHM} measured from the spectra and total $\text{Ly}\alpha$ luminosities estimated from the spectroscopic redshifts and the imaging data. Figure 16 indicates that the ΔV_{FWHM} values of $z = 6.6$ LAEs are distributed in the range of 100–400 km s^{-1} at $\log L(\text{Ly}\alpha) \simeq 42.6$ – 43.6 . The data points of $z = 5.7$ LAEs are similarly distributed, but with a larger scatter given by the larger errors than those of $z = 6.6$ LAEs. Our composite spectra have the FWHM velocity widths of 270 ± 16 and 265 ± 37 km s^{-1} at $z = 6.6$ and 5.7 , respectively. We also evaluate additional possible errors of ΔV_{FWHM} introduced by uncertainties of line-center alignment in the process of spectrum stacking. We find that the typical line-center determinations are as good as 0.32 Å and 0.90 Å for the $z = 6.6$ and 5.7 LAE spectra, respectively, and that the additional errors of line-center alignment contributing to ΔV_{FWHM} are negligibly small, only a 0.1%–1% level. We compare ΔV_{FWHM} of the $z = 6.6$ and 5.7 composite spectra in Figure 16. We find that ΔV_{FWHM} does not evolve from $z = 6.6$ to 5.7 beyond the 1σ level. Because the $\text{Ly}\alpha$ luminosities of our composite spectra are almost the same, $\log L(\text{Ly}\alpha) \simeq 43.0$, this comparison includes little bias of luminosity dependence.

Note that these ΔV_{FWHM} are estimated by Gaussian profile fitting. The real $\text{Ly}\alpha$ profile is not Gaussian, but asymmetric, as clearly found in our composite spectra. Although one cannot obtain ΔV_{FWHM} without fitting a profile, such as a Gaussian, for our relatively poor S/N data of individual spectra, ΔV_{FWHM} can be directly measured at least for the high-quality composite spectra. The direct measurements of FWHM velocity widths corrected for the instrumental broadening are 251 and 260 km s^{-1} for the $z = 6.6$ and 5.7 composite spectra, respectively. Table 6 summarizes the properties of our composite spectra and indicates that the FWHM velocity widths of the direct

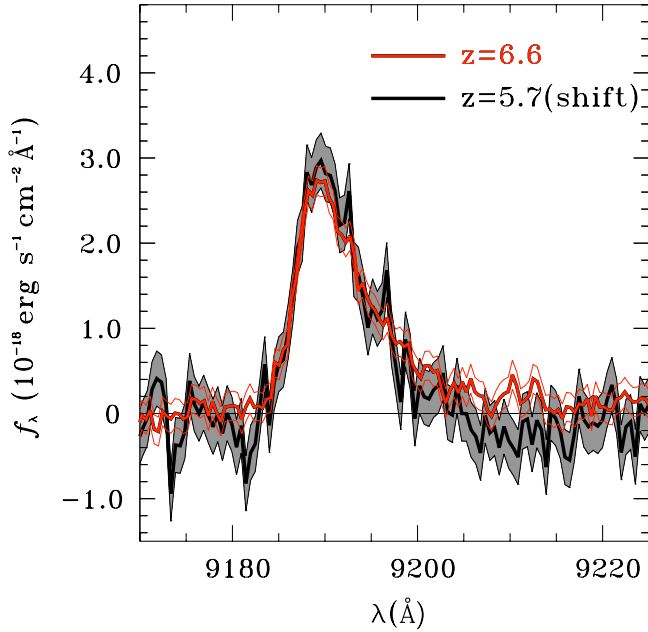


Figure 17. Evolution of LAE spectra. Red and black thick lines represent composite spectra of LAEs at $z = 6.6$ and 5.7 , respectively. For comparison of line shapes, the composite spectrum of the $z = 5.7$ LAEs is redshifted to $z = 6.6$, and scaled by an arbitrary factor. 1σ errors of the composite spectra are shown with thin red lines for $z = 6.6$ LAEs and a gray shade for $z = 5.7$ LAEs.

Table 6
Average Ly α Line Properties

$\langle z \rangle$	$\langle L_{\text{Ly}\alpha} \rangle$ ($10^{43} \text{ erg s}^{-1}$)	$\Delta V_{\text{FWHM}}(\text{direct})$ (km s^{-1})	$\Delta V_{\text{FWHM}}(\text{Gaussian})$ (km s^{-1})	Error(ΔV_{FWHM}) (km s^{-1})
(1)	(2)	(3)	(4)	(5)
6.56	1.39 ± 0.06	251	270	16
5.71	0.96 ± 0.03	260	265	37

Notes. (1) Average redshift; (2) average Ly α luminosity of our spectroscopic data; (3) average FWHM velocity width given by the direct measurement; (4) average FWHM velocity width determined by the Gaussian fitting; (5) error of FWHM velocity-width measurement.

measurements are comparable to those of the Gaussian fitting within the errors.

Figure 17 compares the composite spectra of $z = 6.6$ and 5.7 LAEs. The composite spectrum of $z = 6.6$ LAEs is similar to the one of $z = 5.7$ LAEs within the errors. We find no large evolution beyond the 1σ errors of our measurements. In fact, as shown in Table 6, the direct (Gaussian) FWHM velocity widths obtained above are 251 (270) $\pm 16 \text{ km s}^{-1}$ at $z = 6.6$ and 260 (265) $\pm 37 \text{ km s}^{-1}$ at $z = 5.7$, and there are no differences between the $z = 6.6$ and 5.7 composite spectra beyond the 1σ error of $\simeq 40 \text{ km s}^{-1}$, which is dominated by the error of $z = 5.7$ composite spectrum. Hu & Cowie (2006) also find no evolution of line profiles, although there are no quantitative comparisons in their study. Our composite spectrum of $z = 5.7$ has an S/N lower than that of $z = 6.6$ by a factor of two in the FWHM measurements, which do not allow us to investigate a slight profile change from $z = 6.6$ to 5.7 that may exist. If one compares the best-estimate spectra of our $z = 6.6$ and 5.7 LAEs (thick red and black lines, respectively, in Figure 17), the slope of the red wing is found to be slightly sharper for $z = 5.7$ LAEs than $z = 6.6$ LAEs. This would be a hint of flattening of Ly α line profiles from $z = 5.7$ to 6.6 . A future study with better spectroscopic data would address the issue of this slight evolutionary effect.

Interestingly, our composite spectra indicate that Ly α emission may not be simple smooth asymmetric lines, but contain a substructure. Comparing our composite spectra with the curves of instrumental spectral resolution in the bottom panels of Figure 15, we find knees in the blue tail of the composite LAE spectra at $\simeq 9185$ and 8152 \AA for $z = 6.6$ and 5.7 , respectively, both of which correspond to the same rest-frame wavelength about $\simeq 0.7 \text{ \AA}$ bluer than their line peaks. Since similar knees are not seen in our sky line spectra (e.g., the bottom right panel of Figure 3), these knees are not made by DEIMOS's instrumental line profile. Another possibility may be a residual of sky subtraction, but there are no clear reasons why the residual is mostly positively scattered in statistical sense to make the knees. The peaks of the knees are detected at the 3.5σ and 2.2σ levels for LAEs at $z = 6.6$ and 5.7 , respectively, at the same rest-frame wavelength, which is difficult to explain by the random errors (see 1σ errors associated with the composite spectra in Figure 15). Thus, the knees in the blue wings of $z = 6.6$ and 5.7 spectra are probably real.

5.2. Ly α Velocity–Luminosity Relation

Figure 16 presents a weak, but a positive correlation between ΔV_{FWHM} and $\log L(\text{Ly}\alpha)$ in our $z = 6.6$ LAEs. A linear function fit to the $z = 6.6$ $\Delta V_{\text{FWHM}} - \log L(\text{Ly}\alpha)$ data indicates that the positive correlation is found at the 2.5σ level. This trend is opposite to the one found by Kashikawa et al. (2006). Kashikawa et al. (2006) study LAEs with $\log L(\text{Ly}\alpha) \simeq 42.3 - 43.0$ that are fainter than ours by a factor of 2–4 on average. The distribution of data points of Kashikawa et al. (2006) is similar to ours in the luminosity range where both studies have measurements. Figure 11 of Kashikawa et al. (2006) presents two faint LAEs that have large FWHMs, which apparently make the anti-correlation. If these two faint LAEs are largely up-scattered by statistical errors or sample variance, the anti-correlation is not clearly found. Moreover, Kashikawa et al. (2006) consider no velocity-width measurement errors in their linear-function fitting, while the uncertainties of velocity-width measurements increase toward faint luminosity. Thus, the previous conclusion of the anti-correlation is probably not strong. On the other hand, in Figure 16, our positive correlation is apparent when our data of three bright LAEs in $\log L(\text{Ly}\alpha) \simeq 43.3 - 43.6$ are included. When these three data points are not used for our fitting, neither positive nor negative correlation is identified beyond the 1σ level. If these three bright LAEs were not typical ones due to a sample variance, the clear positive correlation would not be found. Although there is a possibility that these three LAEs are not typical due to sample variance, these bright LAEs have small errors that are difficult to produce largely up-scattered measurements. We conclude that there is no anti-correlation between Ly α luminosity and line width at $z = 6.6$, and that, if our spectroscopic sample is not a biased one, Ly α velocity width positively correlates with Ly α luminosity at $z = 6.6$ in the luminosity range of $\log L(\text{Ly}\alpha) \simeq 42.6 - 43.6$.

6. DISCUSSION

6.1. Constraints on the Cosmic Reionization History

In this section, we discuss implications for cosmic reionization based on our LF, clustering, and Ly α line profile results with the aid of theoretical models. Because some conclusions of theoretical models would depend on their assumptions and methods such as analytical, semi-analytical, and numerical techniques

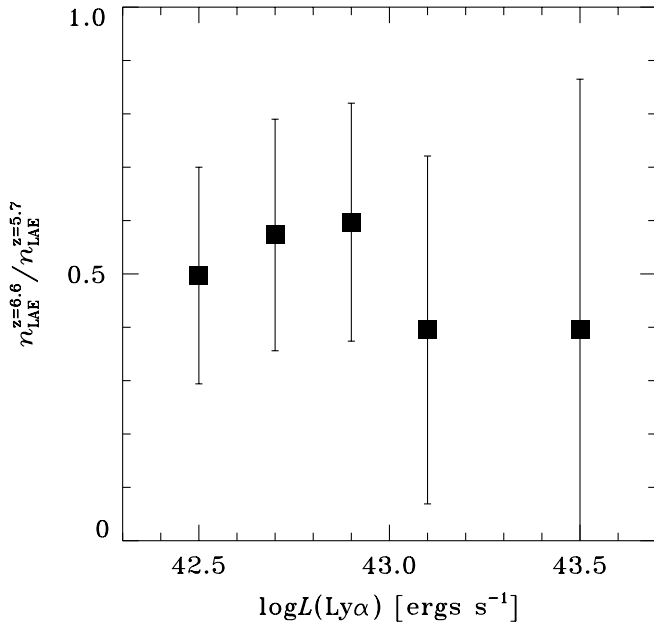


Figure 18. Ratio of number densities of $z = 6.6$ LAEs to $z = 5.7$ LAEs as a function of $\text{Ly}\alpha$ luminosity. Squares plot observational results from LAEs at $z = 6.6$ (this study) and $z = 5.7$ (Ouchi et al. 2008). The data binning is the same as that in Figures 6 and 7.

including radiative transfer, we compare our observational measurements with as many various theoretical models available to date as possible. In this way, we aim to obtain implications for cosmic reionization with less model dependences.

6.1.1. Evolution of $\text{Ly}\alpha$ LF and Luminosity Density

In Section 3.4, we have found that $\text{Ly}\alpha$ LF decreases from $z = 5.7$ to 6.6 at the $>90\%$ confidence level, and that the decrease is 30% in luminosity for the case of pure luminosity evolution. Because $\text{Ly}\alpha$ LF evolution is made not only by cosmic reionization but also by galaxy evolution, we should interpret the decrease of $\text{Ly}\alpha$ LF carefully. In fact, UV-continuum LF of dropout galaxies also decreases from $z = 6$ to 7–8 in observational data (e.g., Ouchi et al. 2009b; Bouwens et al. 2010a; Castellano et al. 2010). Some fraction of the $\text{Ly}\alpha$ LF decrease may be explained by this galaxy evolution effect. Figure 18 presents a number density ratio of $z = 6.6$ to 5.7 LAEs as a function of $\text{Ly}\alpha$ luminosity. We find no significant dependence on luminosity for the ratio within errors, i.e., by a factor of $\simeq 2$ at the luminosity range of $\log L = 42.5\text{--}43.5$. However, it appears that the ratio is relatively smaller at the bright luminosity ($\log L = 43.0\text{--}43.5$) than the faint luminosity ($\log L = 42.5\text{--}43.0$). Note that Figure 18 misses a measurement at the bin of $\log L = 43.3$, because no LAEs are found at $z = 6.6$ in this bin. If the trend of relatively small number density of $z = 6.6$ LAEs at the bright luminosity is true, galaxy evolution may be more dominant on the LF evolution between $z = 5.7$ and 6.6 than the cosmic reionization effect. Since brighter LAEs are likely hosted by more massive dark halos whose formation epochs are near these redshifts (see halo mass functions; e.g., Sheth & Tormen 1999), the evolution of number density of bright LAEs would be more affected by galaxy evolution. On the other hand, simple models of LAEs suggest that brighter LAEs have a less reduction of $\text{Ly}\alpha$ flux due to large ionized bubbles surrounding bright LAEs (Haimes 2002), which would imply that the evolution of bright LAEs is milder than that of faint LAEs in the reionization-effect dominant case.

We need to quantify how much decrease of $\text{Ly}\alpha$ LF is contributed from cosmic reionization or galaxy evolution. If we have an assumption of no galaxy formation effects in $\text{Ly}\alpha$ LF evolution, which is made in previous studies (e.g., Malhotra & Rhoads 2004; Kashikawa et al. 2006), a ratio of IGM's $\text{Ly}\alpha$ transmission at $z = 6.6$ to the one at $z = 5.7$ is 0.7. However, it is not clear whether the no galaxy evolution assumption is correct. The UV LF evolution of LAEs between $z = 5.7$ and 6.6 could resolve the degeneracy of $\text{Ly}\alpha$ LF evolution between cosmic reionization and galaxy formation. Although Kashikawa et al. (2006) claim that there is no evolution of UV LF of LAEs between $z = 5.7$ and 6.6 based on their $\text{Ly}\alpha$ -subtracted z' photometry, we have found that UV LF of LAEs cannot be derived from $\text{Ly}\alpha$ -subtracted z' photometry with an accuracy better than a factor of 2–3, due to large uncertainties. In fact, UV magnitudes estimated with the $\text{Ly}\alpha$ -subtracted z' photometry have large errors, $>0.4\text{--}0.7$, as shown in Table 2. These large errors are raised, because fluxes in the z' band are dominated by the strong $\text{Ly}\alpha$ line, but not by the faint UV continuum. Only with optical z' -band photometry can UV LFs of LAEs be reliably derived up to $z \lesssim 6$ LAEs whose $\text{Ly}\alpha$ lines do not enter the z' band (e.g., Hu et al. 2004; Shimasaku et al. 2006; Ouchi et al. 2008), and near-infrared photometry is required to derive reliable UV LF of LAEs at $z = 6.6$. It should be noted that, by the same reason, EW_0 values of UV-continuum faint LAEs ($\text{EW}_0 \gtrsim 100 \text{ \AA}$) are very poorly constrained (Table 2), and that a number- EW_0 distribution of our $z = 6.6$ LAEs is not obtained reliably. Since we cannot use an uncertain UV LF of LAEs at $z = 6.6$, we investigate effects of galaxy formation with the other methods.

We calculate luminosity densities, ρ , of $\text{Ly}\alpha$ lines from LAEs and UV continua from dropout galaxies, and present ratios of $\rho_z/\rho_{z\sim 6}$ in the top panel of Figure 19, where ρ_z and $\rho_{z\sim 6}$ are luminosity densities of redshifts z and 6, respectively. For these calculations, we use $\text{Ly}\alpha$ LFs at $z = 6.6$ (this study) and 3.1 (Ouchi et al. 2008) as well as UV LFs at $z = 2\text{--}7$ (Bouwens et al. 2007; Reddy & Steidel 2009; Oesch et al. 2010). We estimate two sets of ρ from integrals down to the observed luminosity ($\log L_{\text{Ly}\alpha} = 42.4$ for $\text{Ly}\alpha$ or $M_{\text{UV}} = -18$ for UV) and down to zero luminosity; the latter is probably near a total ρ . We confirm that the ratios of these different estimates agree within the error bars in Figure 19. We thus refer to the latter estimate for our fiducial results including no systematic bias from observations. The top panel of Figure 19 indicates that $\text{Ly}\alpha$ $\rho_z/\rho_{z\sim 6}$ stays constant within the errors between $z = 3.1$ and 5.7, but there is a drop from $z = 5.7$ to 6.6 beyond the error bar. This drop of $\text{Ly}\alpha$ $\rho_z/\rho_{z\sim 6}$ is originated from the decrease of $\text{Ly}\alpha$ LF in this redshift range. On the other hand, a ratio of UV ρ monotonically decreases from $z \sim 3$ to 7. The decrease of UV $\rho_z/\rho_{z\sim 6}$ from $z \sim 6$ to 7 suggests that the cosmic star formation rate density (SFRD) of galaxies decline at this redshift range, and this cosmic SFRD decline would contribute to the decrease of $\text{Ly}\alpha$ $\rho_z/\rho_{z\sim 6}$ from $z = 5.7$ to 6.6.

We evaluate the effect of cosmic SFRD decline on the basis of evolution of UV luminosity density. We assume that $\text{Ly}\alpha$ luminosity density, $\rho^{\text{Ly}\alpha}$, is proportional to UV luminosity density, ρ^{UV} ,

$$\rho^{\text{Ly}\alpha} = \kappa T_{\text{IGM}}^{\text{Ly}\alpha} f_{\text{esc}}^{\text{Ly}\alpha} \rho^{\text{UV}}, \quad (21)$$

where $T_{\text{IGM}}^{\text{Ly}\alpha}$ is a transmission fraction of $\text{Ly}\alpha$ through the IGM and $f_{\text{esc}}^{\text{Ly}\alpha}$ is an $\text{Ly}\alpha$ escape fraction within a galaxy through the ISM. $f_{\text{esc}}^{\text{Ly}\alpha}$ depends on gas infall+outflow (Santos et al. 2004; Dijkstra et al. 2007a; Dijkstra & Wyithe 2010), distribution

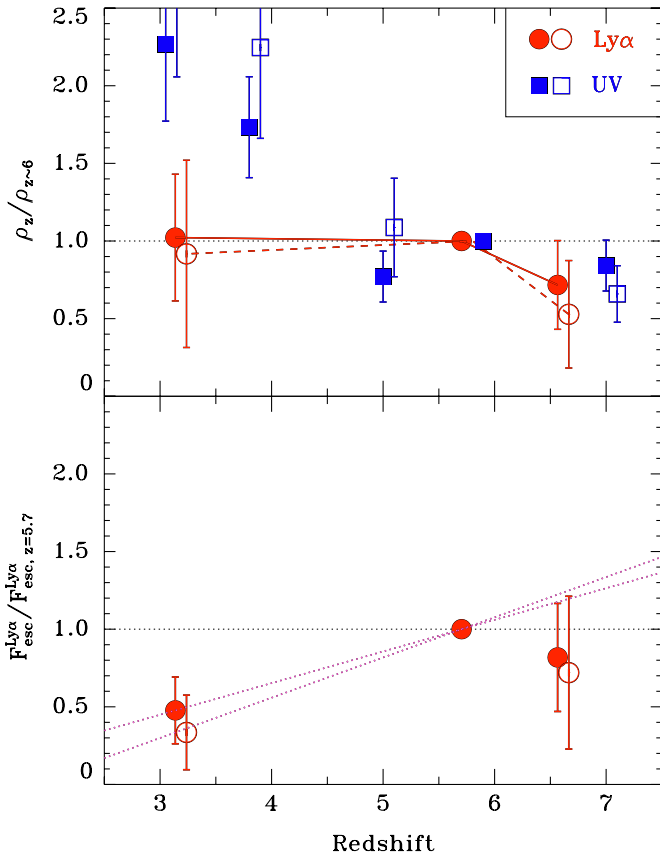


Figure 19. Top panel shows ratios of a luminosity density at each redshift to the one at $z \sim 6$. Red circles and blue squares represent the ratios for Ly α and UV, respectively. The luminosity density of $z \sim 6$ is defined with the one at $z = 5.7$ for Ly α and $z \sim 6$ for UV. The open symbols are the ratios of luminosity densities integrated down to the observed luminosity ($\log L_{\text{Ly}\alpha} = 42.4$ for Ly α or $M_{\text{UV}} = -18$ for UV), while the filled symbols are the ratios of estimated total luminosity densities integrated to zero luminosity. Open symbols are shifted by +0.1 along redshift for clarity. Red solid and dashed lines simply connect the Ly α points of red filled and open circles, respectively. Note that the ratios at $z \sim 6$ have no error bars because this is a definition of the ratios. Instead, the errors of luminosity density measurements at $z \sim 6$ are included in the ratios at the other redshifts ($z \neq 6$). Bottom panel plots ratios of total Ly α escape fraction, $F_{\text{esc}}^{\text{Ly}\alpha}$, as a function of redshift. The ratios are $F_{\text{esc}}^{\text{Ly}\alpha}$ at each redshift divided by $F_{\text{esc}}^{\text{Ly}\alpha}$ at $z = 5.7$. Again, the open circles are those calculated with the luminosity densities integrated down to the observed luminosity, while the filled circles are estimated from the total luminosity densities integrated down to zero luminosity. Magenta dotted lines present linear fits of $F_{\text{esc}}^{\text{Ly}\alpha} / F_{\text{esc}, z=5.7}^{\text{Ly}\alpha}$ and redshift to filled and open circles in the low-redshift range of $z = 3.1-5.7$.

of galactic hydrogen (Zheng et al. 2010a, 2010b), and dust obscuration (Dayal et al. 2010). κ is a factor converting from UV to Ly α luminosities, which depend on stellar population, i.e., initial mass function (IMF), age, and metallicity. Assuming that the stellar population of LAEs is the same at $z = 5.7$ and a given redshift, z , we can obtain a ratio of $T_{\text{IGM}}^{\text{Ly}\alpha} f_{\text{esc}}^{\text{Ly}\alpha}$ at $z = 5.7$ to a redshift, z , with only Ly α and UV luminosity densities:

$$\frac{T_{\text{IGM}, z}^{\text{Ly}\alpha} f_{\text{esc}, z}^{\text{Ly}\alpha}}{T_{\text{IGM}, z=5.7}^{\text{Ly}\alpha} f_{\text{esc}, z=5.7}^{\text{Ly}\alpha}} = \frac{\rho_z^{\text{Ly}\alpha} / \rho_{z=5.7}^{\text{Ly}\alpha}}{\rho_z^{\text{UV}} / \rho_{z=5.7}^{\text{UV}}}, \quad (22)$$

where the indices, z and $z = 5.7$, show redshifts. Because the product, $T_{\text{IGM}}^{\text{Ly}\alpha} f_{\text{esc}}^{\text{Ly}\alpha}$, is a total of Ly α escape fractions, i.e., a fraction of Ly α photons escaping from the IGM and ISM, we refer to this product as a total Ly α escape fraction. We write

$$F_{\text{esc}}^{\text{Ly}\alpha} \equiv T_{\text{IGM}}^{\text{Ly}\alpha} f_{\text{esc}}^{\text{Ly}\alpha} \quad (23)$$

for simplicity. With this definition, the left-hand side of Equation (22) is rewritten as $F_{\text{esc}, z}^{\text{Ly}\alpha} / F_{\text{esc}, z=5.7}^{\text{Ly}\alpha}$ showing redshifts with the indices. Equation (22) means that $F_{\text{esc}, z}^{\text{Ly}\alpha} / F_{\text{esc}, z=5.7}^{\text{Ly}\alpha}$ is determined by the ratio of Ly α luminosity densities divided by the ratio of UV luminosity densities. Since the ratio of UV luminosity densities, $\rho_z^{\text{UV}} / \rho_{z=5.7}^{\text{UV}}$, plays a role of a correction factor of cosmic SFRD evolution, we refer to this as a cosmic SFRD correction factor. The bottom panel of Figure 19 plots $F_{\text{esc}, z}^{\text{Ly}\alpha} / F_{\text{esc}, z=5.7}^{\text{Ly}\alpha}$ as a function of redshift. We find that the total Ly α escape fraction might show a possible decrease by $\sim 20\%$ from $z = 5.7$ to 6.6, albeit with a large error. Thus, the evolution of $F_{\text{esc}, z}^{\text{Ly}\alpha}$ is small and less significant than that of the ratio of Ly α ρ_z shown in the top panel of Figure 19. On the other hand, $F_{\text{esc}, z}^{\text{Ly}\alpha}$ increases from $z = 3.1$ to 5.7 in the bottom panel of Figure 19. This is probably because a fraction of Ly α escaping from the ISM (i.e., $f_{\text{esc}}^{\text{Ly}\alpha}$) increases from low- z toward $z = 5.7$. If one naively extrapolates the linear fit of the relation at $z = 3.1-5.7$ between $F_{\text{esc}, z}^{\text{Ly}\alpha} / F_{\text{esc}, z=5.7}^{\text{Ly}\alpha}$ and redshift toward high- z in the bottom panel of Figure 19, $F_{\text{esc}}^{\text{Ly}\alpha}$ at $z = 6.6$ is smaller than that of the extrapolation (magenta dotted lines in Figure 19) just beyond the 1σ error. However, the evolution of IGM ($T_{\text{IGM}}^{\text{Ly}\alpha}$) and galaxies ($f_{\text{esc}}^{\text{Ly}\alpha}$) cannot be clearly distinguished.

Thus, we evaluate $f_{\text{esc}}^{\text{Ly}\alpha}$, and estimate the evolution of Ly α transmission of IGM from $z = 5.7$ to 6.6 with a quantity of $T_{\text{IGM}, z=6.6}^{\text{Ly}\alpha} / T_{\text{IGM}, z=5.7}^{\text{Ly}\alpha}$. Because the estimates based on $\rho_z^{\text{Ly}\alpha} / \rho_{z=5.7}^{\text{Ly}\alpha}$ shown above would provide additional uncertainties raised by the integration ranges for Ly α luminosity densities, we perform calculations with ratios of Ly α luminosity by replacing $\rho_z^{\text{Ly}\alpha} / \rho_{z=5.7}^{\text{Ly}\alpha}$ with the ratio of Ly α luminosity, $L_z^{\text{Ly}\alpha} / L_{z=5.7}^{\text{Ly}\alpha}$, in Equation (22) at given data points of observed number density, although this improvement of calculations provides only negligible changes in our results. Note that the quantity of $T_{\text{IGM}, z=6.6}^{\text{Ly}\alpha} / T_{\text{IGM}, z=5.7}^{\text{Ly}\alpha}$ can be written as $T_{\text{IGM}, z=6.6}^{\text{Ly}\alpha} / T_{\text{IGM}, z=5.7}^{\text{Ly}\alpha} = (F_{\text{esc}, z=6.6}^{\text{Ly}\alpha} / F_{\text{esc}, z=5.7}^{\text{Ly}\alpha}) (f_{\text{esc}, z=5.7}^{\text{Ly}\alpha} / f_{\text{esc}, z=6.6}^{\text{Ly}\alpha})$ by the definition (Equation (23)). Here, the unknown physical quantity is the evolution of the ratio of Ly α escaping fractions, i.e., $(f_{\text{esc}, z=5.7}^{\text{Ly}\alpha} / f_{\text{esc}, z=6.6}^{\text{Ly}\alpha})$. We consider the two cases of $f_{\text{esc}}^{\text{Ly}\alpha}$ evolution under an assumption of no luminosity dependence of $f_{\text{esc}}^{\text{Ly}\alpha}$ for simplicity. In the first case $f_{\text{esc}}^{\text{Ly}\alpha}$ does not evolve between $z = 5.7$ and 6.6, which gives $(f_{\text{esc}, z=5.7}^{\text{Ly}\alpha} / f_{\text{esc}, z=6.6}^{\text{Ly}\alpha}) = 1$. We find that the ratio is $T_{\text{IGM}, z=6.6}^{\text{Ly}\alpha} / T_{\text{IGM}, z=5.7}^{\text{Ly}\alpha} = 0.80 \pm 0.18$, and that IGM transmission at $z = 6.6$ decreases at the 1σ level. For the second case, we estimate it with a $f_{\text{esc}}^{\text{Ly}\alpha}$ evolution between $z = 5.7$ and 6.6. We assume that the redshift evolution of $f_{\text{esc}}^{\text{Ly}\alpha}$ between $z = 5.7$ and 6.6 is the same as that of linear increase per redshift found in the low redshift regime of $z = 3.1-5.7$. To quantify the evolution of $f_{\text{esc}}^{\text{Ly}\alpha}$ at the low- z ($z = 3.1-5.7$), we can rewrite Equation (23): $f_{\text{esc}, z=3.1}^{\text{Ly}\alpha} / f_{\text{esc}, z=5.7}^{\text{Ly}\alpha} = (F_{\text{esc}, z=3.1}^{\text{Ly}\alpha} / F_{\text{esc}, z=5.7}^{\text{Ly}\alpha}) (T_{\text{IGM}, z=5.7}^{\text{Ly}\alpha} / T_{\text{IGM}, z=3.1}^{\text{Ly}\alpha})$. Figure 19 shows that $(F_{\text{esc}, z=3.1}^{\text{Ly}\alpha} / F_{\text{esc}, z=5.7}^{\text{Ly}\alpha}) = 0.48$. We estimate the ratio of $(T_{\text{IGM}, z=5.7}^{\text{Ly}\alpha} / T_{\text{IGM}, z=3.1}^{\text{Ly}\alpha})$ with the average GP optical depths. Assuming that IGM absorbs a blue half of symmetric Ly α emission line, we obtain $(T_{\text{IGM}, z=5.7}^{\text{Ly}\alpha} / T_{\text{IGM}, z=3.1}^{\text{Ly}\alpha}) = (0.53/0.85)$ based on the estimates of Fan et al. (2006).¹⁶ Note that this number is a

¹⁶ The estimate of $T_{\text{IGM}}^{\text{Ly}\alpha}$ differs only by 3%–5% from those with Madau (1995) and Meiksin (2006; see Ouchi et al. 2008).

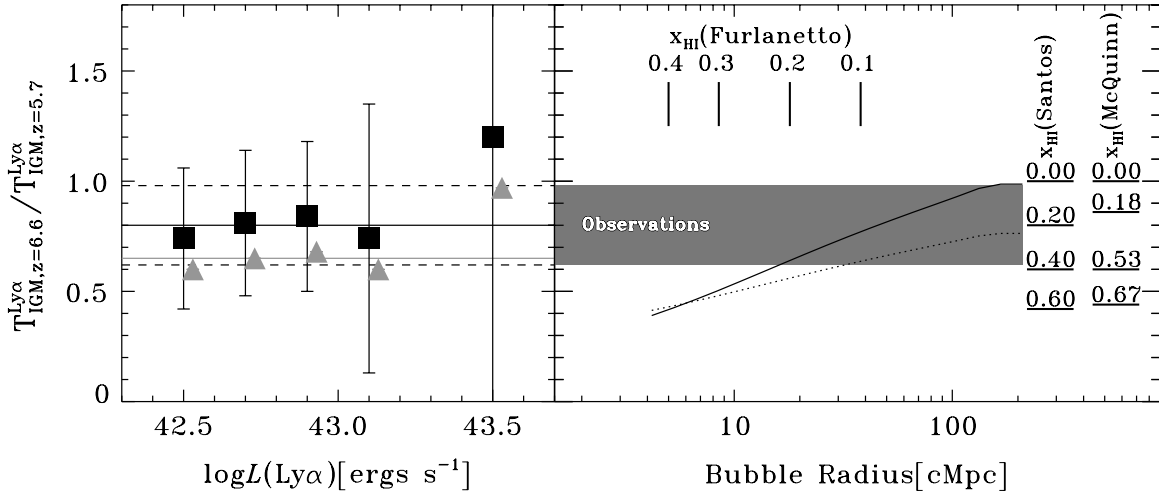


Figure 20. Ly α transmission through IGM at $z = 6.6$ that is normalized by the one at $z = 5.7$. Left panel shows our observational estimates of $T_{\text{IGM},z=6.6}^{\text{Ly}\alpha} / T_{\text{IGM},z=5.7}^{\text{Ly}\alpha}$. Black squares plot $T_{\text{IGM},z=6.6}^{\text{Ly}\alpha} / T_{\text{IGM},z=5.7}^{\text{Ly}\alpha}$ in the case of no evolution of Ly α escape fraction ($f_{\text{esc}}^{\text{Ly}\alpha}$). Black solid and dashed lines are the best estimate and $\pm 1\sigma$ errors of $T_{\text{IGM},z=6.6}^{\text{Ly}\alpha} / T_{\text{IGM},z=5.7}^{\text{Ly}\alpha}$, respectively, for the no $f_{\text{esc}}^{\text{Ly}\alpha}$ evolution case. Similarly, gray triangles and line represent the lower limit in the case of the $f_{\text{esc}}^{\text{Ly}\alpha}$ evolution. Right panel compares these estimates with model predictions. Gray region shows our observational constraints ($\pm 1\sigma$) on $T_{\text{IGM},z=6.6}^{\text{Ly}\alpha} / T_{\text{IGM},z=5.7}^{\text{Ly}\alpha}$. Solid and dotted lines represent the model predictions of Dijkstra et al. (2007b) as a function of ionized bubble radius in comoving Mpc for the cases with and without ionizing background boosts of undetected surrounding sources, respectively. Ticks at the top present the relation between the typical bubble radius and the neutral-hydrogen fraction of IGM for $x_{\text{H I}} \simeq 0.4, 0.3, 0.2$, and 0.1 , which are predicted by the analytic model of Furlanetto et al. (2006). Two sets of ticks in the right-hand side of the panel denote the predicted relations between $x_{\text{H I}}$ and $T_{\text{IGM},z=6.6}^{\text{Ly}\alpha} / T_{\text{IGM},z=5.7}^{\text{Ly}\alpha}$ in the models of Santos et al. (2004) and McQuinn et al. (2007).

lower limit, because Ly α lines are redshifted from the systemic velocity by a few hundred km s $^{-1}$ and less absorbed by IGM (Pettini et al. 2001; McLinden et al. 2010; Steidel et al. 2010). The real number of ($T_{\text{IGM},z=5.7}^{\text{Ly}\alpha} / T_{\text{IGM},z=3.1}^{\text{Ly}\alpha}$) is $> (0.53/0.85)$, closer to unity. Hence the value of $f_{\text{esc},z=3.1}^{\text{Ly}\alpha} / f_{\text{esc},z=5.7}^{\text{Ly}\alpha}$ is > 0.30 ($= 0.48 \times 0.53/0.85$). Extrapolating the redshift evolution of $f_{\text{esc}}^{\text{Ly}\alpha}$ to 6.6, we obtain the ratio of Ly α escape fraction at $z = 5.7$ to 6.6, ($f_{\text{esc},z=5.7}^{\text{Ly}\alpha} / f_{\text{esc},z=6.6}^{\text{Ly}\alpha}$) > 0.81 . Thus, $T_{\text{IGM},z=6.6}^{\text{Ly}\alpha} / T_{\text{IGM},z=5.7}^{\text{Ly}\alpha} > 0.65$ in this second case with the redshift evolution of $f_{\text{esc}}^{\text{Ly}\alpha}$.

The left panel of Figure 20 presents $T_{\text{IGM},z=6.6}^{\text{Ly}\alpha} / T_{\text{IGM},z=5.7}^{\text{Ly}\alpha}$ for the first and second cases with black and gray lines, respectively. Figure 20 also plots the ratio as a function of Ly α luminosity for each observational data point with squares and triangles. Note that the second case only gives the lower limit, and that the gray triangles in the left panel of Figure 20 represent the lower limits. Figure 20 shows that these lower limits are consistent with the results of the first case within the -1σ error, and, thus, the second-case result is included in the first-case result of $T_{\text{IGM},z=6.6}^{\text{Ly}\alpha} / T_{\text{IGM},z=5.7}^{\text{Ly}\alpha} = 0.80 \pm 0.18$. It indicates that the IGM transmission at $z = 6.6$, $T_{\text{IGM},z=6.6}^{\text{Ly}\alpha}$, is smaller than the one at $z = 5.7$ by 20% but just beyond the 1σ error. We conclude that there would exist a small decrease of IGM transmission at the 1σ level, probably contributed by cosmic reionization, and that the ratio of $T_{\text{IGM},z=6.6}^{\text{Ly}\alpha} / T_{\text{IGM},z=5.7}^{\text{Ly}\alpha}$ is $\simeq 0.8$ and no smaller than 0.6.

We obtain another independent constraint on $T_{\text{IGM},z=6.6}^{\text{Ly}\alpha} / T_{\text{IGM},z=5.7}^{\text{Ly}\alpha}$ by comparison with physical models including galaxy evolution and cosmic reionization effects. The left panel of Figure 21 compares Ly α LFs predicted with the semi-analytic models of Kobayashi et al. (2010). Because the model of Kobayashi et al. (2010) reproduces observed Ly α LFs between $z = 3.1$ and 5.7, the galaxy evolution component of this model

at $z \simeq 3-6$ is probably reliable. We plot their Ly α LFs at $z = 6.56$ in three cases of $T_{\text{IGM},z=6.6}^{\text{Ly}\alpha} / T_{\text{IGM},z=5.7}^{\text{Ly}\alpha} = 1.0, 0.8$, and 0.6.¹⁷ Although the models under-predict number densities of LAEs at the faint end ($\log L \lesssim 42.8$) for all the cases, shapes of the predicted LFs agree at the bright luminosity ($\log L \gtrsim 42.8$). Because their faint-end LF may be strongly affected by complicated star formation and supernova feedback processes depending on model assumptions (Kobayashi et al. 2010; see Nagashima & Yoshii 2004 for their models of galaxy formation components), we compare only their bright-end LFs. The left panel of Figure 21 shows that their bright-end LF of the $T_{\text{IGM},z=6.6}^{\text{Ly}\alpha} / T_{\text{IGM},z=5.7}^{\text{Ly}\alpha} = 0.8$ model reproduces our observational results. This constraint on $T_{\text{IGM},z=6.6}^{\text{Ly}\alpha} / T_{\text{IGM},z=5.7}^{\text{Ly}\alpha}$ is consistent with our estimate of $T_{\text{IGM},z=6.6}^{\text{Ly}\alpha} / T_{\text{IGM},z=5.7}^{\text{Ly}\alpha} = 0.80 \pm 0.18$. The right panel of Figure 21 presents Ly α LF predicted with the radiative transfer model of Iliev et al. (2008). Because their luminosity is arbitrary, we have applied a shift of $\Delta \log L = +31.6$ to their model that is roughly matched to our observational data points. The LF shape of the model agrees with that of our observations in the luminosity range of $\log L \simeq 42.5-43.5$, although there is a hint of a steeper LF slope in the model than in our observational measurements.

Next, we place a constraint on a neutral-hydrogen fraction of the IGM, $x_{\text{H I}}$, and a typical ionized bubble radius at $z = 6.6$ based on our estimates of $T_{\text{IGM},z=6.6}^{\text{Ly}\alpha} / T_{\text{IGM},z=5.7}^{\text{Ly}\alpha} \simeq 0.8$. The right panel of Figure 20 ticks $x_{\text{H I}}$ values at the corresponding $T_{\text{IGM},z=6.6}^{\text{Ly}\alpha} / T_{\text{IGM},z=5.7}^{\text{Ly}\alpha}$ obtained by analytic models of Santos et al. (2004) and radiative transfer models of McQuinn et al. (2007). In these comparisons, we assume that T_{IGM} is contributed by the scattering of the Ly α damping wing of hydrogen IGM alone. In the models of Santos et al. (2004), we have applied the realistic models with an Ly α line redshifted by 360 km s $^{-1}$

¹⁷ Because Kobayashi et al. (2010) define $T_{\text{IGM},z=5.7}^{\text{Ly}\alpha} = 1.0$, these three models correspond to their models of $T_{\text{Ly}\alpha} = 1.0, 0.8$, and 0.6.

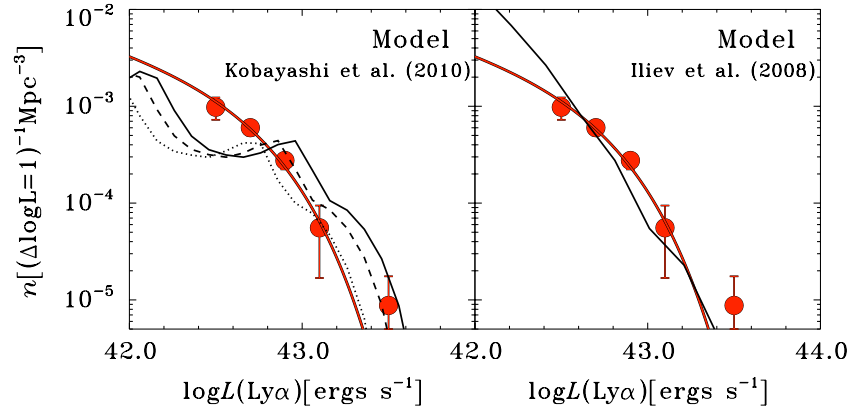


Figure 21. Comparisons of our Ly α LF at $z = 6.6$ with those given by theoretical models. Red circles and line are our best-estimate LF as shown in Figure 7. Left panel shows LFs predicted with semi-analytic models of Kobayashi et al. (2010). Solid, dashed, and dotted lines are predicted LFs with $T_{\text{IGM},z=6.6}^{\text{Ly}\alpha}/T_{\text{IGM},z=5.7}^{\text{Ly}\alpha} = 1.0, 0.8, \text{ and } 0.6$, respectively. Right panel plots an LF reproduced by the radiative transfer model of Iliev et al. (2008) with the applied shift of $\Delta \log L(\text{Ly}\alpha) = +31.6$.

from a systemic redshift, since redshifted Ly α lines by a few hundred km s $^{-1}$ are observationally found not only in LBGs (Pettini et al. 2001; Steidel et al. 2010) but also in LAEs (McLinden et al. 2010). In the McQuinn et al. (2007) models, we use ratios of intrinsic to observed Ly α luminosities at the cumulative number density of $\simeq 10^{-5}$ Mpc $^{-3}$, which corresponds to $\log L \simeq 43$ near to the luminosity range of our observations. Both of the models indicate that $T_{\text{IGM},z=6.6}^{\text{Ly}\alpha}/T_{\text{IGM},z=5.7}^{\text{Ly}\alpha} \simeq 0.8$ corresponds to $x_{\text{H I}} \simeq 0.2$. Even with the errors of $T_{\text{IGM},z=6.6}^{\text{Ly}\alpha}/T_{\text{IGM},z=5.7}^{\text{Ly}\alpha}$, we find that $x_{\text{H I}}$ is smaller than $\lesssim 0.4\text{--}0.5$.

The right panel of Figure 20 also presents the cosmic reionization models of Dijkstra et al. (2007b) and Furlanetto et al. (2006). The models of Dijkstra et al. (2007a) imply that our observational estimate of $T_{\text{IGM},z=6.6}^{\text{Ly}\alpha}/T_{\text{IGM},z=5.7}^{\text{Ly}\alpha} \simeq 0.8$ corresponds to a typical ionized bubble of size $\gtrsim 40$ comoving Mpc. Following the discussion of Dijkstra et al. (2007b), we apply the analytic model of Furlanetto et al. (2006) to this typical ionized bubble size. At the top of the right panel of Figure 20, we tick the volume-averaged neutral fraction predicated by Furlanetto et al. (2006). We find that the model of Furlanetto et al. (2006) infers that our lower limit of $\gtrsim 40$ comoving Mpc corresponds to the neutral fraction of $x_{\text{H I}} \lesssim 0.1$.

In summary, all of these various theoretical models, i.e., analytic, semi-analytic, and numerical models, indicate that our observational estimate of $T_{\text{IGM},z=6.6}^{\text{Ly}\alpha}/T_{\text{IGM},z=5.7}^{\text{Ly}\alpha} = 0.80 \pm 0.18$ corresponds to $x_{\text{H I}} \lesssim 0.2 \pm 0.2$. In the previous studies of Ly α LFs, Malhotra & Rhoads (2004) and Kashikawa et al. (2006) place upper limits of neutral fraction for $x_{\text{H I}} \lesssim 0.3$ and $\lesssim 0.45$, respectively, with the combination of their measurements and one analytic model of Santos et al. (2004). Our result is consistent with these previous studies, but our constraint is stronger and more robust than these previous results because of our better LF evolution determination with cosmic variance errors and the inclusion of model-dependent errors based on various independent reionization models. If all of our deep fields are not strongly biased by patchy IGM distribution by chance, our conclusion of IGM neutral fraction, $x_{\text{H I}} \lesssim 0.2 \pm 0.2$, is not significantly changed.

6.1.2. Evolution of Clustering

Theoretical models predict that a clustering amplitude of observed LAEs is boosted, due to the additional clustering of

LAEs whose Ly α photons can escape in the case where these LAEs reside in an ionized bubble at the reionization epoch (Furlanetto et al. 2006; McQuinn et al. 2007; Lidz et al. 2009; cf. Iliev et al. 2008). In Figure 13, we find no sudden rise of bias from $z = 5.7$ to 6.6 beyond the error bars. This indicates that clustering of $z = 6.6$ LAEs is weakly affected by cosmic reionization. With this result on bias evolution, we constrain cosmic reionization models of LAE clustering predictions.

Figure 22 compares the ACFs and bias of our LAEs at $z = 6.6$ with theoretical predictions of McQuinn et al. (2007) and Furlanetto et al. (2006). McQuinn et al. (2007) models are based on radiative transfer simulations. In their models, Ly α emission fluxes are assigned to dark halos with a mass above a minimum halo mass. We find that the average hosting dark halo masses of LAEs are about $10^{11 \pm 1} M_{\odot}$ over $z = 2\text{--}7$ in Section 4.3. This result is also correct at only $z = 2\text{--}6$, even if we omit the results of $z = 6.6$ LAEs whose clustering might be contaminated by the cosmic reionization effect. If we assume that hosting halo masses of LAEs do not change significantly from $z \sim 6$ to 6.6 as is true for $z = 3\text{--}6$ LAEs, the possible minimum halo mass of $z = 6.6$ LAEs is about $10^{10} M_{\odot}$. The top panel of Figure 22 plots the models of McQuinn et al. (2007) with the minimum halo mass of $3 \times 10^{10} M_{\odot}$ which is the closest to $10^{10} M_{\odot}$ and the smallest halo mass in their models. The comparison of our $z = 6.6$ LAEs and these models indicates that the neutral-hydrogen fraction of IGM is less than $x_{\text{H I}} \lesssim 0.5$ at $z = 6.6$. We also plot the rest of models with masses of $7 \times 10^{10} M_{\odot}$ and $1 \times 10^{11} M_{\odot}$ provided by McQuinn et al. (2007), and confirm that these massive halo models generally give a strong clustering, and that their constraints on $x_{\text{H I}}$ are all consistent with this relatively weak upper limit of $x_{\text{H I}} \lesssim 0.5$. Thus, the comparison with the McQuinn et al. (2007) models places an upper limit of $x_{\text{H I}} \lesssim 0.5$. The comparison with the Furlanetto et al. (2006) models is shown in the bottom panel of Figure 22. We use ratios of small-scale bias to hosting halo bias for LAEs in Furlanetto et al. (2006). Furlanetto et al. (2006) define the small-scale bias as a bias at a scale smaller than a typical ionized bubble size at the redshift. At $z = 6.6$, near the end of reionization, a typical size of ionized bubbles is $\gtrsim 10\text{--}100$ Mpc. Because our bias estimates of $z = 6.6$ LAEs are mostly made at the scale of $\simeq 1\text{--}10$ Mpc (see Figure 12), we thus regard our bias values as a small-scale bias that is defined in the study of Furlanetto et al. (2006). For a hosting halo bias, we assume again no evolution of halo mass, and use $b = 3.7$, which is a

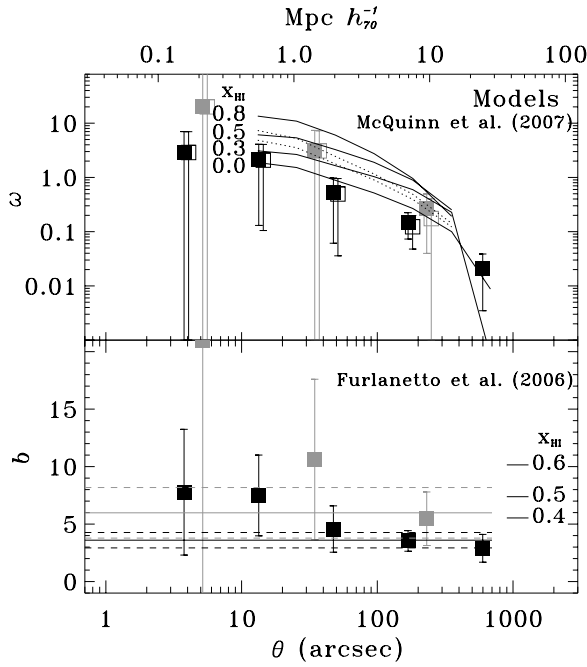


Figure 22. Comparison with our clustering measurements and reionization models. This plot is the same as Figure 12, but with the model predictions of ACF in the top panel (McQuinn et al. 2007) and bias in the bottom panel (Furlanetto et al. 2006). Top: solid lines are the model predictions of McQuinn et al. (2007) for $z = 6.6$ LAEs whose hosting dark halo mass is $3 \times 10^{10} M_{\odot}$. Neutral fractions of the universe are $x_{\text{HI}} = 0.0, 0.3, 0.5$, and 0.8 from bottom to top lines. Dotted lines indicate $z = 6.6$ LAEs with a dark halo mass of $7 \times 10^{10} M_{\odot}$ (bottom) and $1 \times 10^{11} M_{\odot}$ (top) in the case of $x_{\text{HI}} = 0.0$. Bottom: at the right side of this plot, we present Furlanetto et al.'s (2006) predicted bias values under the assumptions described in the text. For clarity, we also plot the best-bias estimate and 1σ ranges for our bright ($N_{\text{B}921} < 25.5$) LAE subsample with gray solid and dashed lines, respectively.

bias of $10^{10} M_{\odot}$ at $z = 6.6$ given by Equation (19). Comparing the 1σ limits of average bias for all sample (black dashed line) and the bright subsample (dark dashed line) in the bottom panel of Figure 22, we find that the neutral-hydrogen fraction of IGM should be smaller than $x_{\text{HI}} \lesssim 0.5$ at $z = 6.6$. Either McQuinn et al. (2007) or Furlanetto et al. (2006) models would imply that a neutral-hydrogen fraction is $x_{\text{HI}} \lesssim 0.5$ at $z = 6.6$ based on our clustering estimates.

6.1.3. Evolution of Ly α Line Profile

The Ly α damping wing of neutral-hydrogen IGM absorbs an Ly α emission line at $>1216 \text{ \AA}$ in the partially and fully neutral universe. Because Ly α damping wing absorption at $>1216 \text{ \AA}$ monotonically weakens toward red wavelengths, the damping wing absorption changes the shape of Ly α line profile. Since an Ly α flux absorbed by Ly α forest has an asymmetric profile with its flux peak near 1216 \AA , i.e., in the bluest wavelength of high- z Ly α line, the absorption component of Ly α damping wing (having a stronger attenuation in bluer wavelengths) should broaden the Ly α line. We use models of Ly α lines made by Dijkstra et al. (2007a), and evaluate the Ly α line broadening. We find that an FWHM of Ly α line broadens by 7%–10% in a very neutral universe where an LAE resides in an ionized bubble with a radius of 0.7 physical Mpc (5 comoving Mpc at $z = 6.6$), compared with an LAE in a more ionized universe with an ionized bubble radius of 2–10 physical Mpc (15–80 comoving Mpc at $z = 6.6$). Because the curvature of the Ly α damping

wing absorption is not steep, the Ly α line broadening is not large, only by a few 10% level. Thus, high-quality spectra are needed to identify the Ly α line broadening, if any, at an observed redshift. In Section 5.1, we obtain the direct (Gaussian) FWHM velocity widths of $251 (270) \pm 16 \text{ km s}^{-1}$ at $z = 6.6$ and $260 (265) \pm 37 \text{ km s}^{-1}$ at $z = 5.7$. These measurements include errors of 6% and 14%, which allow us to marginally identify a few 10% level broadening of Ly α . Our data show that there is no large evolution of Ly α FWHM beyond $\simeq 14\%$, but it is not clear whether a few percent level FWHM broadening exists. In fact, there is a possible hint of flattening of Ly α profile from $z = 5.7$ to 6.6 (Section 5.1), although its significance level is below the 1σ level. One of the goals of future LAE studies will be testing the broadening of Ly α FWHM down to a few percent level.

Haiman & Cen (2005) suggest a test of reionization with a relation between Ly α luminosity and line width. They claim that LAEs in a neutral universe have an anti-correlation between Ly α luminosity and line width, because fainter LAEs preferably residing in smaller H II regions are affected by a stronger damping wing attenuation than brighter LAEs. We compare our observational results with the model of Haiman & Cen (2005) in the luminosity range and velocity width similar to our observations. The model of Haiman & Cen (2005) indicates that, if the universe is fully neutral ($x_{\text{HI}} = 1$), an FWHM velocity width (line width) decreases only by 30 km s^{-1} (1 \AA) from $\log L(\text{Ly}\alpha) = 42.5$ to $\log L(\text{Ly}\alpha) = 43.5$ for LAEs with a velocity width of 300 km s^{-1} . In their model, no anti-correlation, but rather positive correlation, is found for a more ionized universe with a neutral fraction of $x_{\text{HI}} = 0.5$ and 0.25 in this relatively bright luminosity range. Thus, in this luminosity range, they predict that a weak anti-correlation appears only when the universe is nearly neutral. Our observational results indicate that there is no anti-correlation between Ly α luminosity and FWHM velocity width (Section 5.2). Our best-fit function presented in Figure 16 shows a rather positive correlation and an increase of FWHM velocity width by $111 \pm 45 \text{ km s}^{-1}$ from $\log L(\text{Ly}\alpha) = 42.5$ to $\log L(\text{Ly}\alpha) = 43.5$. If the model prediction of Haiman & Cen (2005) is correct, our observations rule out the fully neutral universe at $z = 6.6$ at the $\simeq 3\sigma$ level.

In Section 5.1, we find an interesting knee feature in Ly α line profiles of LAEs at $z = 6.6$ as well as $z = 5.7$. It would be suggestive of galaxy outflow or a proximity effect, but it is not clear whether it can be interpreted with a reasonable physical picture. Because we find these knee features not only at $z = 6.6$, but also $z = 5.7$ when the universe is highly ionized ($x_{\text{HI}} \sim 10^{-4}$), the knee features would not be related to cosmic reionization but galaxy formation. The knee features may be important for understanding dynamics, UV radiation field, and structure of LAEs at high redshifts.

6.1.4. Cosmic Reionization

In Sections 6.1.1–6.1.3, we have obtained the constraints of the neutral-hydrogen fraction of $x_{\text{HI}} \lesssim 0.2 \pm 0.2$ and $x_{\text{HI}} \lesssim 0.5$ at $z = 6.6$ from the evolution of Ly α LF and clustering, respectively, and ruled out the fully neutral universe at $z = 6.6$ at the $\simeq 3\sigma$ level by Ly α line profiles. It should be noted that these three constraints agree, even though these results are given by three independent observational quantities, i.e., Ly α LF, clustering, and Ly α line properties. In Figure 23, we plot our two relatively strong constraints of x_{HI} from Ly α LF and clustering, and compare with the previous estimates and theoretical models. Our results are consistent with the previous ones based on LAEs as well as gamma-ray bursts

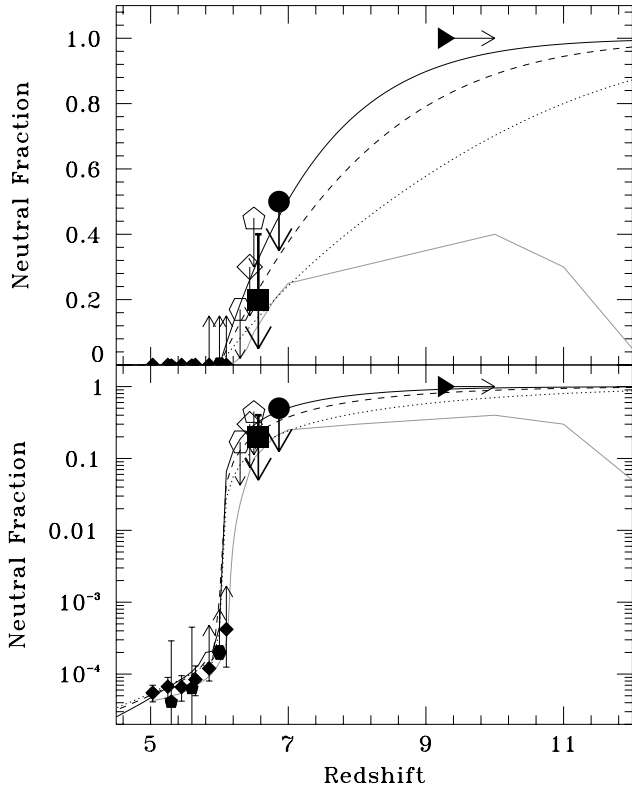


Figure 23. Neutral-hydrogen fraction, x_{HI} , of IGM as a function of redshift. Top and bottom panels are the same, but with a vertical axis of linear and log scales, respectively. The filled square and circle are the upper limits of x_{HI} that we obtain from the evolution of $\text{Ly}\alpha$ LF and clustering, respectively. The open diamond and pentagon denote the upper limits from $\text{Ly}\alpha$ LF at $z = 6.5$ given by Malhotra & Rhoads (2004) and Kashikawa et al. (2006). The open hexagon is the upper limit estimated from the constraints of $\text{Ly}\alpha$ damping wing of GRB at $z = 6.3$ (Totani et al. 2006), respectively. The filled hexagon and pentagons indicate constraints given by GRB spectra (Gallerani et al. 2008b) and QSO dark gap statistics (Gallerani et al. 2008a), respectively. The filled diamonds represent the measurements from GP optical depth of SDSS QSOs (Fan et al. 2006). The triangle plots the 1σ lower limit of redshift of a neutral universe given by WMAP7 (Larson et al. 2010) in the case of instantaneous reionization. Avoiding overlapping symbols, we give a small offset along redshift to the positions of the filled circle and the open diamond. Dotted, dashed, and solid lines show the evolution of x_{HI} for minihalo, small, and large halo cases, respectively, predicted by Choudhury et al. (2008). Gray solid line presents the prediction in the double reionization scenario suggested by Cen (2003).

(GRBs)¹⁸ and QSOs, and our constraint from $\text{Ly}\alpha$ LF, $x_{\text{HI}} \lesssim 0.2 \pm 0.2$, is generally stronger than the previous ones at $z \simeq 6.5$ – 6.6 . This upper limit at $z = 6.6$ prefers an early ($z \gtrsim 7$) reionization on average, which requires more ionizing photons at $z \gtrsim 7$.

The triangle in Figure 23 is the 1σ lower limit of redshift given by the WMAP7 result in the instantaneous reionization case ($z = 10.5 \pm 1.2$; Larson et al. 2010). This rules out the instantaneous reionization at $z < 9.3$, i.e., 100% neutral fraction at $z < 9.3$, at the 1σ level. Figure 23 shows predictions of semi-analytic reionization models of Choudhury et al. (2008). For sources of reionization, they assume three minimum halo masses for star-forming galaxies, $\sim 5 \times 10^5 M_\odot$, $\sim 10^8 M_\odot$, and $\sim 10^9 M_\odot$ at $z = 6$ for mini, small, and large halo cases, respectively. Choudhury et al. (2008) have concluded that reionization only

by large halos is ruled out by the constraints of the electron scattering optical depth (WMAP3; Spergel et al. 2007) and various neutral-hydrogen fraction upper limits available at the time of their study. Our results support their claim, and our relatively strong upper limit of $x_{\text{HI}} \lesssim 0.2 \pm 0.2$ favor their model including minihalos. Minihalos can accomplish the relatively early reionization, as suggested by various theoretical studies. On the other hand, a change of star-forming galaxy properties is also possible. These could be an increase of escape fraction of ionizing photons such suggested by high- z dropout observations (Ouchi et al. 2009b; Bunker et al. 2009; Finkelstein et al. 2010; Bouwens et al. 2010b). It is also possible that the changes of IMF and metallicity are important (e.g., Stiavelli et al. 2004). In fact, the model of Cen (2003) shown in Figure 23 includes the effects of IMF and metallicity changes. Cen (2003) argues that reionization took place twice; the first at $z \sim 15$ – 16 by metal-free Population III stars with a top-heavy IMF and the second at $z \sim 6$ by Population II stars, which give a medium large Thomson scattering optical depth of 0.10 ± 0.03 similar to WMAP7 results (Larson et al. 2010). This scenario gives a fairly low neutral fraction at $z = 6.6$ that is consistent with our LAE constraints. Although it is not clear whether reionization took place twice, metal-free star formation would characterize the history of cosmic reionization.

6.2. Role of LAEs in Galaxy Formation History

The evolution of LAE LF, clustering, and $\text{Ly}\alpha$ line profiles includes various hints for understanding LAEs in galaxy formation history. As shown in Figure 14, a typical bias of LAEs is smaller than that of LBGs over $z = 2$ – 7 . Thus, a typical halo mass of LBG is estimated to be $\sim 10^{12 \pm 1} M_\odot$, about one order of magnitude larger than that of LAEs (Hamana et al. 2004; Ouchi et al. 2004b, 2005b; Lee et al. 2006, 2009; McLure et al. 2009; Hildebrandt et al. 2009).¹⁹ It is possible that some galaxies become LAEs with a halo mass of $\sim 10^{11} M_\odot$, then evolve into LBGs with a halo mass of $\sim 10^{12} M_\odot$ via mass assembly such as mergers and accretion. If this scenario is true, a typical LAE could be a progenitor of typical LBG. In this scenario, two observational questions are consistently answered. The first question is the different trend of LBG and LAE evolution. The LF of LBGs decreases from $z = 3$ to 6 (e.g., Bouwens et al. 2007), while the LF of LAEs does not change much in $z = 3$ – 6 (e.g., Ouchi et al. 2008). In this scenario, LAEs would form earlier than LBGs, and the significant drop of LF may be found only for LBGs in this intermediate redshift of $z = 3$ – 6 . This is because the number density of LBG’s massive ($\sim 10^{12} M_\odot$) hosting halos sharply drops from $z = 3$ to 6 , while that of LAEs’ less massive ($\sim 10^{11} M_\odot$) hosting halos does not decrease much based on the halo model (Sheth & Tormen 1999). The redshift of $z = 3$ – 6 might be still the major formation epoch of LBGs, while the major formation epoch of LAEs would be earlier than LBGs, i.e., at $z > 6$, near the epoch when we find a decrease of LAE LF (from $z = 5.7$ to 6.6) in this study. The second question is the deficit of strong $\text{Ly}\alpha$ emitting galaxies among a UV bright population. It is found that UV-bright galaxies do not have a strong $\text{Ly}\alpha$ emission line (Ouchi et al. 2003, 2008; Ando et al. 2006; Shimasaku et al. 2006; Vanzella et al. 2007,

¹⁸ The estimates of a single GRB would include an additional systematic error of $\delta x_{\text{HI}} \sim 0.3$ owing to the patchiness of reionization (McQuinn et al. 2008). Since the $z \simeq 6.7$ GRB estimate of Greiner et al. (2009) allows $x_{\text{HI}} = 0.001$ – 1 within the 1.2σ level due to the strong degeneracy between absorptions of a damped $\text{Ly}\alpha$ absorber and IGM, the result of Greiner et al. (2009) is not included in Figure 23.

¹⁹ Note that LBGs referred to here are typical dropout galaxies with a UV luminosity near L^* , and that, in our discussion, we do not include the population of the LAE analog of dropout galaxies with a very faint UV magnitude such those studied by Stark et al. (2010). Similarly, LAEs are typical LAEs so far observed in $\log L(\text{Ly}\alpha) \simeq 42$ – 44 , and not those fainter than this luminosity range.

2009). This trend is usually discussed on a plane of UV luminosity and Ly α EW, and no objects are found in the UV-luminous and EW-large regime (e.g., Ando et al. 2006). In the case of our scenario, a typical LAE evolves into a typical LBG, i.e., less massive galaxies with a strong Ly α emission line become massive galaxies with a weak or no Ly α emission line. When this evolution is investigated on this plane, objects move from UV-faint to UV-luminous regimes, because UV luminosity positively correlates with stellar mass at high redshifts (Papovich et al. 2001; Sawicki et al. 2007; Yabe et al. 2009). The UV-faint (less massive) objects are, first, distributed widely in EW values on this plane before the evolution. Then, these objects end up in the UV-bright and small-EW regime on this plane after the evolution. The tendency of Ly α deficit among UV-bright galaxies would be consistent with the scenario of this LAE–LBG evolution sequence. In this way, this evolutionary scenario would provide the answers to these two observational questions. The recent study of Vanzella et al. (2009) has found that LAEs have a more compact UV-continuum morphology than LBGs with no Ly α emission at $z \sim 4$. If our scenario of LAE–LBG evolution is correct, star formation activities start at the center then extend to the outskirts of galaxies, which is suggestive of the inside-out picture of galaxy formation.

The dotted lines in Figure 13 show evolutionary tracks of dark halos for galaxy-conserving models. The galaxy-conserving model assumes that the motion of galaxies is purely driven by gravity, and that merging does not take place. In this case, the bias value of galaxies decreases as the universe evolves with time,

$$b_g = 1 + (b_g^0 - 1)/D(z), \quad (24)$$

where b_g^0 is a bias at $z = 0$ (Fry 1996). Under the assumption of the galaxy-conserving evolution, dark halos of $z = 3$ LAEs evolve into dark halos with $b_g \simeq 1.1$ – 1.3 at $z = 0$. Because, in more realistic extended Press–Shechter formalism (e.g., Lacey & Cole 1993), average evolutionary tracks come slightly below those of the galaxy-conserving models (see, e.g., Figure 13 of Ichikawa et al. 2007), dark halos of $z = 3$ LAEs probably evolve into dark halos with $b_g \simeq 1$ which host present-day $\simeq L^*$ galaxies including the Milky Way, as suggested by Gawiser et al. (2007). On the other hand, in Figure 13, LAEs at $z \simeq 4$ – 7 have a significantly larger bias than $z = 3$ LAEs, and the increase of the LAE bias measurements toward high- z (nearly along solid lines) is steeper than those of galaxy-conserving evolution (dotted lines). The galaxy-conserving model indicates that dark halos of $z \simeq 4$ – 7 LAEs evolve into those with $b_g \simeq 1.5$ – 2 at $z = 0$ whose value is higher than those of $z = 3.1$ LAEs ($b_g \simeq 1.1$ – 1.3), which implies that descendants of $z \simeq 4$ – 7 LAEs are different from those of $z = 3$ LAEs. On average, the descendants of $z \simeq 4$ – 7 LAEs would be more massive than those of $z = 3$ LAEs. The majority of LAEs at $z \simeq 4$ – 7 are probably not ancestors of the Milky Way, but today’s large galaxies more massive than the Milky Way, although there should exist some LAEs that become today’s L^* galaxies by a probability process of halo mass build up. These implications from our clustering results are similar to those from theoretical predictions by Salvadori et al. (2010) who claim that only $\simeq 2\%$ of Milky Way progenitors can be LAEs.

7. CONCLUSIONS

We have identified 207 LAEs at $z = 6.6$ in the 1 deg^2 area of SXDS field down to $L \gtrsim 2.5 \times 10^{42} \text{ erg s}^{-1}$ and $\text{EW} \gtrsim 14 \text{ \AA}$ by deep and wide-field narrowband and broadband imaging of

Subaru/Suprime-Cam. Nineteen Ly α lines are confirmed by the high-quality Keck/DEIMOS spectra, and none of interlopers have been found in our sample through our extensive deep spectroscopy campaign as well as the SXDS project spectroscopy consisting of 3233 objects at $z = 0$ – 6 . We have obtained the Ly α LF, ACF, and Ly α line profiles to constrain cosmic reionization and early galaxy formation with the aid of recent theoretical model predictions. We have also derived ACFs of LAEs at $z = 3.1$ – 5.7 in the SXDS field to find the evolutionary trend of LAE clustering from $z \sim 3$ – 7 in the framework of the Λ CDM model. The major results of our study are summarized below.

1. Our Ly α LF of $z = 6.6$ LAEs shows the best-fit Schechter parameters of $\phi^* = 8.5^{+3.0}_{-2.2} \times 10^{-4} \text{ Mpc}^{-3}$ and $L_{\text{Ly}\alpha}^* = 4.4^{+0.6}_{-0.6} \times 10^{42} \text{ erg s}^{-1}$ with a fixed $\alpha = -1.5$, where the errors include uncertainties of statistics and cosmic variance. The combination of statistics and cosmic variance errors presents scatters of number density measurements up to a factor of $\simeq 10$ among five subfields of $\sim 0.2 \text{ deg}^2$ areas, although the typical scatters of the subfield number densities are not far beyond the errors of Poisson statistics. Comparing this LAE LF at $z = 6.6$ with the one at $z = 5.7$, we find that the Ly α LF decreases from $z = 5.7$ to 6.6 at the $\gtrsim 90\%$ confidence level. A more dominant decrease of L^* (luminosity evolution) than ϕ^* (number evolution) is preferable. The decrease of Ly α LF from $z = 5.7$ to 6.6 is $\simeq 30\%$ in the case of pure luminosity evolution. Note that this 30% luminosity decrease is too small to be identified by the previous studies, due to their large uncertainties from small statistics and cosmic variance.
2. We have identified a significant angular-correlation signal for our $z = 6.6$ LAE sample. This is the detection of clustering signal for the most distant galaxies, to date. The correlation length and bias are $r_0 = 2$ – $5 h_{100}^{-1} \text{ Mpc}$ and $b = 3$ – 6 , respectively. There is no sudden boost of clustering amplitude given by cosmic reionization at $z = 6.6$. In the framework of Λ CDM models, the average hosting dark halo mass inferred from clustering is 10^{10} – $10^{11} M_\odot$. The duty cycle of LAE population, a product of star formation and Ly α emitting duty cycles, is a few 0.1 to a few percent, roughly $\sim 1\%$, although the constraint on the duty cycle involves large uncertainties because of the bias estimate errors and the fairly flat relation between number density and bias of halos from the Λ CDM model.
3. Based on our high-quality DEIMOS spectra, we have found that most of the Ly α emission lines present a clear asymmetric profile with the average FWHM velocity width of $251 \pm 16 \text{ km s}^{-1}$ (direct measurement) at $\log L(\text{Ly}\alpha) \simeq 42.6$ – 43.6 , and that the average FWHM velocity width does not largely evolve from $z = 5.7$ to 6.6 beyond errors of our $\simeq 40 \text{ km s}^{-1}$, which is dominated by the error of our reference $z = 5.7$ LAE. There is no anti-correlation between Ly α luminosity and velocity width. If our spectroscopic sample is not biased, Ly α velocity width positively correlates with Ly α luminosity at $z = 6.6$ in the luminosity range of $\log L(\text{Ly}\alpha) \simeq 42.6$ – 43.6 . We identify a knee feature in a blue tail of Ly α line in our composite spectra of LAEs at $z = 6.6$ as well as 5.7 , which cannot be explained by statistical and systematic instrumental errors. These knee features, if true, would be important for understanding the dynamics, UV radiation field, and structure of LAEs.

4. We compare the evolution of Ly α LF, clustering, and Ly α line profiles from our observations with various reionization models including analytic, semi-analytic, and radiative transfer models. Although there would exist a small $\sim 20\%$ decrease of IGM transmission from $z = 5.7$ to 6.6 due to cosmic reionization, the comparisons of all models and observational quantities reach the same conclusion that hydrogen IGM is not highly neutral at $z = 6.6$. The upper limit of neutral fraction is $x_{\text{H I}} \lesssim 0.2 \pm 0.2$ from our Ly α LF evolution and $x_{\text{H I}} \lesssim 0.5$ from our clustering evolution between $z = 5.7$ and 6.6 . A fully neutral universe, $x_{\text{H I}} = 1$, at $z = 6.6$ is ruled out by no large evolution of Ly α velocity width from $z = 5.7$ to 6.6 and by no anti-correlation between Ly α luminosity and velocity width at $z = 6.6$. All of these reionization tests with Ly α LFs, clustering, and line profiles, agree that the neutral-hydrogen fraction of the IGM is not high at $z = 6.6$. Our strongest constraint from Ly α LF, $x_{\text{H I}} \lesssim 0.2 \pm 0.2$, implies that the major reionization process took place early, at $z \gtrsim 7$.
5. Calculating ACFs, bias, and hosting dark halos of low- z LAEs of SXDS at $z = 3.1\text{--}5.7$ in the same manner as those of our $z = 6.6$ LAEs, we find that hosting dark halo masses stay at the similar value of $10^{11\pm1} M_{\odot}$ over $z = 3\text{--}7$. It implies that LAEs are galaxies at the evolutionary stage for all or some type of galaxies whose dark halos have reached a mass of $\sim 10^{11\pm1} M_{\odot}$. Because a halo mass of typical ($\sim L^*$) LBGs is $\sim 10^{12\pm1} M_{\odot}$, about one order of magnitude larger than that of LAEs, there is a possibility that some galaxies become LAEs with a halo mass of $\sim 10^{11} M_{\odot}$ in the $\sim 1\%$ duty cycle, then evolve into typical LBGs with a halo mass of $\sim 10^{12} M_{\odot}$ via mass assembly such as mergers and accretion. This scenario consistently explains two observational results of LBGs and LAEs: the different LF evolutionary trend between LBGs and LAEs (e.g., Ouchi et al. 2008), and the deficit of strong LAEs among UV bright population (e.g., Ando et al. 2006).

We thank Renyue Cen, Tirthankar Roy Choudhury, Mark Dijkstra, Andrea Ferrara, Ilian Iliev, Masakazu Kobayashi, Matt McQuinn, Takashi Murayama, and Xiaohui Fan for providing their data. Especially, we appreciate the efforts of Mark Dijkstra and Matt McQuinn who responded to a number of our requests. M.O. and K.S. acknowledge Cedric Lacey and Orsi Alvaro for their helpful comments on clustering analysis. M.O. thanks Richard Ellis for his encouragement to publish these results as early as possible. M.O. is grateful to comments from Kentaro Aoki, Richard Ellis, David Sobral, and Eros Vanzella, and useful discussions with Renyue Cen, Mark Dijkstra, Eric Gawiser, Esther Hu, Matt McQuinn, James Rhoads, Alice Shapley, Haojing Yan, and Zheng Zheng at the Ly α Emitter Workshop, Ohio State University, held on 2010 April 26–27. M.O. has been supported via Carnegie Fellowship.

Facilities: Subaru (Suprime-Cam), Keck:II (DEIMOS)

REFERENCES

- Ajiki, M., et al. 2003, *AJ*, **126**, 2091
- Ando, M., Ohta, K., Iwata, I., Akiyama, M., Aoki, K., & Tamura, N. 2006, *ApJ*, **645**, L9
- Bardeen, J. M., Bond, J. R., Kaiser, N., & Szalay, A. S. 1986, *ApJ*, **304**, 15
- Becker, G. D., Rauch, M., & Sargent, W. L. W. 2007, *ApJ*, **662**, 72
- Bertin, E., & Arnouts, S. 1996, *A&AS*, **117**, 393
- Bohlin, R. C., Colina, L., & Finley, D. S. 1995, *AJ*, **110**, 1316
- Bouwens, R. J., Illingworth, G. D., Franx, M., & Ford, H. 2007, *ApJ*, **670**, 928
- Bouwens, R. J., et al. 2010a, *ApJ*, **709**, L133
- Bouwens, R. J., et al. 2010b, *ApJ*, **708**, L69
- Bunker, A., et al. 2009, arXiv:0909.2255
- Carroll, S. M., Press, W. H., & Turner, E. L. 1992, *ARA&A*, **30**, 499
- Cassata, P., et al. 2010, arXiv:1003.3480
- Castellano, M., et al. 2010, *A&A*, **511**, A20
- Cen, R. 2003, *ApJ*, **591**, 12
- Choudhury, T. R., Ferrara, A., & Gallerani, S. 2008, *MNRAS*, **385**, L58
- Coleman, G. D., Wu, C.-C., & Weedman, D. W. 1980, *ApJS*, **43**, 393
- Cuby, J.-G., Hibon, P., Lidman, C., Le Fèvre, O., Gilmozzi, R., Moorwood, A., & van der Werf, P. 2007, *A&A*, **461**, 911
- Daddi, E., Cimatti, A., Pozzetti, L., Hoekstra, H., Röttgering, H. J. A., Renzini, A., Zamorani, G., & Mannucci, F. 2000, *A&A*, **361**, 535
- Dayal, P., Maselli, A., & Ferrara, A. 2010, arXiv:1002.0839
- Dijkstra, M., Lidz, A., & Wyithe, J. S. B. 2007a, *MNRAS*, **377**, 1175
- Dijkstra, M., & Wyithe, J. S. B. 2010, arXiv:1004.2490
- Dijkstra, M., Wyithe, J. S. B., & Haiman, Z. 2007b, *MNRAS*, **379**, 253
- Dunkley, J., et al. 2009, *ApJS*, **180**, 306
- Efstathiou, G., Bernstein, G., Tyson, J. A., Katz, N., & Guhathakurta, P. 1991, *ApJ*, **380**, L47
- Faber, S. M., et al. 2003, *Proc. SPIE*, **4841**, 1657
- Fan, X., et al. 2006, *AJ*, **132**, 117
- Finkelstein, S. L., Papovich, C., Giavalisco, M., Reddy, N. A., Ferguson, H. C., Koekemoer, A. M., & Dickinson, M. 2010, *ApJ*, **719**, 1250
- Finlator, K., Oppenheimer, B. D., & Davé, R. 2010, *ApJS*, in press (arXiv:1005.4066)
- Fry, J. N. 1996, *ApJ*, **461**, L65
- Fukugita, M., & Kawasaki, M. 1994, *MNRAS*, **269**, 563
- Furlanetto, S. R., Zaldarriaga, M., & Hernquist, L. 2006, *MNRAS*, **365**, 1012
- Furusawa, H., et al. 2008, *ApJS*, **176**, 1
- Gallerani, S., Ferrara, A., Fan, X., & Choudhury, T. R. 2008a, *MNRAS*, **386**, 359
- Gallerani, S., Salvaterra, R., Ferrara, A., & Choudhury, T. R. 2008b, *MNRAS*, **388**, L84
- Gawiser, E., et al. 2007, *ApJ*, **671**, 278
- Greiner, J., et al. 2009, *ApJ*, **693**, 1610
- Groth, E. J., & Peebles, P. J. E. 1977, *ApJ*, **217**, 385
- Guaita, L., et al. 2010, *ApJ*, **714**, 255
- Gunn, J. E., & Stryker, L. L. 1983, *ApJS*, **52**, 121
- Haiman, Z. 2002, *ApJ*, **576**, L1
- Haiman, Z., & Cen, R. 2005, *ApJ*, **623**, 627
- Hamana, T., Ouchi, M., Shimasaku, K., Kayo, I., & Suto, Y. 2004, *MNRAS*, **347**, 813
- Hayes, M., et al. 2010, *Nature*, **464**, 562
- Hibon, P., et al. 2010, *A&A*, **515**, A97
- Hickey, S., Bunker, A., Jarvis, M. J., Chiu, K., & Bonfield, D. 2010, *MNRAS*, **404**, 212
- Hildebrandt, H., Pielorz, J., Erben, T., Schneider, P., Eifler, T., Simon, P., & Dietrich, J. P. 2007, *A&A*, **462**, 865
- Hildebrandt, H., Pielorz, J., Erben, T., van Waerbeke, L., Simon, P., & Capak, P. 2009, *A&A*, **498**, 725
- Hu, E. M., & Cowie, L. L. 2006, *Nature*, **440**, 1145
- Hu, E. M., Cowie, L. L., Capak, P., & Kakazu, Y. 2005, in *IAU Colloq. 199, Probing Galaxies through Quasar Absorption Lines*, ed. P. R. Williams, C.-G. Shu, & B. Menard (Cambridge: Cambridge Univ. Press), **363**
- Hu, E. M., Cowie, L. L., Capak, P., McMahon, R. G., Hayashino, T., & Komiyama, Y. 2004, *AJ*, **127**, 563
- Ichikawa, T., et al. 2007, *PASJ*, **59**, 1081
- Iliev, I. T., Shapiro, P. R., McDonald, P., Mellema, G., & Pen, U.-L. 2008, *MNRAS*, **391**, 63
- Iye, M., et al. 2006, *Nature*, **443**, 186
- Kashikawa, N., et al. 2006, *ApJ*, **648**, 7
- Kinney, A. L., Calzetti, D., Bohlin, R. C., McQuade, K., Storchi-Bergmann, T., & Schmitt, H. R. 1996, *ApJ*, **467**, 38
- Kobayashi, M. A. R., Totani, T., & Nagashima, M. 2010, *ApJ*, **708**, 1119
- Komatsu, E., et al. 2009, *ApJS*, **180**, 330
- Kovač, K., Somerville, R. S., Rhoads, J. E., Malhotra, S., & Wang, J. 2007, *ApJ*, **668**, 15
- Lacey, C., & Cole, S. 1993, *MNRAS*, **262**, 627
- Landy, S. D., & Szalay, A. S. 1993, *ApJ*, **412**, 64
- Larson, D., et al. 2010, arXiv:1001.4635
- Lee, K.-S., Giavalisco, M., Conroy, C., Wechsler, R. H., Ferguson, H. C., Somerville, R. S., Dickinson, M. E., & Urry, C. M. 2009, *ApJ*, **695**, 368
- Lee, K.-S., Giavalisco, M., Gnedin, O. Y., Somerville, R. S., Ferguson, H. C., Dickinson, M., & Ouchi, M. 2006, *ApJ*, **642**, 63

- Lidz, A., Zahn, O., Furlanetto, S. R., McQuinn, M., Hernquist, L., & Zaldarriaga, M. 2009, *ApJ*, **690**, 252
- Ling, E. N., Barrow, J. D., & Frenk, C. S. 1986, *MNRAS*, **223**, 21P
- Madau, P. 1995, *ApJ*, **441**, 18
- Madau, P., Pozzetti, L., & Dickinson, M. 1998, *ApJ*, **498**, 106
- Malhotra, S., & Rhoads, J. E. 2004, *ApJ*, **617**, L5
- McLinden, E. M., et al. 2010, arXiv:1006.1895
- McLure, R. J., Cirasuolo, M., Dunlop, J. S., Foucaud, S., & Almaini, O. 2009, *MNRAS*, **395**, 2196
- McLure, R. J., Dunlop, J. S., Cirasuolo, M., Koekemoer, A. M., Sabbi, E., Stark, D. P., Targett, T. A., & Ellis, R. S. 2010, *MNRAS*, **403**, 960
- McQuinn, M., Hernquist, L., Zaldarriaga, M., & Dutta, S. 2007, *MNRAS*, **381**, 75
- McQuinn, M., Lidz, A., Zaldarriaga, M., Hernquist, L., & Dutta, S. 2008, *MNRAS*, **388**, 1101
- Meiksin, A. 2006, *MNRAS*, **365**, 807
- Miyazaki, S., et al. 2002, *PASJ*, **54**, 833
- Mo, H. J., & White, S. D. M. 2002, *MNRAS*, **336**, 112
- Murayama, T., et al. 2007, *ApJS*, **172**, 523
- Nagamine, K., Ouchi, M., Springel, V., & Hernquist, L. 2008, arXiv:0802.0228
- Nagashima, M., & Yoshii, Y. 2004, *ApJ*, **610**, 23
- Nilsson, K. K., Orsi, A., Lacey, C. G., Baugh, C. M., & Thommes, E. 2007, *A&A*, **474**, 385
- Oesch, P. A., et al. 2010, *ApJ*, **709**, L16
- Ono, Y., Ouchi, M., Shimasaku, K., Dunlop, J., Farrah, D., McLure, R., & Okamura, S. 2010a, arXiv:1004.0963
- Ono, Y., et al. 2010b, *MNRAS*, **402**, 1580
- Ota, K., et al. 2008, *ApJ*, **677**, 12
- Ouchi, M., & SXDS Team. 2005, in Proc. 22nd Texas Symp. on Relativistic Astrophysics, ed. P. Chen, E. Bloom, G. Madejski, & V. Patrosian (Palo Alto, CA: Stanford Univ.), 29
- Ouchi, M., et al. 2003, *ApJ*, **582**, 60
- Ouchi, M., et al. 2004a, *ApJ*, **611**, 660
- Ouchi, M., et al. 2004b, *ApJ*, **611**, 685
- Ouchi, M., et al. 2005a, *ApJ*, **620**, L1
- Ouchi, M., et al. 2005b, *ApJ*, **635**, L117
- Ouchi, M., et al. 2008, *ApJS*, **176**, 301
- Ouchi, M., et al. 2009a, *ApJ*, **696**, 1164
- Ouchi, M., et al. 2009b, *ApJ*, **706**, 1136
- Overzier, R. A., Bouwens, R. J., Illingworth, G. D., & Franx, M. 2006, *ApJ*, **648**, L5
- Papovich, C., Dickinson, M., & Ferguson, H. C. 2001, *ApJ*, **559**, 620
- Peacock, J. A., & Dodds, S. J. 1996, *MNRAS*, **280**, L19
- Peebles, P. J. E. 1980, *The Large-Scale Structure of the Universe* (Princeton, NJ: Princeton Univ. Press)
- Pettini, M., Shapley, A. E., Steidel, C. C., Cuby, J.-G., Dickinson, M., Moorwood, A. F. M., Adelberger, K. L., & Giavalisco, M. 2001, *ApJ*, **554**, 981
- Rauch, M., et al. 2008, *ApJ*, **681**, 856
- Reddy, N. A., & Steidel, C. C. 2009, *ApJ*, **692**, 778
- Roche, N., & Eales, S. A. 1999, *MNRAS*, **307**, 703
- Salvadori, S., Dayal, P., & Ferrara, A. 2010, *MNRAS*, **407**, L1
- Santos, M. R., Ellis, R. S., Kneib, J.-P., Richard, J., & Kuijken, K. 2004, *ApJ*, **606**, 683
- Sawicki, M., et al. 2007, in ASP Conf. Ser. 380, At the Edge of the Universe: Latest Results from the Deepest Astronomical Surveys, ed. J. Afonso, H. C. Ferguson, B. Mobasher, & R. Norris (San Francisco, CA: ASP), 433
- Schaerer, D., & de Barros, S. 2010, *A&A*, **515**, A73
- Schechter, P. 1976, *ApJ*, **203**, 297
- Schlegel, D. J., Finkbeiner, D. P., & Davis, M. 1998, *ApJ*, **500**, 525
- Sheth, R. K., & Tormen, G. 1999, *MNRAS*, **308**, 119
- Shimasaku, K., et al. 2003, *ApJ*, **586**, L111
- Shimasaku, K., et al. 2006, *PASJ*, **58**, 313
- Simon, P. 2007, *A&A*, **473**, 711
- Sobral, D., Best, P. N., Geach, J. E., Smail, I., Cirasuolo, M., Garn, T., Dalton, G. B., & Kurk, J. 2010, *MNRAS*, **404**, 1551
- Sobral, D., et al. 2009, *MNRAS*, **398**, L68
- Spergel, D. N., et al. 2007, *ApJS*, **170**, 377
- Stark, D. P., Ellis, R. S., Chiu, K., Ouchi, M., & Bunker, A. 2010, arXiv:1003.5244
- Stark, D. P., Ellis, R. S., Richard, J., Kneib, J.-P., Smith, G. P., & Santos, M. R. 2007, *ApJ*, **663**, 10
- Steidel, C. C., Erb, D. K., Shapley, A. E., Pettini, M., Reddy, N., Bogosavljević, M., Rudie, G. C., & Rakic, O. 2010, *ApJ*, **717**, 289
- Stiavelli, M., Fall, S. M., & Panagia, N. 2004, *ApJ*, **610**, L1
- Taniguchi, Y., et al. 2005, *PASJ*, **57**, 165
- Tilvi, V., et al. 2010, *ApJ*, **721**, 1853
- Tokoku, C., et al. 2008, in ASP Conf. Ser. 399, Panoramic Views of Galaxy Formation and Evolution, ed. T. Kodama, T. Yamada, & K. Aoki (San Francisco, CA: ASP), 65
- Totani, T., Kawai, N., Kosugi, G., Aoki, K., Yamada, T., Iye, M., Ohta, K., & Hattori, T. 2006, *PASJ*, **58**, 485
- Vanzella, E., Cristiani, S., Dickinson, M., Giavalisco, M., Lee, K., Nonino, M., Rosati, P., & GOODS Team. 2007, in ASP Conf. Ser. 380, At the Edge of the Universe: Latest Results from the Deepest Astronomical Surveys, ed. J. Afonso, H. C. Ferguson, B. Mobasher, & R. Norris (San Francisco, CA: ASP), 45
- Vanzella, E., et al. 2009, *ApJ*, **695**, 1163
- Wilkins, S. M., Bunker, A. J., Ellis, R. S., Stark, D., Stanway, E. R., Chiu, K., Lorenzoni, S., & Jarvis, M. J. 2010a, *MNRAS*, **403**, 938
- Wilkins, S. M., Bunker, A. J., Lorenzoni, S., & Caruana, J. 2010b, arXiv:1002.4866
- Willis, J. P., & Courbin, F. 2005, *MNRAS*, **357**, 1348
- Willis, J. P., Courbin, F., Kneib, J.-P., & Minniti, D. 2008, *MNRAS*, **384**, 1039
- Yabe, K., Ohta, K., Iwata, I., Sawicki, M., Tamura, N., Akiyama, M., & Aoki, K. 2009, *ApJ*, **693**, 507
- Yagi, M., Kashikawa, N., Sekiguchi, M., Doi, M., Yasuda, N., Shimasaku, K., & Okamura, S. 2002, *AJ*, **123**, 66
- Yan, H.-J., Windhorst, R. A., Hathi, N. P., Cohen, S. H., Ryan, R. E., O'Connell, R. W., & McCarthy, P. J. 2010, *Res. Astron. Astrophys.*, **10**, 867
- Zehavi, I., et al. 2004, *ApJ*, **608**, 16
- Zheng, Z., Cen, R., Trac, H., & Miralda-Escude, J. 2010a, *ApJ*, **716**, 574
- Zheng, Z., Cen, R., Trac, H., & Miralda-Escude, J. 2010b, arXiv:1003.4990